Ab-initio modeling of photo-active materials beyond conventional lead halide perovskites

Bruno Cucco

COLLEGE SCIENCES DE LA MATIERE
DOCTORAL DES MOLECULES
BRETAGNE ET MATERIAUX

Université de Rennes

THÈSE DE DOCTORAT DE

L'UNIVERSITÉ DE RENNES

ÉCOLE DOCTORALE N° 638
Sciences de la Matière, des Molécules et Matériaux
Spécialité : *Science des Matériaux*

Par
Bruno CUCCO

Ab-initio Modeling of Photo-Active Materials Beyond Conventional Lead Halide Perovskites

Thèse présentée et soutenue à Rennes, le 27 Octobre 2023
Unité de recherche : Institut des Sciences Chimiques de Rennes

Rapporteurs avant soutenance :

Marie-Liesse DOUBLET — Directrice de recherche CNRS, Université de Montpellier
Leonidas TSETSERIS — Professeur, National Technical University of Athens

Composition du Jury :

Président :	Regis GAUTIER	Professeur, Université de Rennes
Examinateurs :	Lucia REINING	Directrice de recherche CNRS, École Polytechnique Palaiseau
	Michael SALIBA	Professeur, University of Stuttgart
Dir. de thèse :	Mikaël KEPENEKIAN	Chercheur CNRS, Université de Rennes
	George VOLONAKIS	Professeur Junior, Université de Rennes

ACKNOWLEDGEMENTS

First, I would like to deeply thank my parents **Valmir Cucco** and **Roselene Cerutti**, my sister **Silvia da Silva Cucco** and my brother-in-law **Anderson Santos Nunes** for all the love, dedication and support in every aspect of my life. None of this work could have been done without you and every word in this document is dedicated to you. I love you all unconditionally.

I would like to thank my supervisors **Mikaël Kepenekian** and **George Volonakis** for all the support and everything you taught me. I couldn't have wished for better tutors and all the opportunities and experiences you provided to me are priceless. Your efforts helped me grow not only as a researcher but also as a person. Thank you very much.

I would also like to thank all the members from the perovskite group at the Université de Rennes. In special, Professor **Jacky Even** and Dr. **Claudine Katan** for the guidance in all stages of my PhD. I also acknowledge all the members of the CTI group and colleagues from the Institut des Sciences Chimiques de Rennes.

I would like to thank Dr. **Claudio Quarti** and Professor **Feliciano Giustino** for hosting me as a visiting scholar in their group. I have an immense respect for both of you as researchers and also as a person. I feel very lucky for these experiences and I learned a lot from you. Thank you very much.

I woud like to thank all the ISCR staff for their willingness and friendliness throughout these three years.

Last but not least, I would like to thank the Université de Rennes, the ENSCR, LUMOMAT and also the doctoral school S3M for all the financial support, which made my visiting scholar period and conferences participation possible. All these experiences were key for my professional formation and I am very grateful.

TABLE OF CONTENTS

CHAPTER 1

INTRODUCTION

1.1 The Perovskite Structure

In 1839 Gustav Rose discovered a new inorganic compound with the chemical formula $CaTiO_3$ [1]. The mineral is shown in Figure 1.1(a), and was found to crystallize in a unique lattice, which consists of a three-dimensional network of TiO_6 corner-sharing octahedra with the large Ca atoms filling the space between as shown in Figure 1.1(b). This lattice is generally described by the chemical formula AMO_3, where at the A-site is typically a dication (e.g. Ca^{2+}), at the center of the octahedron M-site a tetravalent metal (e.g. Ti^{4+}), and O is the position of the oxygen atoms at the corners of the octahedron (i.e., O^{2-}). This unique crystal structure was named "perovskite" after the Russian mineralogist Lev Perovski and it is today used to describe materials that share the same prototypical crystal structure of $CaTiO_3$. AMO_3 perovskites (i.e. oxide perovskites) like $SrTiO_3$, $BaSnO_3$ have been extensively investigated for many decades

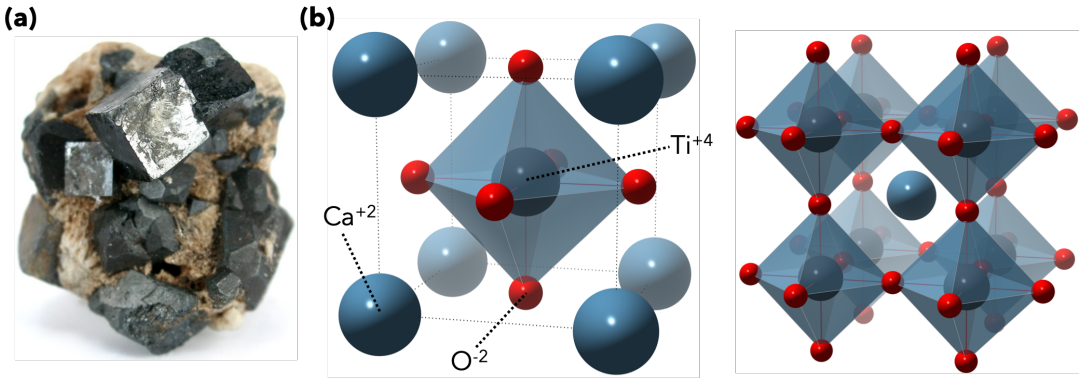

Figure 1.1 – Illustration of the $CaTiO_3$ (a) mineral and (b) crystal structure. The network of corner-sharing octahedra expands in three dimensions. The Ca atoms are found trapped within the octahedra cages, the O atoms are found at the corners of the octahedra, and the Ti atoms are located at the center of the octahedra in coordination with the O atoms. The mineral picture was adapted from the Mindat database [2].

now, for various applications such as high-temperature superconductors [3], magnetic recording heads [4], and transparent conductive oxides [5, 6]. It is worth noting that the majority of the currently known perovskites are oxides, accounting for 68% of these compounds [7].

1.2 Halide-based Perovskites

Oxide perovskites exhibit large band-gaps and are not particularly interesting for photoactive applications, with very few exceptions [8]. This is not the case for another type of perovskites that are formed with halogen atoms at the corners of the octahedron, known as halide perovskites. These materials were first reported back in 1893 with the pioneering work of H. L. Wells *et al.*, where the authors report the synthesis of a series of inorganic halide perovskites, among them prototypical compounds like $CsPbCl_3$ and $CsPbBr_3$ [9]. Many halide-based perovskites exhibit low band-gaps well within the visible range, and have drawn significant attention in recent years for opto-electronic due to their highly tunable optical and electronic properties. In terms of structure, perovskite materials are known to undergo temperature-dependent phase transitions, which are characterized by octahedra tilting. For example, $CsPbBr_3$ as illustrated in Figure 1.2, exhibit a cubic (α) and tetragonal (β) lattice phases that are skewed towards higher temperatures, while at low-temperature one can expect two orthorhombic phases, the black (γ) phases. These phases play an important role in the different applications of perovskites and are deeply connected to lattice vibrations and the highly anharmonic nature of perovskites [10, 11].

Besides all-inorganic materials, it is also possible to synthesize hybrid organic-inorganic halide perovskite. The first report of a hybrid perovskite material was given by Kojima *et al.*, via the synthesis of methylammonium (MA) based perovskites such as $CH_3NH_3PbBr_3$ ($MAPbBr_3$) and $CH_3NH_3PbI_3$ ($MAPbI_3$) [12]. Later works developed by Turren-Cruz *et al.* also reported the synthesis of formamidinium (FA) based perovskites [13]. However, since its early reports FA-based perovskites are known to be highly unstable, rapidly crystallizing into photoinactive non-perovskite phases [14]. Subsequent works by Saliba *et al.* demonstrated the possibility of stabilizing FA-based perovskites via the introduction of a mixture of different cations (Cs^+, MA^+, FA^+) at the A-site [15].

All of these materials can be synthesized via a variety of techniques, including low-cost processes which consist of the mixture of the precursor salts in solution. Solution processing techniques like spin coating and printing offer low-cost and scalable approaches for fabricating perovskite films. These methods involve depositing precursor solutions onto substrates and

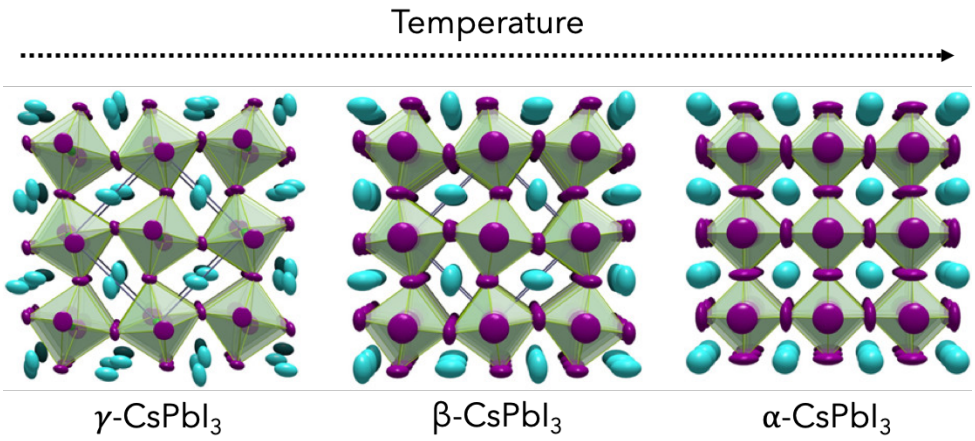

Figure 1.2 – Illustration of different phases of the AMX_3 perovskite crystal structure as a function of temperature. Here we illustrate the case of $CsPbI_3$. The cubic (α) and tetragonal (β) phases skew towards higher temperatures, while at low-temperature one can expect the orthorhombic (γ) phase. Figure adapted from reference [10].

subsequent annealing to induce crystallization. Vacuum deposition methods, including thermal co-evaporation and sputtering, provide precise control over film deposition and crystallization. One can optimize the film morphology, crystalline quality, and optoelectronic properties by carefully controlling the synthesis parameters, such as precursor composition, annealing temperature, and film thickness.

1.3 Dimensionality in Perovskites

Controlling synthesis parameters not only affects film quality and optoelectronic properties but can also lead to structural transformations to generate materials beyond conventional perovskites. Introducing precursor salts based on small A^+-site cations, such as the organic molecules MA and FA or the inorganic species Cs, will typically lead to the formation of three-dimensional perovskites discussed so far. However, one can also introduce organic salts based on large organic cations such as butylammonium (BA), leading to a break in the octahedra connectivity along specific directions. Depending on the synthesis parameters it is possible to generate layered, one-dimensional, and zero-dimensional perovskites, where the latter are usually referred to as quantum dots, shown in Figure 1.3. Hybrid organic–inorganic layered halide perovskites have drawn attention as high-performance semiconductors for a variety of applications, such as solar-cells, LEDs, lasers, and photodetector [16, 17]. These materials are categorized

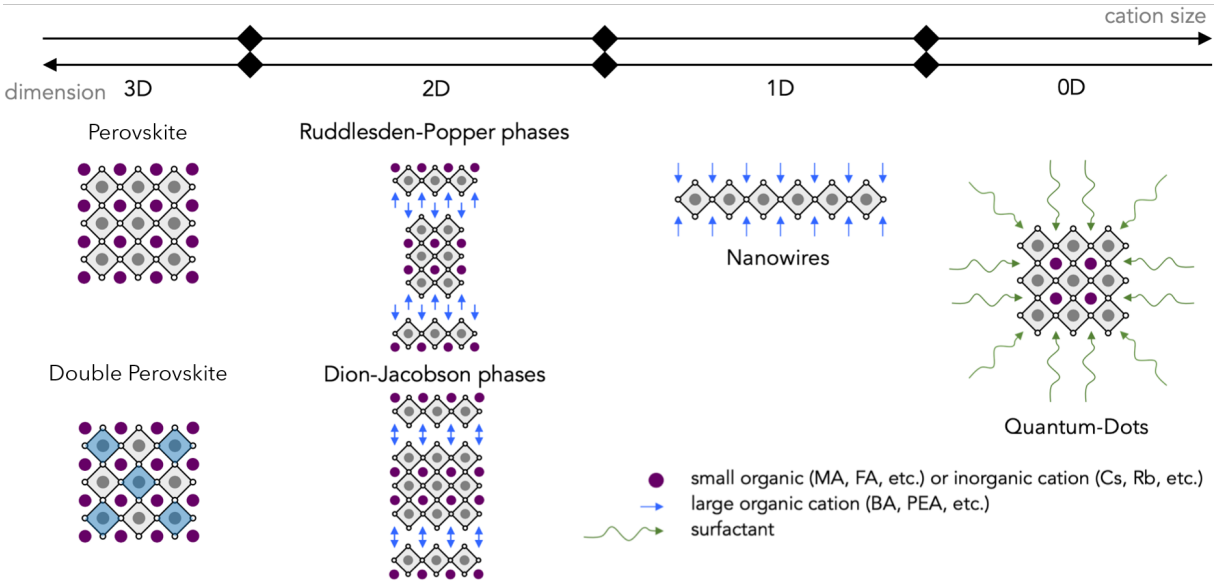

Figure 1.3 – The perovskite class of materials schematics according to dimensionality and cation size. The dimensionality decreases as the cation size increases.

based on their stacking orientations and the number of inorganic layers n, which allows fine-tuning of their optoelectronic properties via dielectric and quantum confinement effects [18, 19]. Layered systems also offer more versatility when it comes to compositional engineering, as the A-site cation can contain several types of organic cations [20, 21]. Moreover, introducing hydrophobic spacer cations in layered materials allows significant improvements in their stability while maintaining functionality [22], revealing two-dimensional compounds as potentially very stable materials. The challenge hereafter lies in achieving high efficiencies in layered perovskite devices without sacrificing stability. Recent developments in integrating three-dimensional and layered perovskites in a single device, i.e. 3D/2D heterostructures, have demonstrated the potential to combine the stability of layered materials with the efficiency of three-dimensional materials, paving the way for advanced multilayered device architectures [23].

1.4 Beyond Conventional Perovskites

While it is possible to obtain different perovskite dimensionalities via A^{+}-site cation engineering, similar structural transformations can also be induced via the M^{+2}-site. Heterovalent substitution of Pb (or Sn) by noble metals leads to the formation of a set of materials known as double perovskites [24]. These materials have a general stoichiometry given by $A_2^{+1}M^{+1}M'^{+3}X_6^{-1}$ and are structurally similar to AMX_3 perovskites, forming ordered rock-

salt structures as illustrated in Figure 1.3. One of the main advantages of double perovskites is the fact that it is possible to combine different types of metals for the M and M' sites, largely expanding the cluster of metal ions in halide perovskites. Materials such as $Cs_2AgBiBr_6$, $Cs_2AgBiCl_6$, $Cs_2AgInCl_6$, $Cs_2AgSbBr_6$ and $Cs_2AgSbCl_6$ have all been successfully synthesized and are shown to be stable [24–27]. More recently, layered double perovskites have also been synthesized and share the same advantages as their three-dimensional counterparts [28]. It is also possible to synthesize double perovskite materials on which one of the metal sites is vacant, known as vacancy-ordered double perovskites. These materials consist of a periodic rock-salt arrangement between the metal site M and vacant sites, similar to the double perovskites just introduced. Several three-dimensional perovskites such as $CsSnI_3$ and $CsGeI_3$ are known to be highly unstable in the AMX_3 form, and when exposed to air and moisture they can rapidly form vacancy-ordered materials such as Cs_2SnI_6 and Cs_2GeI_6 [29].

Besides double perovskites, other types of perovskite-like materials have been investigated. Ag/Bi double salts are metal halide materials that are composed of a periodic arrangement of edge-sharing octahedra. As their octahedra are not corner-sharing, they are usually regarded as perovskite-like materials. Yet, they still have electronic properties that can be associated with Ag/Bi double perovskites and are shown to be stable materials with tunable optoelectronic properties [30].

1.5 Electronic and Optical Properties

Part of the success of halide perovskites lies in their remarkable electronic structure. Figure 1.4(a) shows as an example the electronic band structure of the γ-phase of $MAPbI_3$ obtained via density functional theory. This material is predicted to exhibit a fundamental direct band-gap of 1.7 eV which is in good agreement with the experimental measurements for its optical band-gap (1.65-1.70 eV) [31, 32].

It is also possible to tune the band-gap value of these materials via halogen composition. It is known that the size of the halogen has a role in the size of the band-gap, with larger halogens (e.g. I) exhibiting smaller band-gaps and smaller halogens (e.g. Cl) exhibiting larger band-gap values [33]. In the case of $CsPbX_3$ (X=Cl, Br, I) nanocrystals the band-gap can be tuned via halogen composition within a range of 1.79 eV to 3.1 eV [33]. Theoretical calculations were also able to show that spin-orbit coupling has a major role in both the electronic and optical properties of perovskites, also being the source of effects such as Rashba splitting and Dresselhaus [34, 35]. Furthermore, analysis of these materials' electronic band structures also reveals

that both valence and conduction band edges exhibit highly dispersive bands, which indicates light and balanced charge carrier effective masses. This usually leads to higher charge carrier mobilities which favors charge carrier separation and collection, a highly important feature for many optoelectronic applications [36, 37]. The valence band edges are formed of hybridizations of Pb s-orbitals and I p-orbitals, while the conduction band edges are formed of hybridizations

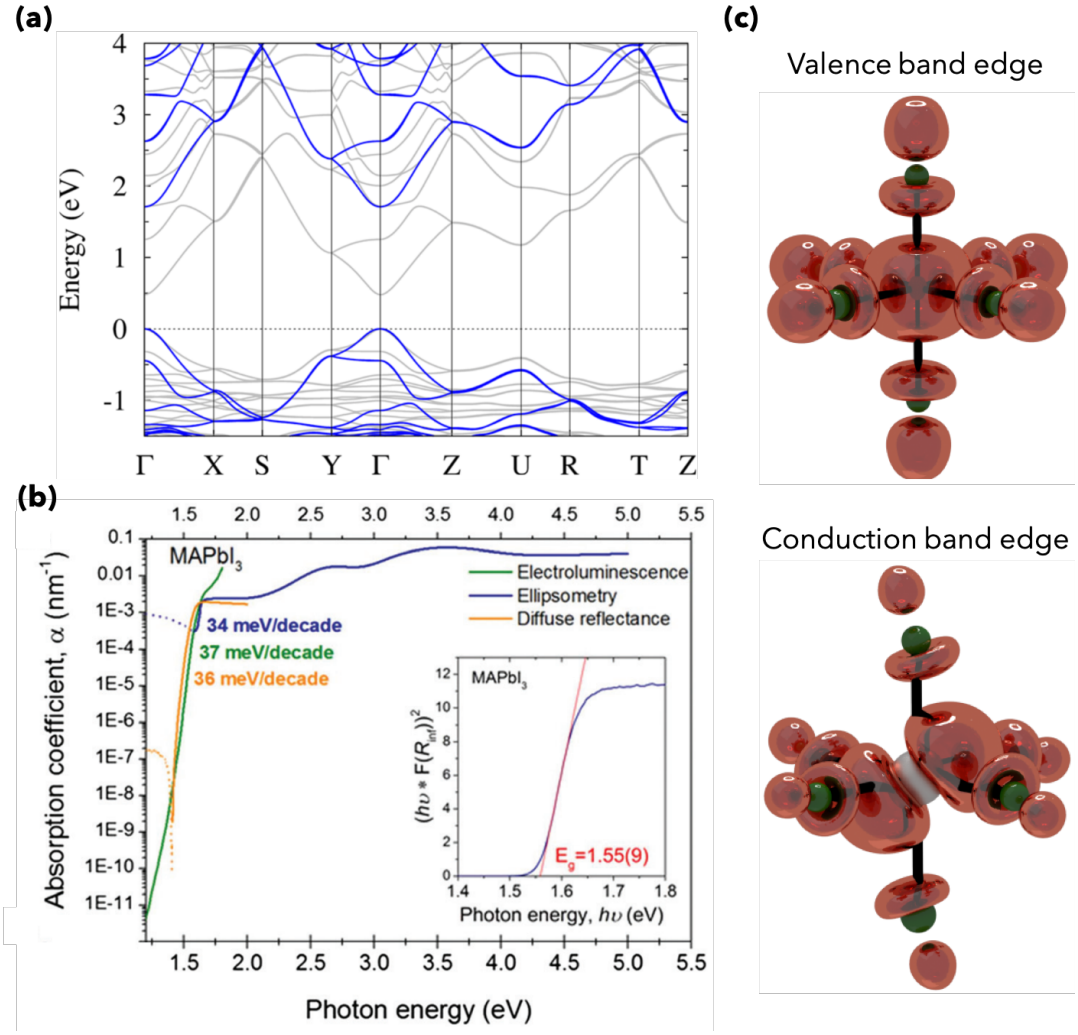

Figure 1.4 – (a) Band structure of orthohombic (Pnma) $CH_3NH_3PbI_3$ obtained from DFT+SOC (gray) and GW (blue). (b) The experimental absorption coefficient of $MAPbI_3$. (c) Illustration of the charge density at the band edges for Pb-based perovskites. Figure (a) is adapted from reference [38] and figure (b) from reference [39].

of Pb p-orbitals and I p-orbitals orbitals. The s-to-p optical transition of Pb gives rise to very sharp optical absorption onsets and large absorption coefficients [40], as shown in Figure 1.4(b).

All these ingredients combined turn halide perovskites into remarkable candidates for various photo-active applications, such as solar cells [41], light-emitting diodes (LEDs) [42], photocatalysis [43], water splitting [44], imaging and sensing [45], and X-ray detectors [46]. Halide perovskites have also been used for other types of applications such as transistors [47], memory devices [48] and superconductors [49]. In the following, I will focus on the photovoltaic and LED applications of perovskites.

1.6 Photovoltaic Applications

Perovskite-based solar cells (PSCs) are nowadays widely investigated due to their record high power conversion efficiencies (PCE) and potential low fabrication cost, which could revolutionize the photovoltaic industry. The first application of perovskites in photovoltaics was reported on the pioneering work of Kojima *et al.*, where the authors employed $MAPbX_3$ (X=Br, I) in dye-sensitized solar cells based on a layer of perovskite on mesoporous TiO_2 as charge carrier collector, achieving 3.8% PCE [12]. Later in 2012, two important breakthroughs occurred with the works of Lee *et al.* and Kim *et al.*, where the authors realized that the perovskite material could be stable in direct contact with the solid-state transporter, without the need for mesoporous TiO_2 [5, 50]. Later on, Ball *et al.* realized that the perovskite itself could also transport both holes and electrons [51]. In 2014, all these works culminated in a solar-cell device based on perovskite thin films without any mesoporous scaffold [52], achieving 10% PCE. It is important to note that the development of perovskite sensitized solar-cell devices did not cease immediately and efficiencies of over 15% were achieved in 2013 [53]. Yet, the application of a dye-sensitized media in PSCs gradually dropped as the efficiencies of all-solid-state devices spiked dramatically after the breakthrough works of 2014. Figure 1.5 shows the best solar cell PCE achieved for different technologies throughout the years for small-size solar cells, where emerging technologies are highlighted. Blue triangles and yellow circles represent perovskite-based technologies. To date, single-junction PSCs devices have achieved PCEs surpassing 26.1%, rivaling some of the most state-of-art technologies available [54], such as crystalline Si-based cells. More impressively, these high efficiencies were achieved in a very short period of time, leading to intense interest in this topic throughout the last decade. One of the advantages of PSCs is their ability to absorb a broad range of wavelengths, including both in the visible and the near-infrared regions. Furthermore, they exhibit high charge carrier mobilities and long carrier diffusion lengths, allowing for efficient conversion of sunlight into electricity [55]. Moreover, perovskites can be processed using low-cost techniques, enabling

scalable and cost-effective production of solar cells [56, 57].

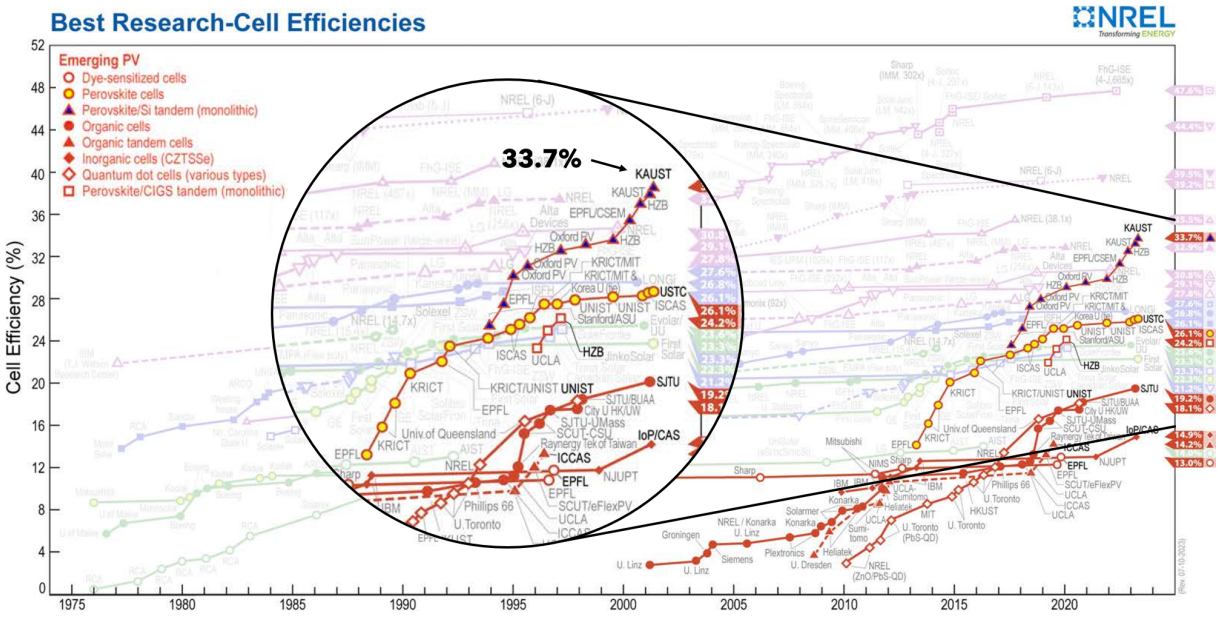

Figure 1.5 – NREL chart (September of 2023) containing the best solar-cell efficiencies for different technologies. Both blue triangles and yellow circles are perovskite-based technologies. Figure adapted from reference [54].

Metal halide perovskites have opened up new possibilities for highly efficient multi-junction solar cells. Tandems (multi-junction with two layers) based on perovskite/silicon, perovskite/CIGS (Copper indium gallium (di)selenide), and also perovskite/perovskite [58], have demonstrated their potential to surpass the efficiencies of single-junction cells achieving efficiencies surpassing 33.7%, as shown with the blue triangles in Figure 1.5. By harvesting the complementary absorption properties of different materials and optimizing the bandgap alignment, tandem solar cells can achieve higher PCEs than single-junctions and are actively investigated nowadays. Besides solar cells, layered perovskites have also been applied in LEDs, lasers, and photodetector applications [17].

1.7 Light-Emitting Devices

In addition, highly efficient perovskite-based LEDs have also been developed. LED device performance can be evaluated using a variety of metrics, such as external quantum efficiency (EQE), lifetime, and color purity. When it comes to perovskite-based LEDs, EQE is the most commonly used metric to assess device performance and it measures the ratio of photons emit-

ted from the device to the number of electrons passing through it. In 2014, Tan *et al.* developed the first perovskite-based LED that operates at room temperature, which exhibited a maximum external quantum efficiency of 0.76% in the infrared region and 0.1% in the green region [59]. Though these values are lower than those of OLEDs (20.35% [60]), the work encouraged the community to continue seeking ways to improve device performance. In late 2018, just four years after the works of Tan *et al.*, other research groups had already achieved EQEs of over 20% in perovskite-based LEDs for green [61], red [62], and infrared light [63]. As for perovskite-based solar cells, this rapid efficiency growth led both the research and industrial communities to remain interested in the potential of perovskite-based LEDs. One of the primary reasons for their success lies in their bright and tunable emissions across the visible spectrum [64]. Figure 1.6 shows colloidal perovskite $CsPbX_3$ nanocrystals (X = Cl, Br, I) in toluene solution under UV illumination. By engineering both the size of nanocrystals and their composition, it is possible to achieve tunable band-gap energies covering the entire visible spectral region with narrow and bright emissions. To our knowledge, the best EQE for a perovskite-based device was achieved by Ma *et al.* for green LEDs with an astonishing 25.5% [65].

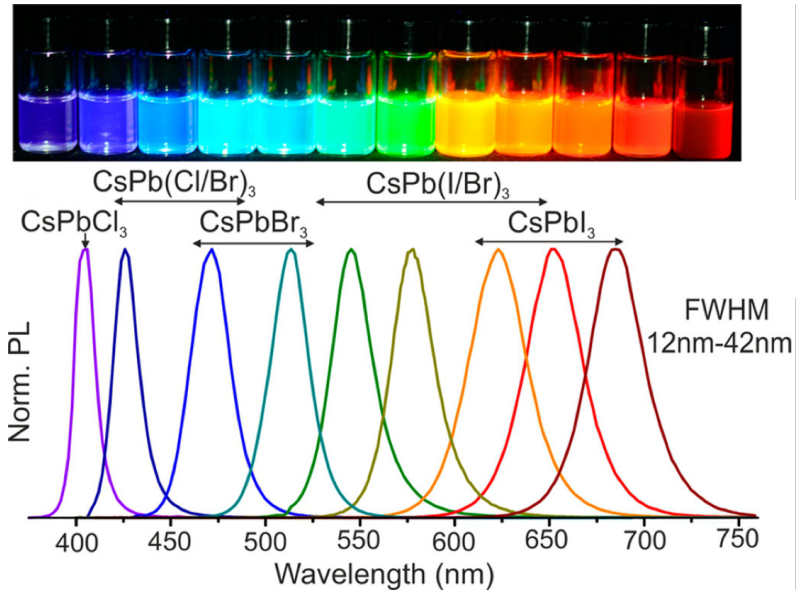

Figure 1.6 – Colloidal perovskite $CsPbX_3$ nanocrystals (X = Cl, Br, I) in toluene solution under UV illumination Figure adapted from reference [33].

1.8 Challenges and Outlook

Although the development of perovskite-based technologies happened fast, challenges remain for the commercialization of both PSCs and perovskite-based LEDs. Long-term stability, scalability, lead toxicity, and color stability are all critical points that need to be addressed. There is a growing effort to enhance the stability of PSCs by controlling their structure and developing strategies to control film morphology and crystallinity, via the introduction of additives [66], optimization of device architectures [67], and encapsulation of perovskite layers [68], which could all contribute to improving the long-term performance and reliability of PSCs and LEDs. Moreover, since their early developments concerns have been raised regarding the presence of lead in perovskite materials and its potential environmental and health impacts [69]. Lead is known to be a toxic heavy metal, and its use in perovskite solar cells and other optoelectronic devices has prompted a significant number of publications focused on developing lead-free alternatives [70]. These efforts aim to mitigate the potential risks associated with lead exposure, especially during the manufacturing, use, and disposal of perovskite-based devices, while maintaining the fantastic electronic properties brought by lead. The community strives to develop environmentally friendly and sustainable perovskite technologies by exploring alternative compositions and materials. For example, Pb-free Sn-based perovskites exhibit interesting electronic and optical properties but suffer from well-known instabilities [29]. Other approaches involve structural diversification such as the double perovskite materials [24] and vacancy-ordered double perovskites [29].

There are also several open questions regarding the fundamental mechanisms underlying all these applications. Dielectric and quantum confinement effects in lower dimensional perovskite structures are known to give rise to strongly bounded excitonic states [71], which play a major role in their optical properties. Moreover, due to substantial lattice distortions generated by the combination of strong charge carrier coupling with the soft perovskite lattice can also lead to the formation of self-trapped excitons [72] and polarons [73], which are hypothesized to be the primary mechanisms underlying the broad photoluminescence observed in some of these perovskites and a key feature in LED applications [74]. The electron-phonon coupling mechanisms in different perovskites are still not fully understood, and it is the root of the charge carrier transport properties that permeate any optoelectronic application. In addition, the role of lattice anharmonicity in the structural phase transition of perovskites and its effect on electronic, optical, and transport properties is still an open question [10, 11]. Both experimental and theoretical understanding of all these processes is crucial for enabling their potential applications.

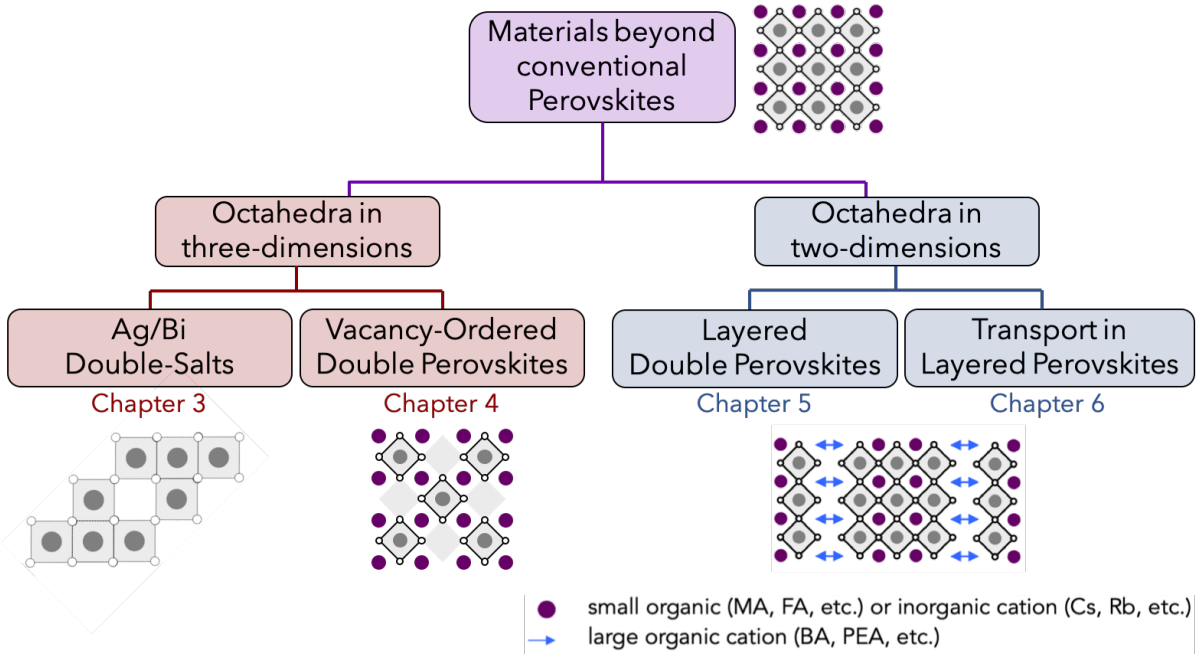

Figure 1.7 – Schematic connection between the different chapters in this thesis. The chapter numbers are also highlighted.

This thesis will focus on the employment of state-of-the-art computational approaches to address some of these challenges and assist in maturing these technologies for industrial and commercial applications. We will discuss important aspects of perovskite and perovskite-like materials going from their fundamental electronic structure to the investigation of excitonic properties and charge carrier transport. This introduction started with a broad overview of conventional perovskites, stating developments achieved in the past few years, their current state, and some of the challenges that need to be addressed. Figure 1.7 shows a schematic connection between this thesis' chapters. This thesis is organized according to the different types of materials investigated, with some of them classified as materials with octahedra connected in three dimensions, hereafter called "three-dimensional", and others with octahedra connected in two dimensions (layered). In each chapter, I will discuss the details of the electronic, optical, and stability properties of each of these materials and their suitability for optoelectronic applications. In Chapters 3 and 4, which cover three-dimensional materials, I will present two families of lead-free compounds beyond conventional perovskites. These chapters address both the stability and toxicity challenges stated previously. The first, namely Ag/Bi double salts, exhibit promising electronic and optical properties for photovoltaic applications. The second, namely vacancy-ordered halide double perovskites, are shown to be not suitable for photovoltaics, yet

could be fantastic building blocks for light-emitting applications. In Chapter 5, I will investigate lead-free layered double perovskite materials. I address the stability and toxicity issues present in perovskites while discussing critical differences in the electronic and optical properties of layered and three-dimensional systems. Finally, in Chapter 6 I will present how the dimensionality reduction affects the charge carrier transport in these materials, which is a fundamental property for any type of optoelectronic application, and it is directly related to the efficiencies of devices.

CHAPTER 2

METHODOLOGICAL FRAMEWORK

In this chapter, I will present the fundamentals of the methodological framework of this thesis. I start from the backbone of computational modeling of solid materials, the density functional theory (DFT), and move towards higher levels of theory. I will discuss the GW method to introduce dynamically screened Coulomb interactions, leading to a remarkable agreement between theory and experimentally measured band-gaps. Next, the Bethe-Salpeter formalism is presented as a tool to account for electron-hole coupling in ab-initio DFT and be able to predict complex phenomena such as the formation of exciton. Then, I will introduce the modern theory of electron-phonon coupling, which is fundamental to the understanding of charge carriers transport in periodic systems. Finally, I will introduce general concepts about Wannier functions and their utility within computational sciences as a powerful tool for accurate interpolations.

2.1 Density Functional Theory

The DFT is undoubtedly one of the most successful modern quantum many-body approaches developed to model materials. Such success comes from its effectiveness and predictive power, which opened the doors for the improvement of technologies in many fields such as optoelectronics [75, 76], spintronics [77], batteries [78], pharmacology [79] and nuclear physics [80].

The basis of DFT was established in 1964 by Hohenberg and Kohn in the work "Inhomogeneous Electron Gas" [81]. The fundamental concept of their findings is the demonstration of a connection between the ground state of a system, described by the many-body Schrödinger equation, and the correspondent electronic density. In equation 2.1 below, we show the many-body Schrödinger equation.

$$\begin{aligned}\Bigg[&-\sum_i \frac{\hbar^2}{2m_e}\nabla_i^2 - \sum_i \frac{\hbar^2}{2M_I}\nabla_I^2 + \frac{1}{2}\sum_{i\neq j}\frac{e^2}{4\pi\varepsilon_0}\frac{1}{|\mathbf{r}_i-\mathbf{r}_j|} \\ &+\frac{1}{2}\sum_{I\neq J}\frac{e^2}{4\pi\varepsilon_0}\frac{Z_I Z_J}{|\mathbf{R}_I-\mathbf{R}_J|} - \sum_{i,I}\frac{e^2}{4\pi\varepsilon_0}\frac{Z_I}{|\mathbf{r}_i-\mathbf{R}_I|}\Bigg]\Psi = E_{tot}\Psi.\end{aligned} \tag{2.1}$$

Here the indexes $\{i,j\}$ refer to electrons while $\{I,J\}$ to nuclei, m_e and M_I are the electron and nuclei masses, and r_i and R_I are the positions of electron and nuclei, respectively. The first two terms are related to the kinetic energy associated with electrons and nuclei. The third, fourth, and fifth terms are the Coulomb interactions between electron-electron, nuclei-nuclei, and electron-nuclei, respectively. Within the so-called Born-Oppenheimer or adiabatic approximation [82], which treats nuclei coordinates as *slow variables*, Hohenberg and Kohn demonstrated that the ground-state of a system of N electrons can be determined completely by the electronic density $n(\mathbf{r})$, rather than the wavefunction $\Psi(\mathbf{r})$. In practice, this approach is beneficial as it reduces the number of variables from a general $3N$ system to only 3. An important consequence of this statement is that the expected value of any single-particle operator $\hat{O}$ can be determined as a functional of the electronic density, that is, $O[n(\mathbf{r})] = \int d\mathbf{r} n(\mathbf{r}) O(\mathbf{r})$, instead of steaming from a wavefunction integral.

Using these concepts, Kohn and Sham showed that equation 2.1 can be reduced to the famous Kohn-Sham equation (KSE) shown in equation 2.2 below.

$$\left[-\frac{\nabla^2}{2} + V_n(\mathbf{r}) + V_H(\mathbf{r}) + V_x(\mathbf{r}) + V_c(\mathbf{r})\right]\phi_i(\mathbf{r}) = \varepsilon_i\phi_i(\mathbf{r}). \tag{2.2}$$

The KSE equation is obtained by mapping the many-body particle system in an independent par-

ticle framework and breaking each potential and energy term into manageable pieces. The terms $V_H(\mathbf{r})$, $V_x(\mathbf{r})$ and $V_c(\mathbf{r})$ stem from the coulomb interaction between electrons. The Hartree potential $V_H(\mathbf{r})$ arises from the effective electrostatic electron-electron interaction. The exchange potential $V_x(\mathbf{r})$ appears as a consequence of the Pauli exclusion principle, imposing a short-range repulsive interaction between electrons. The correlation potential $V_c(\mathbf{r})$ appears due to the many-body interaction between the electrons and is one of the most challenging aspects of the theory, as it incorporates all the effects that are lost when moving from the many-body system to the single particle problem introduced by Kohn and Sham. Effectively, the exchange-correlation energy functional $E_{xc}[n(\mathbf{r})] = E_x[n(\mathbf{r})] + E_c[n(\mathbf{r})]$ represents the energy difference between the full many-body system and the single-particle picture. Finally, the potential $V_n(\mathbf{r})$ describes an external potential acting over the single-particle system as a product of the electron-nuclei interactions.

Most of these terms do not pose problems to the solution of the Kohn-Sham equation, with the exception of how the $V_{xc}(\mathbf{r})$ exchange-correlation potential is treated. Many approximations for $V_{xc}(\mathbf{r})$ have been proposed throughout the years, such as the Local Density Approximation (LDA) [83] and Generalized Gradient Approximation (GGA) [84]. More complex variations of these functionals, such as the Local Spin Density Approximation (LSDA) [85], meta-GGA [86] and hybrid GGA [87] have also been proposed later on. These functionals can be generated via various techniques, such as Monte-Carlo calculations [88] and machine learning [89]. Furthermore, we can also introduce tools that can allow us to treat the interaction between core and valence electrons effectively. In the context of the DFT employed in this thesis, such treatment is done via pseudopotentials [90], which are essentially tools that allow us to exploit the energy separation between core electron states and valence states. Within this approach, the interactions between core and valence electrons are substituted by an effective potential, significantly reducing the number of variables in practical calculations. It is important to notice that this is not the only way to treat these interactions, and some implementations of DFT consider all electrons explicitly in the calculations [91].

Finally, it is also necessary to choose an appropriate representation for the electronic wavefunctions in our calculations. The most common basis sets for DFT calculations are the plane-wave basis and the atomic orbital basis. The plane-wave basis set relies on expanding the electronic wavefunctions as a combination of plane waves. This can be quite advantageous to describe periodic systems accurately and is well-suited to treat long-range electronic interactions [92]. Yet, when dealing with localized electronic features, many plane waves might be required making the method computationally demanding. The atomic orbital basis is based on

centering atomic orbitals around each atom in the system. It closely connects with tight-binding approaches, making it particularly interesting to study molecular systems or localized electronic states. Although this approach tends to be computationally efficient, one has to be very careful with the choice of atomic orbitals involved in the method. It is also important to notice that this type of basis set is not exclusive to molecular systems, yet more suitable for them. Other types of basis sets can also be found in the literature, such as Gaussian basis set [93] and Real-space grid basis set [94], but these will not be covered in this thesis.

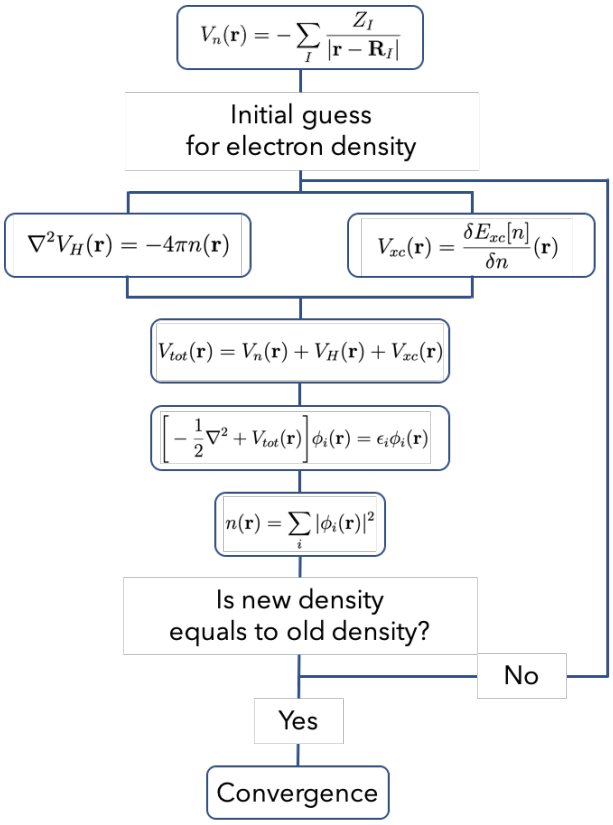

Figure 2.1 – Schematic flow-chart for the density functional theory self-consistent cycle.

Together all these approaches completely define the modern DFT and allow us to solve the KSE for systems containing hundreds and thousands of atoms. It is important to note that the solution of the KSE does not lead to the electronic wavefunction but to single-particle orbitals. An essential consequence of this statement is that the Kohn-Sham (KS) eigenvalues are not the required energies to add or remove electrons from the many-body system. Yet, it can be shown that there are relations between the true and KS eigenvalues, and quantities such as ionization energies and electronic affinity can be obtained [95].

A representation of the DFT self-consistent cycle is shown in Figure 2.1. At first, an initial guess for the electronic density is given and employed to solve a Poisson-like equation for the Hartree potential and to evaluate the exchange-correlation potential. Once all the different potentials are considered, the KSE is solved, and a new electronic density is calculated from the KS orbitals. This electronic density is compared with the initial density or the density of the previous step, and if they fall within a determined convergence criterion, the self-consistent cycle ends. If they do not, the new density is re-plugged at the beginning of the cycle until convergence is reached. With the final electronic density in hands, any observable can be calculated accordingly to the integral $O[n(\mathbf{r})] = \int d\mathbf{r} n(\mathbf{r}) O(\mathbf{r})$ discussed previously. The KS eigenvalues and eigenvectors can also be a basis for more complex theories and approaches.

2.2 The GW Method

DFT is a powerful tool and can be employed to obtain accurately a handful of properties for real systems, such as structural-related parameters. Yet, due to approximations involved within the theory, it is well known that DFT usually leads to underestimating band-gaps and poor prediction of excitation energies [96]. The GW method is likely one of the most famous approaches proposed to treat band-gap underestimation due to its solid theoretical framework and integrability with DFT codes. The main difference between the DFT and GW comes from how the many-body Schrodinger equation is treated. The GW method employs a many-body perturbation theory, where the central quantity is not anymore the electronic density but the so-called single-particle Green's functions. This quantity is defined as $G(\mathbf{r},\mathbf{r'};t-t') = -i\langle\Psi_0^N|\hat{T}[\hat{\psi}(\mathbf{r},t)\hat{\psi}^\dagger(\mathbf{r'},t')]|\Psi_0^N\rangle$, and can be interpreted as a complex generalized density, which describes the probability amplitude for the propagation of a particle from the $(\mathbf{r'},t')$ point in space-time to the point $(\mathbf{r},t)$, as illustrated in Figure 2.2(a). The operator $\hat{T}$ is known as a time operator and is simply describing if the trajectory is going from $(\mathbf{r'},t')$ to $(\mathbf{r},t)$ or the opposite. Its utility comes from the fact that it contains poles at the excitation energies of the many-electron system. This can be seen clearly as one applies a Fourier transformation from the time to the frequency domain leading to equation 2.3 below

$$G(\mathbf{r},\mathbf{r'};\omega) = \sum_n \frac{\psi_n^{N+1}(\mathbf{r})\psi_n^{N+1}(\mathbf{r'})}{\omega - (E_n^{N+1} - E_0^N) + i\eta} + \sum_n \frac{\psi_n^{N-1}(\mathbf{r})\psi_n^{N-1}(\mathbf{r'})}{\omega - (E_0^N - E_n^{N-1}) - i\eta}. \tag{2.3}$$

The excitation energies in the two term brackets represent those measured in photoemission experiments. The first term describes the injection of an electron by inverse photoemission, and

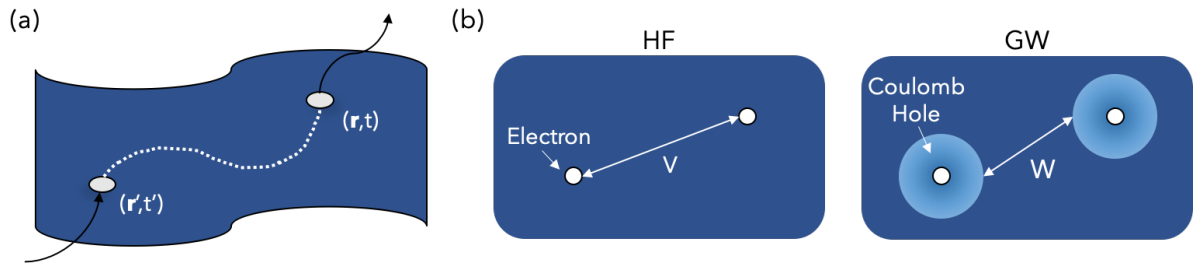

Figure 2.2 – (a) Physical representation of a Green's function. (b) Illustration of the GW quasiparticle concept. The interaction V between electrons at the DFT level is much stronger than the interaction W between quasiparticles at the GW level. We define a GW quasiparticle as the system formed by an electron plus its Coulomb hole. The black arrows indicate where the particle is injected and removed from the system. The white arrows indicate the Coulomb interactions V and W.

the second represents the emission of an electron via direct photoemission. The main goal of many-body perturbation theory is to determine the Green's function for a particular system.

One must remember that many different scattering processes and interactions can happen during the trajectory of a particle from a given point A to B. Formally speaking, it is necessary to account for all possible quantum mechanical paths, i.e., sum over all probability amplitude paths that the particle can propagate from A to B. The general interacting Green's function will assume the form given in Equation 2.4:

$$G = G_0 + G_0\Sigma G_0 + G_0\Sigma G_0\Sigma G_0 + ..., \tag{2.4}$$

where Σ is known as electronic self-energy or scattering potential. The first term represents the direct propagation of a particle from one point to another given by a non-interacting Green's function G_0. The second term describes the same process, but the particle is scattered during the path, while in the third term, two scattering processes are accounted for, and so on. By factoring out G in this equation, one derives the Dyson equation shown in Equation 2.5

$$G = G_0 + G_0\Sigma G, \tag{2.5}$$

which relates the Green's function of the real interacting system G with the Green's function of a non-interacting reference system G_0. Practically, Dyson's equation is not solved in this form but is instead recast into the form of an effective single particle equation of motion, known as

the quasiparticle equation, as shown in Equation 2.6

$$\hat{h}_0(\mathbf{r})\psi_n(\mathbf{r}) + \int \Sigma(\mathbf{r},\mathbf{r'};E_n)\psi_n(\mathbf{r'})d^3r' = E_n\psi_n(\mathbf{r}). \tag{2.6}$$

Here $\hat{h}_0(\mathbf{r})$ is essentially the KSE Hamiltonian given by Equation 2.2, while the second term is the heart of the GW method and incorporates the exchange and correlation processes in the system. The solution of the quasiparticle equation leads to the complex energies E_n, where the real part contains the excitation energies and the imaginary part carries the excitation lifetimes. Up to this point, this equation is very general, and there are no means to evaluate the self-energy term.

Within the well-established Hartree-Fock theory, one can expand the self-energy in the bare Coulomb interaction V up to the first order to obtain $\Sigma^{HF} = iG_0V$, which is called the Hartree-Fock approximation. Here Σ^{HF} describes the interaction between a system formed by two electrons interacting via a strong potential V as illustrated at the HF panel of Figure 2.2(b). Yet one might consider a much more realistic picture where an electron is directly added or removed from a many-electron system, similar to photoemission experiments. In this situation, the new electron (or holes) will polarise its environment by repealing nearby electrons (or holes) and creating a positively (or negatively) charged cloud in its vicinity, forming what is known as a Coulomb hole. The system formed by an electron (or hole) plus its Coulomb hole effectively behaves as a particle, which is known as a quasiparticle. Such structures possess all the properties of a standard particle and can move throughout the system, interacting with other quasiparticles. The key point behind this idea is that due to the reduced effective charge in comparison to an isolated electron, quasiparticles interact very weakly with each other via a screened interaction W, as illustrated at the GW panel of Figure 2.2(b). In this picture, one can do a similar expansion as shown before to obtain $\Sigma^{GW} = iG_0W$, which is, in fact, the GW approximation. One can also think of the GW as being a Hartree-Fock method with a dynamically screened Coulomb interaction. In practical calculations, the potential W can be tricky to evaluate and is usually constructed from the response function $\chi_0(\mathbf{r'},t';\mathbf{r},t) = -iG_0(\mathbf{r'},t';\mathbf{r},t)G_0(\mathbf{r},t;\mathbf{r'},t')$. The function G_0 and a wavefunction basis set can be obtained from mean-field theories, DFT or Hartree-Fock approaches.

When it comes to converging GW calculations it is necessary to be careful as there are several steps one needs to follow. As shown in equation 2.6, the term $\Sigma(\mathbf{r},\mathbf{r'};E_n)$ plays an essential role in the theory and can be decomposed into an exchange and a correlation part, i.e.

$\Sigma(\mathbf{r},\mathbf{r'};E_n) = \Sigma^x_{n\mathbf{k}} + \Sigma^c_{n\mathbf{k}}$. The exchange part of the self-energy term is shown in Equation 2.7.

$$\Sigma^x_{n\mathbf{k}} = -\sum_m \int_{BZ} \frac{d\mathbf{q}}{(2\pi)^3} \sum_G v(\mathbf{q}+\mathbf{G})|\rho_{nm}(\mathbf{k},\mathbf{q},\mathbf{G})|^2 f_{m(\mathbf{k}-\mathbf{q})}. \tag{2.7}$$

Here the number of reciprocal space G-vectors entering the sum in Equation 2.7 needs to be converged as it is system dependent. Analogously, the correlation part of the self-energy term shown in Equation 2.8 also needs to be converged.

$$\Sigma^c_{n\mathbf{k}} = i\sum_m \int_{BZ} \frac{d\mathbf{q}}{(2\pi)^3} \sum_{\mathbf{G},\mathbf{G'}} \frac{4\pi}{|\mathbf{q}+\mathbf{G}|^2} \rho_{nm}(\mathbf{k},\mathbf{q},\mathbf{G})\rho^*_{nm}(\mathbf{k},\mathbf{q},\mathbf{G'}) \int d\omega' G^0_{m\mathbf{k}-\mathbf{q}}(\omega-\omega')\varepsilon^{-1}_{\mathbf{G}\mathbf{G'}}(\mathbf{q},\omega'). \tag{2.8}$$

First, the number of states included in the sum over states m needs to be checked. Next, the static dielectric screening $\varepsilon^{-1}_{\mathbf{G}\mathbf{G'}}(\mathbf{q},\omega')$ also needs to be investigated. This function can be written as

$$\varepsilon^{-1}_{\mathbf{G}\mathbf{G'}}(\mathbf{q},\omega') = \delta_{\mathbf{G},\mathbf{G'}} + v_{\mathbf{G}}(\mathbf{q})[\chi^0_{\mathbf{G},\mathbf{G'}}(\mathbf{q},\omega) + \sum_{\mathbf{G}_1,\mathbf{G}_2} \chi^0_{\mathbf{G},\mathbf{G}_1}(\mathbf{q},\omega) v_{\mathbf{G1}}(\mathbf{q}) \delta_{\mathbf{G}_1,\mathbf{G}_2} \chi_{\mathbf{G}_2,\mathbf{G'}}(\mathbf{q},\omega)], \tag{2.9}$$

where $\chi^0_{\mathbf{G},\mathbf{G'}}(\mathbf{q},\omega)$ is given by:

$$\begin{aligned}\chi^0_{\mathbf{G},\mathbf{G'}}(\mathbf{q},\omega) = 2\sum_{c,v} \int_{BZ} \frac{d\mathbf{k}}{(2\pi)^3} \rho^*_{cv\mathbf{k}}(\mathbf{q},\mathbf{G})\rho_{cv\mathbf{k}}(\mathbf{q},\mathbf{G'}) f_{v\mathbf{k}-\mathbf{q}}(1-f_{c\mathbf{k}}) \times \\ \times \left[\frac{1}{\omega + \varepsilon_{v\mathbf{k}-\mathbf{q}} - \varepsilon_{c\mathbf{k}} + i0^+} - \frac{1}{\omega + \varepsilon_{c\mathbf{k}} - \varepsilon_{v\mathbf{k}-\mathbf{q}} - i0^+}\right].\end{aligned} \tag{2.10}$$

The sum over G-vectors appearing in Equation 2.9 and the sum over valence and conduction states in Equation 2.10 need to be converged simultaneously as they are interdependent. The number of unoccupied states appearing in these sums can converge slowly and many states might have to be included. Lastly, all these terms involve integrations over the reciprocal space and as so one should also check the GW results over different Brillouin zone samplings.

2.3 Electron-Hole Coupling and Optical Properties

The GW method has been extensively used throughout the past decade and has been shown to provide excellent agreement between experimentally measured and calculated band-gaps [97]. Yet, even if the method can accurately predict quasi-particle band-gaps for various extended systems it can fail drastically to predict optical band-gaps, especially for low-dimension sys-

tems [98–101]. The underlying reason is that in lower dimensions, due to both electronic and dielectric confinement effects, one can expect a strong coupling between electrons and holes, which gives rise to bounded quasiparticle states known as excitons. These can not be predicted by either standard DFT or GW method, as there is no formal coupling between electrons and holes in these theories [99]. These particles play a significant role in optical properties and can adversely affect the use of the material in solar-cell devices, for example, but positively impact applications for light-emitting devices. Nowadays, excitons are investigated for several applications such as transistors, valleytronics, LEDs, solar cells, quantum emitters, optically controlled information processing and fast/slow light applications [102, 103].

To account for the coupling between electrons and holes, one needs to take an extra step of complexity beyond the GW method and solve the Bethe-Salpeter equation (BSE) [104], shown in Equation 2.11

$$H^{vck}_{v'c'k'} = (\varepsilon_{ck} - \varepsilon_{vk})\delta_{vv'}\delta_{cc'}\delta_{kk'} + (f_{ck} - f_{vk})[2\bar{V}^{vck}_{v'c'k'} - W^{vck}_{v'c'k'}]. \tag{2.11}$$

Here the BSE is written in the space of transitions between valence and conduction states as a pseudo-eigenvalue problem for a two-particle Hamiltonian. The labels v, c, and k indicate valence, conduction, and momentum indexes, f_{ck} and f_{vk} are Fermi distribution functions, and $\bar{V}^{vck}_{v'c'k'}$ and $W^{vck}_{v'c'k'}$ are the electron-hole exchange and the screened interaction part of the BSE kernel. The competition between the repulsive exchange interaction and the attractive Coulomb interaction in the kernel will dictate whether an exciton state can be formed. Typically one employs the GW eigenvalues as parameters for the solution of the BSE due to the band-gap renormalization and electronic bands dispersion correction, which can strongly affect the exciton binding energies and its spatial localization.

As in the case of the GW method, the solution of the BSE is also demanding in terms of computational ressources. First, one needs to evaluate the static dielectric screening in the same way as presented in Equation 2.9. Next, we evaluate the macroscopic dielectric function according to Equation 2.12.

$$\varepsilon_M(\omega) \equiv 1 - lim_{\mathbf{q}\to 0}\frac{8\pi}{|\mathbf{q}|^2\Omega}\sum_{vc\mathbf{k}}\sum_{v'c'\mathbf{k}'}\left\langle v\mathbf{k}-\mathbf{q}|e^{-i\mathbf{qr}}|c\mathbf{k}\right\rangle\left\langle c'\mathbf{k}'|e^{i\mathbf{qr}}|v'\mathbf{k}'-\mathbf{q}\right\rangle\sum_{\lambda}\frac{A^{\lambda}_{cv\mathbf{k}}(A^{\lambda}_{c'v'\mathbf{k}'})^*}{\omega - E_{\lambda}}. \tag{2.12}$$

Here the number of bands included in the double summation of valence and conduction states must be carefully checked, as they will dictate the number of electron-hole pairs included in the calculation. In general, it is not necessary to include many pairs if one is interested in

computing optical properties just for the first set of transitions near the band edges. Yet, to achieve convergence across the entire spectra many states will be necessary. Next, the BSE kernel also contains summations that need to be checked. In the case of the exchange component shown in Equation 2.13, one can truncate the summation over reciprocal space G-vectors to save computational time, as these calculations can be extremely demanding.

$$\bar{V}^{vck}_{v'c'k'} = \frac{1}{\Omega}\sum_{\mathbf{G}\neq 0} v(\mathbf{G})\left\langle v'\mathbf{k}'\right|e^{-i\mathbf{G}\mathbf{r}}\left|c'\mathbf{k}'\right\rangle\left\langle c\mathbf{k}\right|e^{i\mathbf{G}\mathbf{r}}\left|v\mathbf{k}\right\rangle. \tag{2.13}$$

Analogously the screened coulomb interaction $W^{vck}_{v'c'k'}$ shown in Equation 2.14 also has a summation of G-vectors which can be truncated to save computational time.

$$W^{vck}_{v'c'k'} = \frac{1}{\Omega}\sum_{\mathbf{G}\mathbf{G}'} v(\mathbf{q}+\mathbf{G}')\varepsilon^{-1}_{\mathbf{G}\mathbf{G}'}(\mathbf{q})\left\langle v'\mathbf{k}'\right|e^{-i(\mathbf{q}+\mathbf{G}')\mathbf{r}}\left|v\mathbf{k}\right\rangle\left\langle c\mathbf{k}\right|e^{-i(\mathbf{q}+\mathbf{G})\mathbf{r}}\left|c'\mathbf{k}'\right\rangle\delta_{\mathbf{q},\mathbf{k}-\mathbf{k}'}. \tag{2.14}$$

Finally, one should also check the convergence of the obtained BSE spectra with respect to the number of reciprocal space points included in the calculation. In practice, the number of points necessary for the calculation will be proportional to the size of the exciton wavefunction in real space. Figure 2.3 shows the difference between the band-gaps E_g^{HSE} calculated via hybrid DFT-HSE06 calculations and band-gaps evaluated within G_0W_0 ($E_g^{G_0W_0}$) and BSE-G_0W_0 ($E_g^{BSE-G_0W_0}$). Here one can observe large discrepancies between the different methodologies.

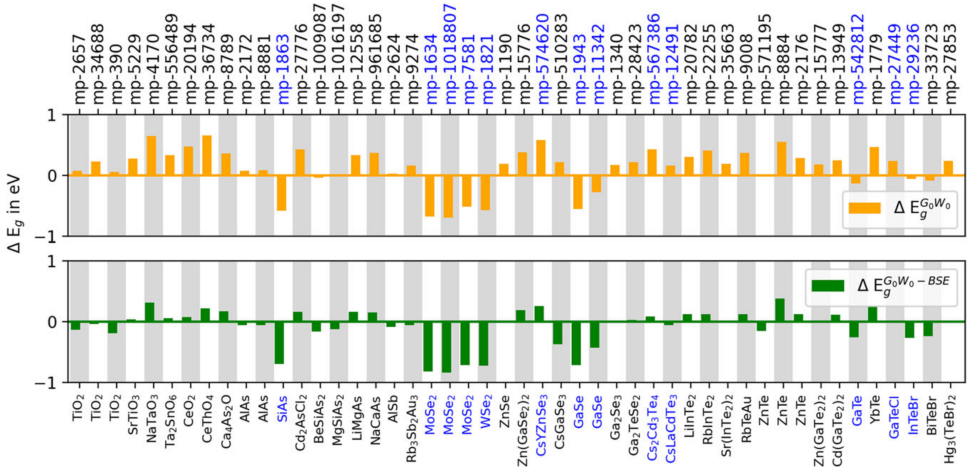

Figure 2.3 – Differences between E_g^{HSE} and $E_g^{G_0W_0}$ (orange) as well as $E_g^{BSE-G_0W_0}$ (green). The Materials Project id (mp-id) for each material is shown. Layered materials are labeled in blue. This figure was adapted from reference [98].

2.4 Ab-initio Charge Carrier Mobilities

As discussed in section 2.1, typically in DFT the atoms are kept frozen due to the clamped ions approximation. However, the mobility of electrons and holes inside a crystalline material is deeply connected with their interaction with the lattice's vibrations via electron-phonon coupling. To investigate phonons within DFT, one often employs the harmonic approximation and expands the total potential energy up to second order in the atomic displacements $\Delta\tau_{\kappa\alpha\rho}$, as shown in Equation 2.15.

$$U = U_0 + \frac{1}{2}\sum_{\kappa\alpha\rho;\kappa'\alpha'\rho'} \frac{\partial^2 U}{\partial\tau_{\kappa\alpha\rho}\partial\tau_{\kappa'\alpha'\rho'}}\Delta\tau_{\kappa\alpha\rho}\Delta\tau_{\kappa'\alpha'\rho'}, \tag{2.15}$$

where U_0 is the total energy of the ions in their equilibrium positions, and the derivatives are calculated in reference to the equilibrium structures. The atomic displacements $\Delta\tau_{\kappa\alpha\rho}$ can be calculated as [105]

$$\Delta\tau_{\kappa\alpha\rho} = \left(\frac{M_0}{N_p M_k}\right)^{1/2}\sum_{\mathbf{q}\nu} e^{i\mathbf{q}.\mathbf{R}_\rho} e_{\kappa\alpha,\nu}(\mathbf{q}) l_{\mathbf{q}\nu}(\hat{a}_{\mathbf{q}\nu} + \hat{a}^\dagger_{-\mathbf{q}\nu}). \tag{2.16}$$

Here the term $l_{\mathbf{q}\nu} = [\hbar/(2M_0\omega_{\mathbf{q}\nu})]^{1/2}$ represents the zero-point displacement amplitude, which depends on each specific phonon mode, frequency and phonon branch. The second derivatives of the total energies with respect to the atomic displacements shown in equation 2.15 defines the matrix of interatomic force constants (IFC), that is, $C_{\kappa\alpha\rho\kappa'\alpha'\rho'} = \partial^2 U/\partial\tau_{\kappa\alpha\rho}\partial\tau_{\kappa'\alpha'\rho'}$. By applying a Fourier transformation on the IFC matrix, one obtains the so-called dynamical matrix [106]:

$$D_{\kappa\alpha,\kappa'\alpha'}(\mathbf{q}) = (M_\kappa M_{\kappa'})^{-1/2}\sum_\rho C_{\kappa\alpha 0\kappa'\alpha'\rho} e^{i\mathbf{q}.\mathbf{R}_\rho}. \tag{2.17}$$

The eigenvalues of the dynamical matrix are precisely the phonon's vibrational frequencies. By solving the eigenvalue problem of Equation 2.18, we can obtain the eigenvectors, often called "normal modes of vibration." The Hermiticity of the dynamical matrix allows us to select eigenvectors $e_{\kappa\alpha,\nu}(\mathbf{q})$ which are orthonormal for each $\mathbf{q}$ vector. The ab-initio implementation of this scheme within the DFT framework is usually called Density Functional Perturbation Theory (DFPT). DFT and DFPT allow us to have information regarding electron and phonon contributions, which are the primary ingredients for investigating electron-phonon coupling.

$$\sum_{\kappa'\alpha'} D_{\kappa\alpha,\kappa'\alpha'}(\mathbf{q}) e_{\kappa'\alpha',\nu}(\mathbf{q}) = \omega^2_{\mathbf{q}\nu} e_{\kappa\alpha,\nu}(\mathbf{q}). \tag{2.18}$$

In this thesis, to evaluate charge carrier mobilities from ab-initio calculations, we rely on the linear response of the macroscopic current density to define the conductivity within a material [107], given by:

$$\sigma_{\alpha\beta} \equiv \left.\frac{\partial J_{M,\alpha}}{\partial E_\beta}\right|_{\mathbf{E=0}} = \frac{-e}{V_{uc}} \sum_n \int \frac{d^3k}{\Omega_{BZ}} v^\alpha_{n\mathbf{k}} \partial E_\beta f_{n\mathbf{k}}, \tag{2.19}$$

where $f_{n\mathbf{k}}$ is the out-of-equilibrium occupation function. In semiconductors, the conductivity will depend on the carrier concentration, i.e., the larger the carrier concentration, the larger the conductivity will be. To discuss a more intrinsic property of the material, we choose to employ the carrier drift mobility in our investigations, which is defined as $\mu_{\alpha\beta} = \sigma_{\alpha\beta}/en_c$, where n_c is the carrier density. These considerations lead to the final expression for the drift mobility:

$$\mu_{\alpha\beta} = \frac{-e}{V_{uc} n_c} \sum_n \int \frac{d^3k}{\Omega_{BZ}} v^\alpha_{n\mathbf{k}} \partial E_\beta f_{n\mathbf{k}}. \tag{2.20}$$

To calculate the partial derivative of the out-of-equilibrium occupation function with respect to the electric field, one has to solve the iterative Boltzmann transport equation (IBTE) [105, 108], given by:

$$\begin{aligned} \partial_{E\alpha} f_{n\mathbf{k}} = e\frac{\partial f_{n\mathbf{k}}}{\partial \varepsilon_{n\mathbf{k}}} v_{n\mathbf{k},\alpha} \tau_{n\mathbf{k}} + \frac{2\pi}{\hbar} \tau_{n\mathbf{k}} \sum_{m\nu} \int \frac{d\mathbf{q}}{\Omega_{BZ}} |g_{nm\nu}(\mathbf{k},\mathbf{q})|^2 \\ \times [(n_{\mathbf{q}\nu} + 1 - f^0_{n\mathbf{k}}) \delta(\varepsilon_{n\mathbf{k}} - \varepsilon_{m\mathbf{k}+\mathbf{q}} + \hbar\omega_{\nu\mathbf{q}}) \\ + (n_{\mathbf{q}\nu} + f^0_{n\mathbf{k}}) \delta(\varepsilon_{n\mathbf{k}} - \varepsilon_{m\mathbf{k}+\mathbf{q}} - \hbar\omega_{\nu\mathbf{q}})] \partial_{E\alpha} f_{m\mathbf{k}+\mathbf{q}}. \end{aligned} \tag{2.21}$$

Here the terms $\tau_{n\mathbf{k}}$ are the carrier lifetimes, $g_{nm\nu}(\mathbf{k},\mathbf{q})$ are the electron-phonon matrix elements, $f^0_{n\mathbf{k}}$ is the Fermi-Dirac distribution and $n_{\mathbf{q}\nu}$ is the Bose-Einstein distribution. In practice, we do not evaluate the carrier lifetimes directly but its inverse, known as scattering rates, as shown in Equation 2.22. This function carries the information of how strongly an electron at the band n and momentum $\mathbf{k}$ is scattered by the different vibration modes in the system.

$$\begin{aligned} \tau^{-1}_{n\mathbf{k}} = \frac{2\pi}{\hbar} \sum_{m\nu} \int \frac{d\mathbf{q}}{\Omega_{BZ}} |g_{nm\nu}(\mathbf{k},\mathbf{q})|^2 [(n_{\nu\mathbf{q}} + 1 - f^0_{m\mathbf{k}+\mathbf{q}}) \\ \times \delta(\varepsilon_{n\mathbf{k}} - \varepsilon_{m\mathbf{k}+\mathbf{q}} - \omega_{\nu\mathbf{q}}) \\ + (n_{\nu\mathbf{q}} + f^0_{m\mathbf{k}+\mathbf{q}}) \delta(\varepsilon_{n\mathbf{k}} - \varepsilon_{m\mathbf{k}+\mathbf{q}} + \omega_{\nu\mathbf{q}})]. \end{aligned} \tag{2.22}$$

Both Equations 2.21 and 2.22 depends on the electron-phonon matrix elements $g_{nm\nu}(\mathbf{k},\mathbf{q})$. This term is responsible for introducing the coupling between electrons and phonons. It describes the scattering of an electron from the initial state $n\mathbf{k}$ to the state $m\mathbf{k}+\mathbf{q}$ via a phonon

with crystal momentum $\mathbf{q}$ in the branch ν. Formally these matrix elements are defined as $g_{nm\nu}(\mathbf{k},\mathbf{q}) = \left\langle u_{m\mathbf{k}+\mathbf{q}} | \Delta_{\mathbf{q}\nu} v_{SCF} | u_{n\mathbf{k}} \right\rangle_{uc}$, where the states $u_{n\mathbf{k}}$ are the Bloch periodic part of the KS wavefunctions and $\Delta_{\mathbf{q}\nu} v_{SCF}$ is the variation of the self-consistent potential for a given phonon mode $\mathbf{q}$ at the branch ν, as defined in Equation 2.23 [108].

$$\Delta_{\mathbf{q}\nu} v_{SCF} = \sum_{\kappa\alpha\rho} e^{-i\mathbf{q}.(\mathbf{r}-\mathbf{R}_\rho)} \sqrt{\frac{\hbar}{2M_\kappa \omega_{\mathbf{q}\nu}}} e_{\kappa\alpha,\nu}(\mathbf{q}) \frac{\partial V_{SCF}(\mathbf{r})}{\partial \tau_{\kappa\alpha\rho}}. \tag{2.23}$$

In practice, we need to interpolate $g_{nm\nu}(\mathbf{k},\mathbf{q})$ over extremely dense grids, as the convergence of transport properties is relatively slow concerning the Brillouin zone sampling. For this purpose, tools such as Wannier function interpolation can be critical, and we will discuss some general aspects of the method in the next section.

These are all the ingredients to perform charge carrier mobilities calculations from first principles. The Bloch wavefunctions, phonon modes, and self-consistent potential derivatives can be obtained within the DFT and DFPT methods, which entirely define the electron-phonon matrix elements. The matrix can then be used to calculate the electron-phonon scattering rates, which are necessary for the solution of the IBTE. Once the IBTE is solved, the charge carrier mobilities can be obtained via a simple Brillouin zone integration.

2.5 Maximally Localized Wannier Functions

Within this thesis, we will be thoroughly discussing the fundamental electronic properties of crystalline materials, i.e. periodic systems in space. The periodicity of solid materials allows us to express the electronic wavefunctions as the so-called Bloch waves, which are periodic functions in real space and also invariant to gauge transformations of the form

$$\tilde{\Psi}_{n\mathbf{k}}(\mathbf{r}) = e^{i\phi_n(\mathbf{k})} \Psi_{n\mathbf{k}}(\mathbf{r}), \tag{2.24}$$

where $\phi_n(\mathbf{k})$ is an arbitrary phase and n and k are band and momentum indexes, respectively. A more general way of representing this transformation can be obtained by considering unitary transformation matrices, which act over the Bloch orbitals, as shown in:

$$\tilde{\Psi}_{n\mathbf{k}}(\mathbf{r}) = \sum_{m=1}^{N} U_{mn}^{\mathbf{k}} \Psi_{m\mathbf{k}}(\mathbf{r}), \tag{2.25}$$

where N is the dimension of the matrix $U_{mn}^{\mathbf{k}}$.

The set of Bloch functions is composed of objects that are intrinsically localized in reciprocal space but delocalized in real space. By applying a Fourier transformation on Equation 2.25, one obtains a set of localized functions in real space known as Wannier functions [109], as shown in Equation 2.26.

$$w_n(\mathbf{r}-\mathbf{R}) = |\mathbf{R}_n\rangle = \frac{V}{(2\pi)^3}\int_{BZ}\sum_{m=1}^{N} U_{mn}^{(\mathbf{k})}\,|\Psi_{m\mathbf{k}}\rangle\, e^{-i\mathbf{k}\cdot\mathbf{R}} d\mathbf{k}, \tag{2.26}$$

where V is the unit-cell volume, $\mathbf{R}$ are real space coordinates, and n are Wannier function indexes. As in the case of Bloch functions, the Wannier functions are also ill-defined due to the arbitrarity of gauge choice. This poses a problem as multiple sets of Wannier functions can be obtained to represent the same physical system.

Throughout the literature, there are several techniques developed to reduce the arbitrarity behind the choice of the matrix $U_{mn}^{\mathbf{k}}$, such as the exploration of symmetry criteria or function analicity [110, 111]. In this same context, N. Marzari and D. Vanderbilt developed a methodology that chooses the appropriate gauge via a minimization procedure. The method consists in defining the spread Ω of a Wannier function as

$$\Omega = \sum_n \left[\langle \mathbf{0}n|r^2|\mathbf{0}n\rangle - \langle \mathbf{0}n|\mathbf{r}|\mathbf{0}n\rangle^2\right] = \sum_n \left[\langle r^2\rangle_n - \bar{\mathbf{r}}_n^2\right], \tag{2.27}$$

where r is the position operator and $|\mathbf{0}n\rangle$ are the Wannier functions at the unit-cell. This spread defines the localization of the Wannier functions in real space, and the goal of the procedure is to find the set of matrices $U_{mn}^{\mathbf{k}}$ that minimizes the spread Ω. The set of Wannier functions obtained from the minimization are known as Maximally Localized Wannier Functions (MLWF) [112] and the methodology has been implemented by the original authors in the Wannier90 code [113].

One of the most exciting aspects of the *wannierization* procedure, as it is usually referred to, is that it directly connects with real atomic orbitals since the Wannier functions are wavefunction representations in real space. This allows us to understand molecular orbitals and take advantage of the Wannier basis set to perform very accurate electronic band interpolations. Such interpolations have been applied in several fields of physics and chemistry, such as the study of topological insulators [114], electronic bands interpolation [113, 115], Bethe-Salpeter calculations [115] and transport calculations [116].

2.6 The Spectroscopic Limited Maximum Efficiency

The most classical parameter that is used to have a first glimpse of the photovoltaic potential and capabilities of a material is the so-called Schockley-Queisser limit (SQ)[117]. The SQ measures the maximum theoretical efficiency of a solar cell device using a simple single p-n junction under the illumination of a standard solar/black-body spectrum. Due to its simplistic approach and dependency only on the fundamental band-gap of a material, the approach has been widely applied in the investigation of new photovoltaic absorbers. Yet, the SQ theory does not consider dipole-forbidden transitions or the indirect band-gap character of some semiconductors. Moreover, the absorption coefficient of the material is taken into account as a step function of the form

$$\alpha(E) = \begin{cases} 1\,; & E \geq E_g \\ 0\,; & E < E_g, \end{cases}$$

where $\alpha(E)$ is the absorption coefficient and E_g is the band-gap. As so, a model that would be capable of incorporating the true band-gap nature and absorption coefficient of materials is desirable.

The Spectroscopic Limited Maximum Efficiency (SLME) was proposed by L. Yu and A. Zunger as a means to treat these problems and introduce ab-initio data directly into such models [118]. As on the SQ limit, the power conversion efficiency of a solar cell device can be expressed as $\eta = \frac{P_m}{P_{in}}$, where P_m represents the maximum power that can be generated by the device assuming that the total solar power reaching it is given by P_{in}. The latter can be obtained by integrating solar irradiation over the energies, that is, $P_{in} = \int_0^\infty E I_{sun}(E) dE$. The maximum power can be obtained through the maximization of the $P(V)$ power function with respect to the voltage V as follows:

$$P_m = max[J_{sc} - J_0(e^{eV/kT} - 1)]V_V.$$

Although here the expression is the same as in the SQ limit, the definitions of J_{sc} and J_0 are different. The absorptivity of the material is defined as $a(E) = 1 - e^{-2\alpha(E)L}$, where $\alpha(E)$ is the ab-initio evaluated absorption coefficient and L is the thin-film thickness [119]. The thickness dependence allows one to have a better understanding of the photovoltaic properties of a material in real devices. The short-circuit current can be determined as

$$J_{sc} = e \int_0^\infty a(E) I_{sun}(E) dE, \tag{2.28}$$

where e is the electron charge. Besides the thickness-dependent absorptivity, the fraction of

the radiative recombination current f_r is also taken into account (in SQ, $f_r = 1$) to compute the reverse saturation current J_0. Thus, not all photons that reach the solar cell device will be absorbed, and the rate of photon absorption will depend intrinsically on the band-gap nature of the material as follows

$$J_0 = \frac{J_0^r}{f_r} = \frac{e\pi \int_0^\infty a(E) I_{bb}(E,T) dE}{e^{\Delta/kT}}.$$

The radiative recombination current J_0^r is evaluated through the absorptivity and the black-body spectrum $I_{bb}(E,T)$, and $\Delta = E_g - E_g^{da}$ represents the difference between the fundamental band-gap E_g and the true dipole-allowed direct band-gap E_g^{da}. Introducing Δ allows us to differentiate materials by their optical type, such as indirect or dipole-forbidden direct band-gap materials, while f_r allows one to consider the fraction of radiative recombinating e-h pairs.

For the works done in this thesis, the SLME methodology was coded in Fortran using the Fortran Standard Library (https://stdlib.fortran-lang.org) to perform the required integrals and function minimization. Furthermore, a third-order spline method was used to interpolate the ab-initio absorption coefficient over the experimental energy grid of the AM1.5G solar spectrum. The reference Air Mass 1.5G Spectra was obtained from the U.S. Department of Energy (DOE)/NREL/ALLIANCE data repository (www.nrel.gov/grid/solar-resource/spectra-am1.5.html) complying with the legal requirements for its usage.

CHAPTER 3

AG/BI HALIDE DOUBLE SALTS

In this chapter, I will present our investigation of a class of lead-free Ag/Bi double salt materials. I will start by introducing their crystal lattice and some of the most commonly investigated compounds. Next, I will demonstrate the challenges of modeling these materials from a computational point of view and show that a careful analysis of their crystal symmetries is necessary. The models I developed will be compared side-by-side with the available experimental data and also with other methodologies in the literature. In the following, I will use our models to evaluate these materials' electronic and optical properties and finalize the chapter by giving insights into their photovoltaic performance and possible pathways to optimize devices.

In 2017, a stable class of Ag/Bi lead-free halide materials with stoichiometry $Ag_aBi_bI_x$ (where x = a + 3b) were proposed as promising candidates for photovoltaic applications, exhibiting suitable optical band-gaps in the visible range around 1.4 eV and 2.0 eV [30, 120]. These materials are composed of a mixture of two salts, AgI and BiI_3. Turkevych *et al.* [30] coined the term "Rudorffites" for these compounds, inspired by Walter Rüdorff's pioneering work on $NaVO_2$, which shares a similar crystal lattice structure [121]. Ag/Bi double salts belong to a class of materials that are easily processable and have been successfully synthesized via various techniques such as spin coating [56], thermal coevaporation [57], and solution atomization to produce aerosols [122]. Among these materials, $AgBiI_4$ and Ag_3BiI_6 have emerged as exciting candidates, being successfully integrated into solar cell devices and achieving remarkable short-circuit currents of 10.7 mA/cm^2 [30, 123], and PCE of up to 5.6% for outdoor devices [124] and 5.17% for indoor devices [123]. These PCE values are among the highest reported for lead-free and perovskite-like materials, excluding the less stable Sn-based materials [125]. Besides the $AgBiI_4$ and Ag_3BiI_6 one can also find other members of the Ag/Bi double salts that have been synthesized, such as the Bi-rich compound $AgBi_2I_7$ and the Ag-rich compound Ag_2BiI_5. Materials that are skewed towards the Bi-rich side, such as $AgBi_2I_7$, tend to exhibit lower performance in optoelectronic devices [30, 56]. However, they have been successfully applied as alternatives for sensitive and stable X-ray detection [126]. Furthermore, these double salts have been employed as photo-responsive electrochemical capacitors [127] and memory logic operators [128]. Despite incorporating these materials in optoelectronic devices, there has been practically no thorough investigation of their electronic structure. Xiao *et al.* was the first to report the band structure of $AgBiI_4$, employing a cubic $Fd\bar{3}m$ cell with ordered Ag and Bi atoms [129]. In 2017, Sansom *et al.* introduced the density of states for $AgBiI_4$ by considering the lowest energy structure of Ag/Bi ordering in a super-cell [130]. The limited number of theoretical works on these materials can be attributed to the difficulty in precisely determining the positions of Ag and Bi atoms based on the available structural data, which poses a challenge for ab-initio calculations.

3.1 Structural Propeties

To gain a deeper understanding of this issue, it may be helpful first to establish a link between ABX_3 perovskites and Ag/Bi double salt materials. In the case of ABX_3 perovskites, the heterovalent substitution of two Pb^{+2} by a monovalent Ag^{+} and a trivalent Bi^{+3} leads to the formation of Ag/Bi double perovskites, such as Cs_2AgBiX_6 [24], as shown in the corner-

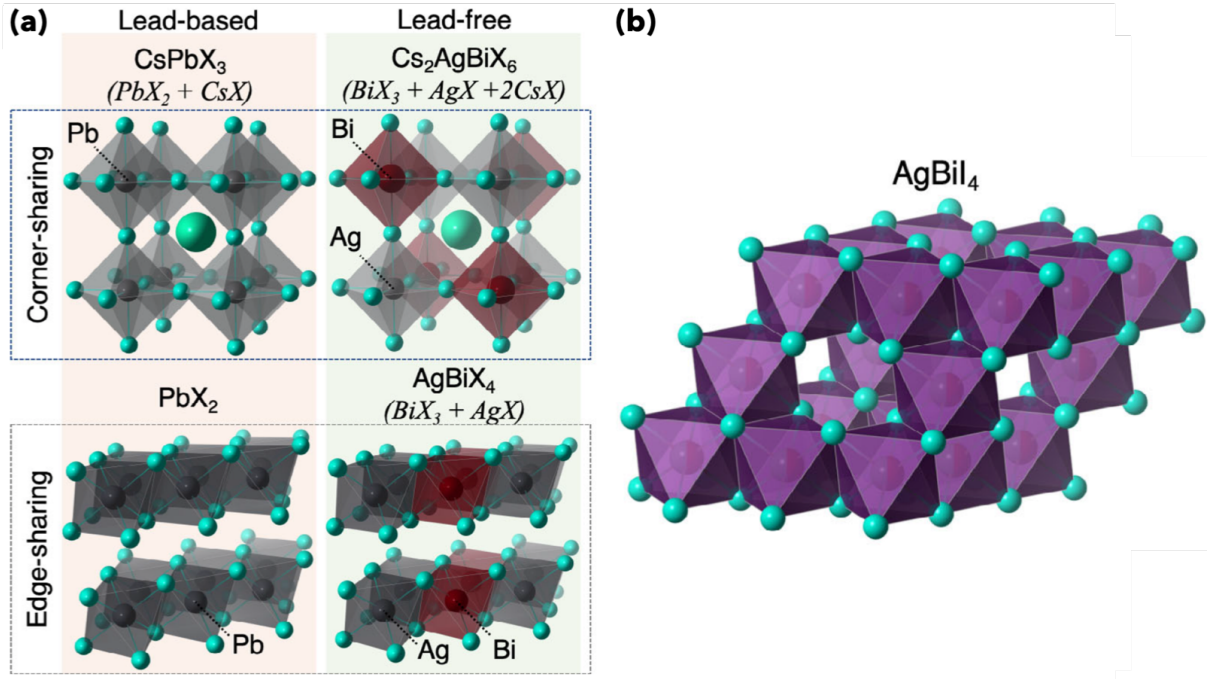

Figure 3.1 – a) Schematics between corner-sharing lead-based and lead-free Ag/Bi perovskites and the edge-sharing lead-based and Ag/Bi halide double salts (PbX_2 corresponds to the 2H-PbX_2 polytype). b) Crystal structure of $AgBiI_4$ made of partially occupied Ag/Bi sites and vacancy sites. Figure adapted from reference [131].

sharing structures of Figure 3.1(a). Analogously one can also substitute Pb^{+2} in the simple salt, e.g., 2H-PbX_2, leading to the formation of an Ag^{+}/Bi^{+3} double salt, which like the Pb salt it also exhibit a network of edge-sharing octahedra, as shown in the edge-sharing structures of Figure 3.1(a). In reality, for iodides such $AgBiI_4$, the lattice does not form ordered layers of octahedra separated by a vacuum, but it arranges to create a 3D lattice that contains Ag, Bi, and vacancies (Δ), as shown in Figure 3.1(b). Because these double salts are formed by a mixture of Ag and Bi salts, an ample phase space of materials can be synthesized by varying the ratio of the precursor salts. Such structural diversity is made possible due to vacant sites, allowing charge neutrality for different Ag-to-Bi ratios. It is important to note that this is not the case for double perovskites, as there are no vacant sites but the third salt in the reaction (e.g. CsBr), which constrains the stoichiometry to form Cs_2AgBiX_6.

It is possible to derive the whole Ag/Bi double salt class of materials by starting from the general class $Ag_xBi_y\Delta_zI_w$, where x, y, z, and w denote the stoichiometry of each species. First, we have to associate the correct number of halogens per metal site for a crystal of edge-sharing octahedra, which leads us to the equation $x + y + z = 2w$. We then normalize the halogen

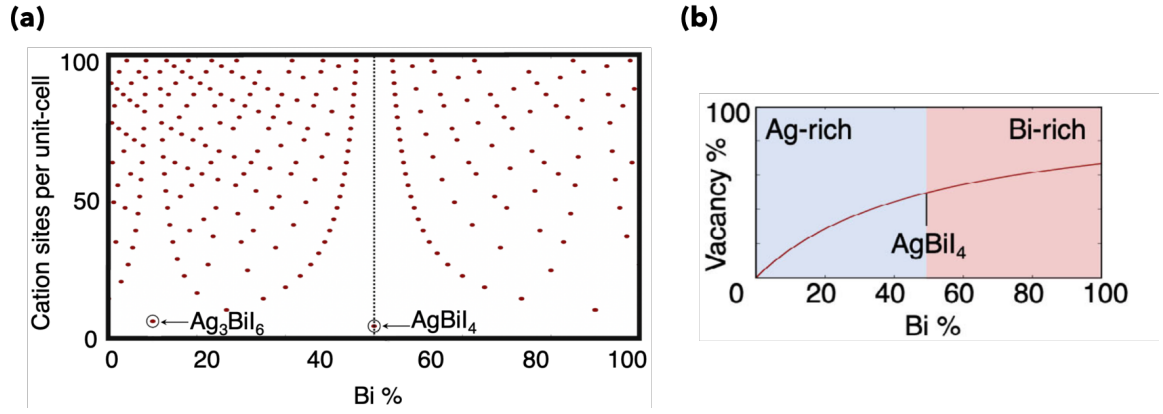

Figure 3.2 – (a) Representation of the Ag/Bi double salt materials' phase space. We illustrate the number of cation sites per unit cell as a function of the Bi to Ag ratio. Every dot corresponds to a compound within the Ag/Bi halide double salts class. b) Vacancy percentage in the double salt structures as a function of the Bi-to-Ag ratio. Figure adapted from reference [131].

occupation at the anion sub-lattice, simplifying the equation to $x+y+z=2$. Next, we impose charge neutrality based on the most commonly found nominal oxidation state of each species, that is, Bi^{+3}, Ag^{+1}, Δ^{+0} and I^{-1}, leading to the equation $3y+x=2$. These two equations define the Ag-Bi-I material's space, shown in Figure 3.2(a). $AgBiI_4$ and Ag_3BiI_6 exhibit the smallest unit-cells; for this reason and due to the available experimental data, we will mainly focus on these two compounds throughout this chapter. By combining both equations, one can also derive an expression between the vacancy ratio ($\Delta\%$) and the Bi-to-Ag ratio ($Bi\%$) given by $\Delta\% = 2Bi\%/(1+2Bi\%)$, as shown in Figure 3.2(b). This relation implies that many vacant sites must exist for Bi-rich materials to retain charge neutrality. For example, the precursor salt BiX_3 contains 75% vacant sites, which is precisely the case of the BiI_3 crystal.

The difficulty in assigning precisely the positions of Ag and Bi discussed before is related to the fact that all these compounds are very similar to each other. They exhibit almost indistinguishable diffraction patterns that can be resolved in different symmetry groups [30, 130]. One strategy adopted during the refinement of the experimental structures is the use of partially occupied atomic sites, which allows an accurate refinement, yet, it poses a challenge for atomistic modeling, as one needs the exact atomic coordinates of each atom. A simple way to visualize this problem is to take the experimental structure of $AgBiI_4$ refined by Sansom *et al.* [130]. This structure has a $Fd\bar{3}m$ (227) space-group with I atoms located at the 32 Wyckoff position and Ag and Bi atoms sharing the 16c sites with occupancy of 0.492 and 0.508, respectively. Assigning either Ag or Bi coordinates in the unit cell would inevitably break the symmetry of

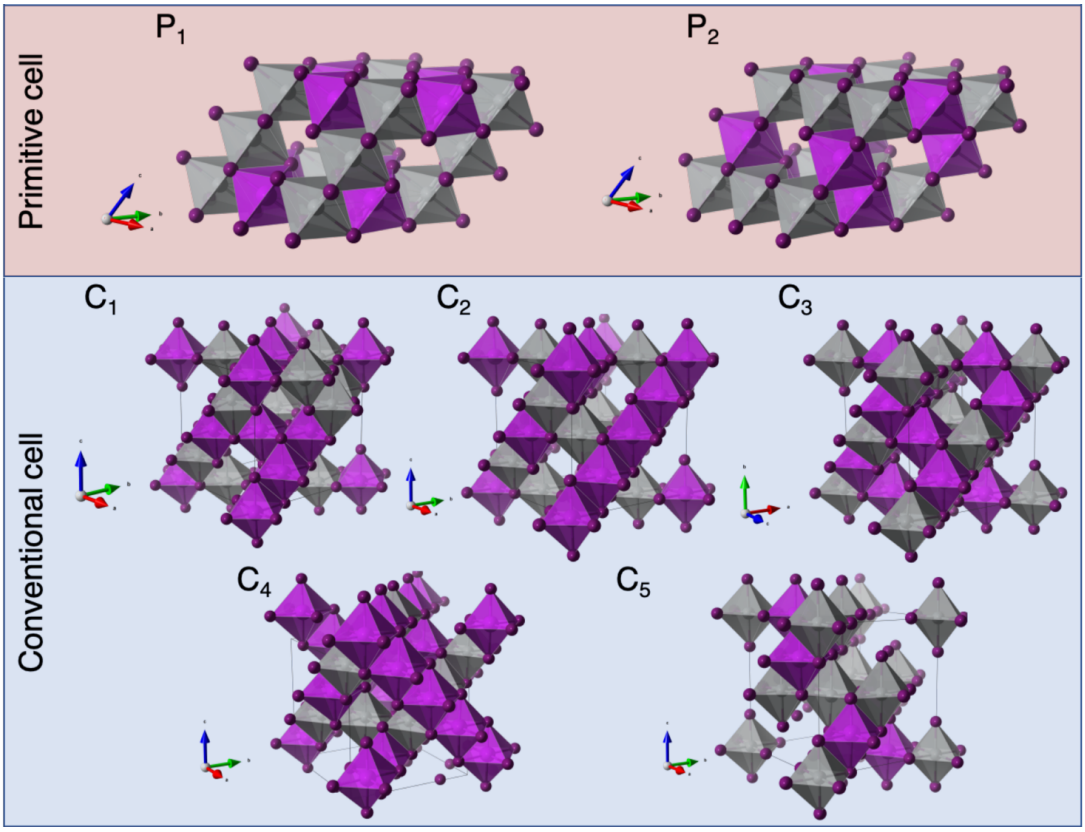

Figure 3.3 – Different atomic ordering for $AgBiI_4$ within the conventional cell (C_i) and primitive cell (P_j). Figure adapted from reference [131].

the experimentally reported structure because now half of the 16c sites will be occupied by Ag and the other half by Bi.

Typically, one resorts to supercell calculations, where different atomic arrangements are considered to deal with partially occupied atomic sites. To assess the impact of the order on the electronic structure of these materials, we perform DFT-PBE calculations for a series of different orderings obtained within the primitive cell and also from the conventional cell of $AgBiI_4$, as shown in Figure 3.3. Within the primitive cell, only two configurations are possible, while within the conventional cell, we identify five unique orderings. The atomic positions and lattice parameters of all configurations are optimized using PBE functionals, and more computational details can be found in the Appendix A.1. First, we compare each structure's X-ray powder diffraction pattern to the available experimental data, as shown in Figure 3.4. We observe noticeable disagreement between the different orderings, which differs from the experiments. More importantly, we observe significant variations of 40% between the calculated electronic

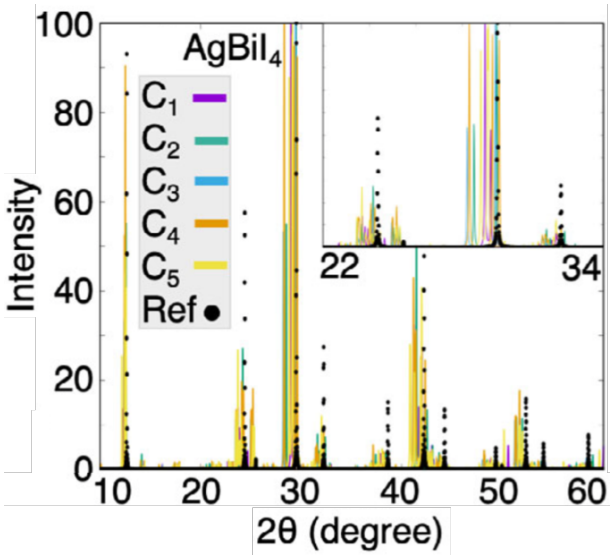

Figure 3.4 – (a) Calculated XRD patterns for different atomic orderings (C_i) within a super-cell of the Fd$\bar{3}$m (227) $AgBiI_4$ unit-cell. The inset shows a zoom around the largest intensity peak. Figure adapted from reference [131].

band-gaps, shown in Table 3.1. These results indicate that the supercell's atomic ordering and size can strongly affect the structural and electronic properties of $AgBiI_4$.

Table 3.1 – DFT-PBE band-gaps E_g for different orderings between Ag and Bi on the $AgBiI_4$ Fd$\bar{3}$m (227) conventional (C_i) and primitive (P_j) unit-cell, where $i = 1,...,5$ and $j = 1,2$.

Orderings	C_1	C_2	C_3	C_4	C_5	P_1	P_2
E_g (eV)	0.54	0.38	0.40	0.43	0.58	0.37	0.38

A different computational approach is to model these materials as random alloys. Random alloys are formed by a homogeneous mixture of the partially occupied atomic species. To model such systems we can employ methodologies such as the Special Quasi-Random Structures (SQS) [132] and the Virtual Crystal Approximation (VCA) [133]. We employ both methodologies as the SQS is developed to generate the structure that best mimics the figure's correlations of a perfectly random alloy. VCA introduces fictitious (virtual) atomic species that exhibit the averaged electronic configuration of the alloyed species in a single unit cell. These ideas are schematically shown at the top of Figure 3.5, while within SQS, one has two species randomly assigned in the lattice; within VCA, there is effectively just one virtual atom representing the average of Ag and Bi. By employing these approaches, we obtain a much better agreement of

XRD patterns than the supercell approach, as shown in Figure 3.5(c). In particular, SQS seems quite precise, while VCA leads to some shifts between experimental and calculated peaks. Although the structural properties are well reproduced within both approaches, the band structures shown in Figure 3.5(a-b) are predicted to be metallic in both cases, which is a direct contradiction to experimental data [130]. Thus, $AgBiI_4$ can not be modeled as a random alloy, and a method that can appropriately assign Ag and Bi atomic coordinates needs to be explored.

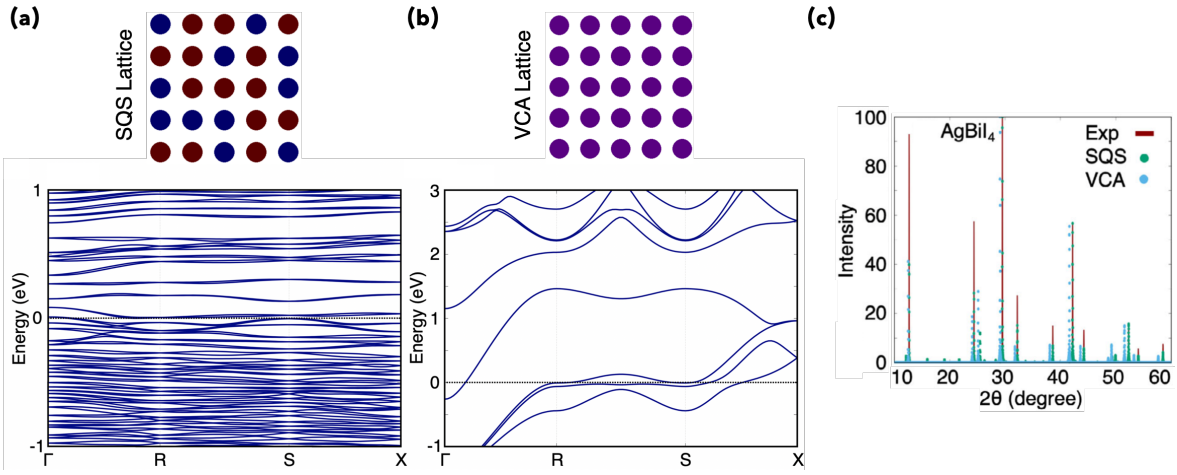

Figure 3.5 – (a) SQS and (b) VCA band structures for $AgBiI_4$ obtained within DFT-PBE calculations. The Fermi level is set to zero in both cases. (c) Calculated XRD patterns for $AgBiI_4$ modeled as a random alloy within the SQS and the VCA methods. Figure adapted from reference [131].

In order to accomplish that, we investigate the group/subgroup relationships for the identified materials' space groups. Given an arbitrary parent space group G, its symmetry operations can be reduced to a group H, which is a subgroup of G. During this process, the Wyckoff positions of the original parent group will split into different sites with different multiplicities. The process of splitting will vary depending on the transformation from the parent group to its subgroups. This is commonly referred to as Wyckoff Position Splitting (WPS) and was first investigated by H. Wondratschek [134]. We use the WPS to design alternative unit cells (e.g., a super-cell) that can describe the same initial structure but in a lower symmetry space-group (subgroup) representation that can retain most symmetry operations of the parent group.

Taking as an example the $AgBiI_4$ $Fd\bar{3}m$ (227) structure refined by Sansom *et al.*, when the $Fd\bar{3}m$ (227) space group is transformed into its Imma (74) subgroup, the original 16c Wyckoff position will be split in two sites with different symmetries but same multiplicities, as show in Figure 3.6(a). This transformation allows us to split the original site into two different ones that

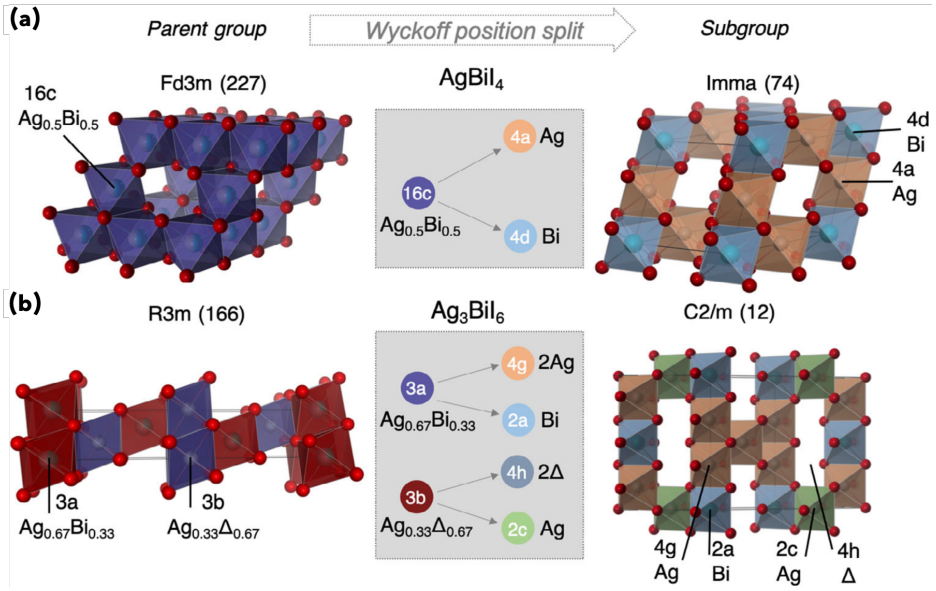

Figure 3.6 – Predicted WPS when a) $AgBiI_4$ is transformed from the parent group $Fd\bar{3}m$ (227) to its subgroup Imma (74) and b) Ag_3BiI_6 is transformed from parent group R3m (166) to its subgroup C2/m (12). The octahedra color matches the Wyckoff sites of the parent and subgroup space groups, as shown in the middle panel. Figure adapted from reference [131].

are symmetrically different but have the same multiplicity, allowing us to fit both Ag and Bi in two independent sites in the unit cell while maintaining their ratio. Hierarchically speaking, the Imma (74) is the subgroup that retains the most symmetries of $Fd\bar{3}m$ (227) while producing the desired splitting. To derive a matrix transformation that connects both cells, we let M be the rotation transformation matrix that connects the basis vectors of the parent space-group G and the subgroup H, such as that $H = GM$, and let m be the translation matrix which transforms the origin g of the parent space-group into h of the subgroup, such as $h = gm$. The matrices M and m that connects the $Fd\bar{3}m$ (227) to Imma (74) are

$$M = \begin{bmatrix} 1/2 & 1/2 & 0 \\ -1/2 & 1/2 & 0 \\ 0 & 0 & 1 \end{bmatrix} \text{ and } m = \begin{bmatrix} 1/4 \\ 1/4 \\ 0 \end{bmatrix}.$$

To validate this structural description, Figure 3.7(a) shows a comparison between the calculated XRD patterns of the experimental $Fd\bar{3}m$ (227) structure and the material modeled within the subgroup Imma (74) after optimizing the atomic coordinates. As the XRD patterns agree well, we also look at the calculated average Bi–I (3.08 Å) and Ag–I (3.09 Å) bond lengths on the reduced symmetry structure. These values are in excellent agreement with the measure-

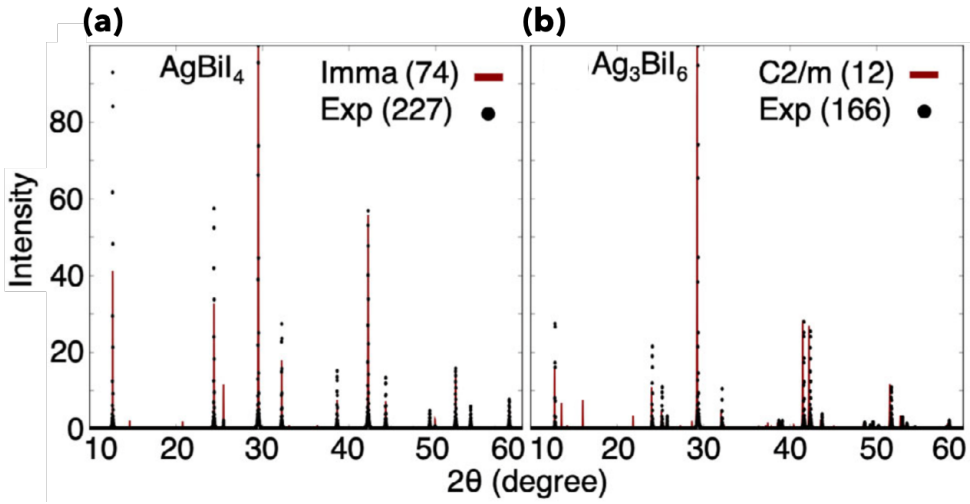

Figure 3.7 – (a) Calculated XRD patterns for models of (a) $AgBiI_4$ and (b) Ag_3BiI_6 in its subgroups using Wyckoff position splitting, respectively. Figure adapted from reference [131].

ments of Sansom *et al.* (3.06 Å) [130]. Moreover, Barone *et al.* developed a high-throughput approach using machine learning algorithms to screen $AgBiI_4$ structures and identify the most suitable atomic arrangements [135]. Considering a wide range of potential structures, crucial properties such as lattice parameters, simulated X-ray diffraction (XRD) patterns, the density of states, band-gaps, and bulk moduli are obtained through an ensemble average of the screened structures rather than a specific crystal structure. The values we calculated are also in good agreement with the results obtained by Barone *et al.* [135], which have Bi-I and Ag-I bond lengths of 3.14 Å and 3.09 Å, respectively. We employ the same approach to the Ag-rich compound Ag_3BiI_6 resolved by Oldag *et al.* [136] which has the R3m (166) space group. As shown in Figure 3.6(b), the experimental compound has the Wyckoff position 3a being partially occupied by Ag and Bi in ratios of 2/3 to 1/3, respectively, and the Wyckoff position 3b partially occupied by Ag and vacant sites in ratios of 1/3 to 2/3, respectively. We identify the C2/m (12) space group as the most symmetric subgroup of R3m (166) that can appropriately fit these occupancies. In this case, the WPS representation is also illustrated in Figure 3.6(b) and leads to four independent Wyckoff positions. As in the case of $AgBiI_4$, the subgroup structure also exhibits a good agreement in comparison to the experimental XRD data shown in Figure 3.7(b). We also compared the calculated radial distribution functions for the different models we discussed, and we note important differences in the interatomic distances even for atoms at short distances which can explain the highly structural dependent electronic properties, as shown in Figure 3.8. Analogously to the case of $AgBiI_4$, we also identify the matrices that connect the

parent and subgroup structures of Ag_3BiI_6 as

$$M = \begin{bmatrix} 1/3 & -3 & 0 \\ -1/3 & -3 & 0 \\ 2/3 & 0 & -1 \end{bmatrix} \text{ and } m = \begin{bmatrix} 0 \\ 0 \\ 0 \end{bmatrix}.$$

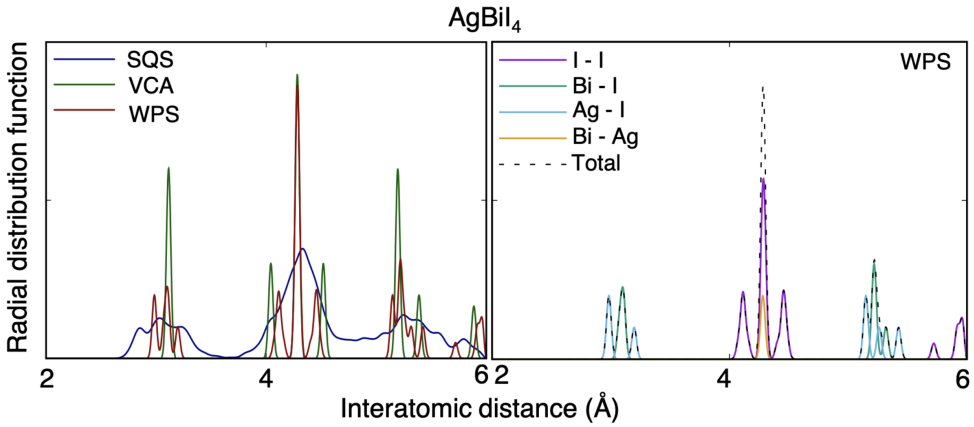

Figure 3.8 – The radial distribution functions evaluated for the three modeling approaches: special quasi-random structures, virtual crystal approximation, and Wyckoff position splitting. The decomposition of the WPS radial distribution function about each pair of atomic species is also shown. Figure adapted from reference [131].

3.2 Electronic Structure

Having established our methodology based on the WPS as appropriate for the structural description of Ag/Bi double salts, we move to investigate their electronic structure. Figure 3.9 shows the calculated electronic band structures and projected density of states (PDOS) for $AgBiI_4$ and Ag_3BiI_6 within DFT-PBE0 hybrid functional, which is known to overcome to a large extent the well-known band-gap underestimation of DFT. $AgBiI_4$ exhibit a 1.67 eV indirect band-gap between the Γ and R points. The calculated band-gap is in close agreement with the experimental value of 1.73 eV [130]. The conduction band minimum (CBM) is located at the R point. It is worth noticing that the band at the Γ point is only 14 meV higher in energy. Ag_3BiI_6 compound also exhibits an indirect band-gap, with valence band maximum (VBM) located at the X-point and CBM located at the K-point $(1/3, -1/3, 1/3)$ between the Γ–I path. We obtain a band-gap of 1.74 eV, in comparison to the experimentally measured band-gap of 1.83 eV [137]. The PDOS analysis shows that the VBM of both materials is mainly formed by

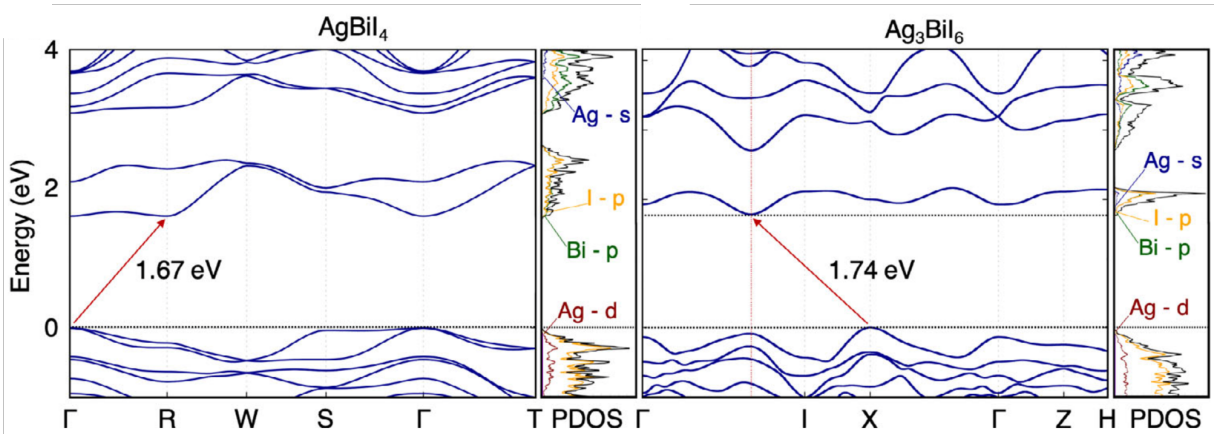

Figure 3.9 – Hybrid DFT-PBE0 band structures for $AgBiI_4$ (Imma (74)) and Ag_3BiI_6 (C2/m (12)). The CBM in (b) is located at the k-point $(1/3, -1/3, 1/3)$ between the Γ–I path and is shown with red dashed lines. The projected density of states is also shown. Figure adapted from reference [131].

hybridized I-5p and Ag-4d states, while the CBM is made of hybridized Bi-6p and I-5p orbitals.

Table 3.2 – Electron and hole effective masses for $AgBiI_4$ and Ag_3BiI_6.

	holes			electrons		
	m_1	m_2	m_3	m_1	m_2	m_3
$AgBiI_4$	0.59	0.69	1.27	0.65	0.24	0.69
Ag_3BiI_6	0.57	0.59	0.54	0.65	0.61	0.44

These observations reveal that the conduction band bandwidth is reduced when going from $AgBiI_4$ to Ag_3BiI_6 due to the reduction of Bi/Ag ratio, as Bi is the main contributor to the CBM. Interestingly these are also the same orbital characters observed for corner-sharing Ag/Bi double perovskites [24, 138]. These results suggest that even though the corner-sharing feature is lost, the electronic structure is still similar between these perovskite-like materials.

We compute the charge carrier effective masses at the band edges to quantify the electronic bands' dispersion. For $AgBiI_4$ we calculate an average hole effective mass of 0.77 m_0 and electron average mass of 0.42 m_0. For the Ag_3BiI_6 we obtain isotropic hole and electron effective masses of 0.57 m_0 and 0.55 m_0, respectively. Sansom *et al.* also report anisotropic effective masses for $AgBiI_4$ and show that the masses can vary more than 60% between different structural models (i.e., defect spinel and $CdCl_2$ in their case), which highlights the importance of having an appropriate structural model for these compounds. The effective mass components

for the two materials are shown in Table 3.2.

3.3 Optical Properties and Theoretical Performances

Next, we investigate the optical properties of the two materials. Figure 3.10 shows the calculated absorption coefficients for $AgBiI_4$ and Ag_3BiI_6. For comparison, we also include the absorption coefficient of the prototypical double perovskite $Cs_2AgBiBr_6$, a triple salt perovskite shown in Figure 3.1. The absorption onset of both Ag/Bi double salts are sharp and close to the calculated band-gaps E_g due to the first dipole allowed transition being very close in energy to E_g. In the case of the double perovskite $Cs_2AgBiBr_6$, the absorption onset is located at much higher energies, well above 2.3 eV, which is due to the significant difference between the indirect band-gap (1.98 eV) and the first allowed transition.

Having described the electronic and optical properties of these materials, we move now to the investigation of their potential as solar-cell absorbers. Here we employ the Spectroscopic Limited Maximum Efficiency (SLME) method proposed by L. Yu and A. Zunger [118], which allows us to have an explicit dependence on the calculated absorption coefficient of the material and its optical nature (See Chapter 2.6). Figure 3.10(b) shows the calculated SLME as a function of the thin-film thickness for $AgBiI_4$, Ag_3BiI_6 and $Cs_2AgBiBr_6$. We find that the two double salts are predicted to have higher efficiencies than the double perovskite and that $AgBiI_4$ can reach theoretical values above 25%. We also observe a steeper increase of the efficiency concerning the film thickness for the Ag_3BiI_6, with both materials reaching a plateau above 400 nm thickness. Interestingly, the Ag_3BiI_6 efficiency is higher than $AgBiI_4$ for thin-film thickness below 100 nm, which is consistent with its larger absorption coefficient. Yet, the higher efficiency of $AgBiI_4$ at larger thicknesses can be understood from the smaller band-gap exhibited by $AgBiI_4$, which leads to higher absorption of the infrared photons that are not absorbed by Ag_3BiI_6. This contribution becomes more important as one increases the thin-film thickness, while the shape of the absorption coefficient curve becomes less important. This can be seen from the expression $a(E) = 1 - exp(-2\alpha(E)L)$, where $a(E)$ is the absorptivity, $\alpha(E)$ is the absorption coefficient, and L is the thin-film thickness [118]. The calculated efficiencies are higher than those achieved by real devices, which is due to our models being defect-free and having perfect band alignments. Turkevich *et al.* [30] reported high performances for Ag_3BiI_6-based devices, yet, our results show that there is no intrinsic advantage of this material in comparison to $AgBiI_4$.

We also analyze the J-V curves obtained for different thicknesses (Figure 3.10(c)). Both

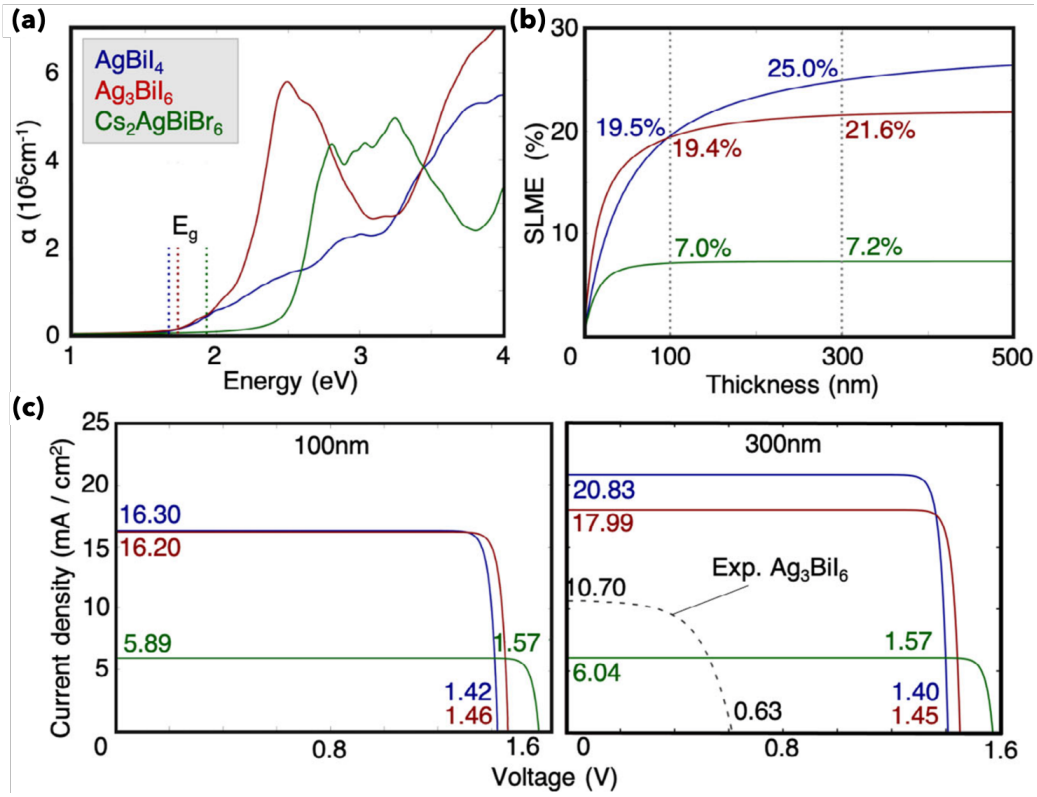

Figure 3.10 – a) Absorption coefficient of $AgBiI_4$ (Imma (74)), Ag_3BiI_6 (C2/m (12)), and $Cs_2AgBiBr_6$. The dotted lines indicate the band-gaps E_g. b) SLME as a function of the thin-film thickness for the three materials. Current density as a function of voltage (J–V plot) for a thickness of c) 100 nm and d) 300 nm. The black dashed curve represents the experimental curve obtained by Turkevich *et al.* [30] for a device containing Ag_3BiI_6. Figure adapted from reference [131].

Ag/Bi double salt materials exhibit identical characteristics for the 100 nm thickness. The V_{oc} for both materials are similar, which is related to their also similar band-gaps. For 300 nm, we observe an increase of the estimated J_{sc} for both, yet slightly more for $AgBiI_4$, which results in higher efficiency. When comparing to $Cs_2AgBiBr_6$, the Ag/Bi double salts exhibit slightly smaller V_{oc} values due to their smaller band-gaps, but significantly higher J_{sc}. We note that photovoltaic devices based on $Cs_2AgBiBr_6$ have experimentally achieved a PCE of 3.11% [139], which is around 40% of the ideal SLME predict by our calculations, while Ag_3BiI_6 devices achieved a PCE of 5.6%, which is around just 26% of the ideal SLME. Hence, there is room for experimental improvement of device performances. By comparing the experimental curve measured by Turkevich *et al.* [30] shown in Figure 3.10(c), we see that the J_{sc} is at 60% of the ideal SLME value, while the V_{oc} is at 43%. The low V_{oc} can have several origins, such as

choosing unfitted electron or hole transport layers. The SLME results indicate that a possible direction for improving PCEs of Ag/Bi double salt devices is the optimization of the applied electron/hole transport layers and their interfaces or the passivation of defects, as both could be sources for the low V_{oc}. In a recent work published by Guerrero *et al.*, the authors were able to improve the V_{oc} for Ag-rich double salts, in alignment with our predictions [140].

Take-home Messages

- Ag/Bi double salts are challenging materials to model via ab-initio calculations. Their structural, electronic, and optical properties are sensitive to the different structural models. As so, a method that can appropriately describe the atomic positions of Ag, Bi, and vacancies in the crystal lattice is necessary.
- These materials cannot be modeled as random alloys.
- We develop a symmetry-based modeling approach based on WPS that allows us to retain a large part of the experimentally reported symmetries. These structures are unique for each compound in the Ag/Bi double salt class of materials and can correctly capture structural and electronic properties in excellent agreement with the available experimental data.
- These materials exhibit small and tunable band-gaps, effective masses, large absorption coefficients, and efficiencies, which makes them interesting candidates for photovoltaic applications.
- Current devices based on Ag/Bi double salts are mainly limited by low V_{oc}. Optimizing electron/hole transport layers and their interfaces or the passivating defects could significantly improve solar-cell performances.

This work has been published and featured on the front cover of *Solar RRL*. The article can be found at reference [131].

CHAPTER 4

VACANCY-ORDERED HALIDE DOUBLE PEROVSKITES

In this chapter, I will discuss a class of perovskites known as vacancy-ordered halide double perovskites (VODP). These, as the Ag/Bi double salts, have been proposed as potential lead-free materials for photovoltaic applications. Yet, poor device performance still challenges their applications as solar-cell absorbers. To gain insights, we will explore their structural, electronic, and optical properties by means of DFT, GW, and Bethe-Salpeter calculations. The first half of this section will focus on Ti-based and Zr-based perovskites, as these have been thoroughly investigated experimentally in recent years. I will use this section to present the general structural, stability, electronic, and optical properties of VODP. In the second half of this chapter, I will generalize these properties for the entire VODP class and classify them according to their electronic configuration. Finally, I will explore the role of excitons in these compounds and provide a deep understanding of the origin of low solar-cell device performance observed in VODP. The main objective is to identify prospective materials for both photovoltaics and LED applications.

A_2MX_6 VODP are a class of perovskites that have emerged as potential lead-free materials for a broad range of applications, such as solar-cells [29, 141] and light-emitting devices [142, 143]. These materials can be seen as double perovskites ($A_2^{+1}M^{+1}M'^{+3}X_6^{-1}$) where one of the metal sites is empty. Therefore, to retain charge neutrality in the vacancy-ordered structure the M-site atom is tetravalent, that is $A_2^{+1}M^{+4}X_6^{-1}$. These materials are very stable, and to-date several VODPs were synthesized containing different tetravalent M-site atoms such as Te [144], Ti [141], Zr [142], Hf [74], Pd [145], Pt [146], Se [147], Sb [148], Sn [29] and Ge [149]. In fact, the oxidation of Sn^{2+} in its tetravalent state Sn^{4+} leads to the structural transformation of $CsSnX_3$ to the more stable Cs_2SnX_6 VODP [29]. Throughout the past couple of years, there has been a growing interest in these materials as they could be potential candidates for lead-free perovskite photovoltaics. Sn-based VODP were the first ones to be employed in solar-cell devices, achieving PCE of up to 0.96%, V_{oc} of 0.51 V and also J_{sc} of 5.41 $mAcm^{-2}$ [150]. Similarly, Ti-based compounds Cs_2TiX_6 (X = Br, I) have also been successfully incorporated in solar-cell devices achieving PCE of up to 3.3% in a heterojunction architecture with C_{60}, with a V_{oc} of 1.0 V and a J_{sc} of 5.69 $mAcm^2$ [141]. Although these numbers are high compared to other VODPs; these exhibit poor photovoltaic performance compared to their Pb-based counterparts. To understand the limiting factors behind their performance I will investigate the structural, electronic, and optical properties of the VODP class. We start our discussion from the known materials Cs_2TiX_6 (X=Br, I), and also Cs_2ZrBr_6 (X=Br, I), as these alongside with Sn-based VODP, have been the primary materials being investigated for photovoltaics [151–153].

4.1 Structural Properties

VODPs typically crystallize in the $Fm\bar{3}m$ face-centred cubic lattice (space-group number 225). The lattice is made of rock-salt arrangement of corner-sharing MX_6 and ΔX_6 octahedra, where Δ represents a vacant site, as schematically despicted in Figure 4.1. Furthermore, Ti and Zr exhibit similar electronic configurations which should lead to similarities in their electronic and optical properties, as the M-site is one of the main contributors to the perovskite optoelectronic properties [24]. The first step in our investigation is to employ DFT to optimize lattice parameters and atomic positions fully. For this purpose, we use the Quantum ESPRESSO package [154, 155] with PBE pseudopotentials taken from Pseudo Dojo [156]. The computational details are included in the Appendix A.2. Similarly to ABX_3 perovskites, bromides have smaller lattice constants compared to iodides. The calculated lattice parameters for Cs_2TiBr_6 and Cs_2ZrBr_6 are 10.92 Å and 11.24 Å, respectively. For the iodides Cs_2TiI_6 and Cs_2ZrI_6, we

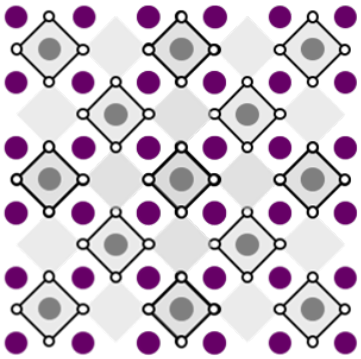

Figure 4.1 – Representation of the conventional cell of A_2MX_6 VODP structures.

obtain larger lattice constants of 11.75 Å and 12.00 Å. These are in good agreement with the experimental values of 10.57-10.92 Å for Cs_2TiBr_6 [151–153] and 11.67 Å for Cs_2TiI_6 [151]. We can also quantify the volume of the vacant site and find 36.9 $Å^3$, 33.1 $Å^3$, 38.5 $Å^3$, and 40.2 $Å^3$ for Cs_2TiBr_6, Cs_2ZrBr_6, Cs_2TiI_6, and Cs_2ZrI_6, respectively. This is consistent with the fact that only halogens surround the vacant site. Hence their interactions define its size.

4.2 Electronic Structure of the Ti- and Zr-based VODP

We move to investigate the electronic properties of the materials. For this purpose, we employ different approximations for the exchange-correlation function within DFT to probe and understand the role of the different corrections in these materials. These approaches are the standard DFT-PBE and hybrid functional DFT-HSE06 [87]. Figure 4.2 show the electronic band structure of Cs_2TiBr_6 and Cs_2ZrI_6 with and without spin–orbit coupling (SOC). A complete symmetry analysis of the bands for the different high symmetry points of the Brillouin zone is also shown. The electronic band structure of these materials is very similar, which can be explained by the orbital contribution to the bands. As seen on the projected density of states of Figure 4.2, the VBM is dominated by halogen's p-orbitals while the CBM is mainly formed by M-site d-orbitals. Both materials exhibit indirect band-gaps between the Γ-X high symmetry points. Within DFT-HSE06 we obtain band-gaps of 2.68 eV and 2.58 eV for Cs_2TiBr_6 and Cs_2ZrI_6, respectively. Furthermore, smaller halogens exhibit larger band-gaps, while the smaller the B-site atom, the smaller the band-gap. We note that within DFT-PBE, Cs_2TiBr_6 has a smaller band-gap than Cs_2ZrI_6 due to the larger exchange correction for bromides concerning iodides obtained with the hybrid HSE06 approach. A summary of the band-gaps for all materials can be found in Table 4.1.

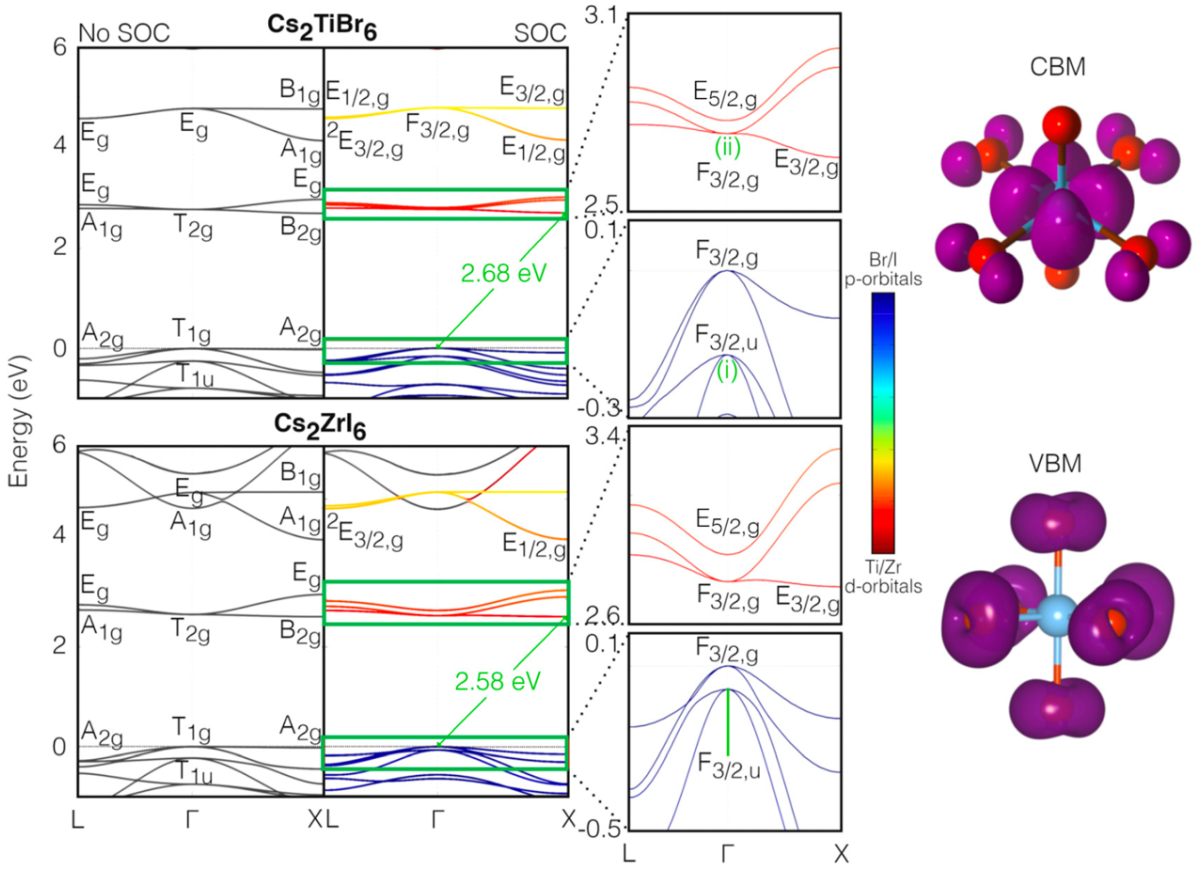

Figure 4.2 – Electronic band structures and symmetry analysis with and without SOC for Cs_2TiBr_6 and Cs_2ZrI_6. The VBM is set to zero, and the conduction bands are rigidly shifted to match the DFT-HSE06 results. The colors on SOC band structures denote the projection of the halogen p-orbitals (blue) and M-site atoms d-orbitals (red) to the respective band. The pseudo-charge density for the VBM and the CBM of Cs2TiBr$_6$ is also shown. Figure adapted from reference [157].

Table 4.1 – Calculated electronic band-gaps E_g (in eV) for DFT-PBE, DFT-HSE and G_oW_o, and measured optical gaps.

	DFT-PBE		DFT-HSE		G_oW_o		Experimental
	Indirect	Direct	Indirect	Direct	Indirect	Direct	Optical Band-gap
Cs_2TiBr_6	1.57	1.64	2.68	2.74	3.87	3.93	1.78-2.00 [141, 151]
Cs_2TiI_6	0.74	0.79	1.75	1.80	2.31	2.33	1.02 [151]
Cs_2ZrBr_6	2.73	2.75	3.88	3.90	5.02	5.04	3.76 [142]
Cs_2ZrI_6	1.65	1.67	2.58	2.59	3.32	3.34	Not reported

We perform G_0W_0 calculations (See methods in Chapter 2.2) to improve the band-gap description. For Cs_2TiBr_6, we predict a quasi-particle band-gap of 3.87 eV, around two times larger than the experimentally measured optical band-gap of 1.78-2.00 eV [141, 151, 152] and also larger than our HSE06 calculation. To investigate the origin of the large GW band-gap in Figure 4.3 we compare the band structure of Cs_2TiI_6 at both HSE and GW levels. By aligning the VBM which is made of I p-states, we show that both approaches offer a similar description of the VBM and the dispersive Cs-s states at the conduction band. Yet, we observe a discrepancy in the description of the Ti-d and Zr-d states at the CBM. We attribute these difference to the starting point of our GW calculation, which does not correctly describes the correlated d-states of the M^{4+}-site. One possible solution is to employ Hubbard corrections via DFT+U as a starting point for the GW calculations. A self-consistent DFT+U-GW method has already been proposed by Patrick and Giustino and was shown to provide reliable results for TiO_2.

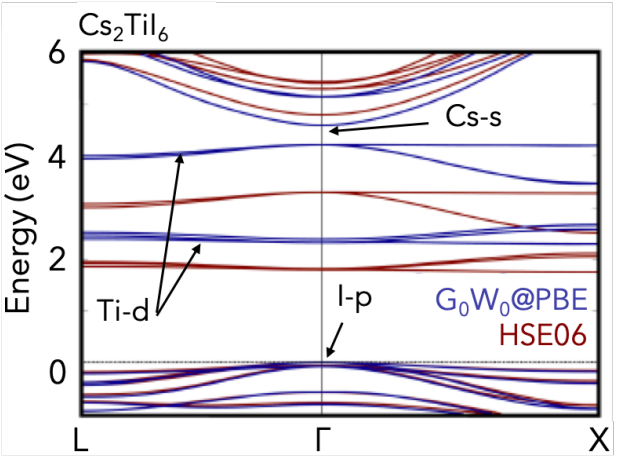

Figure 4.3 – Superposed HSE and GW interpolated band structure for Cs_2TiI_6 materials.

4.3 Crystal Field Splitting of d-orbitals in VODPs

Here, we analyze in-depth the orbital contribution to the band edges. The CBM of the VODP arises from the interaction between the d_{xy} orbitals of the M-site atoms and the p-orbitals of the halogens. As shown in Figure 4.4, the d-orbitals split when subjected to octahedral coordination resulting in a double degenerate e_g state ($d_{x^2-y^2}$ and d_{z^2}) and a triple degenerate t_{2g} state (d_{xy}, d_{xz}, and d_{yz}), similar to what is observed at the Γ point in the band structures without SOC. The charge density plots of these points demonstrate a combination of the aforementioned

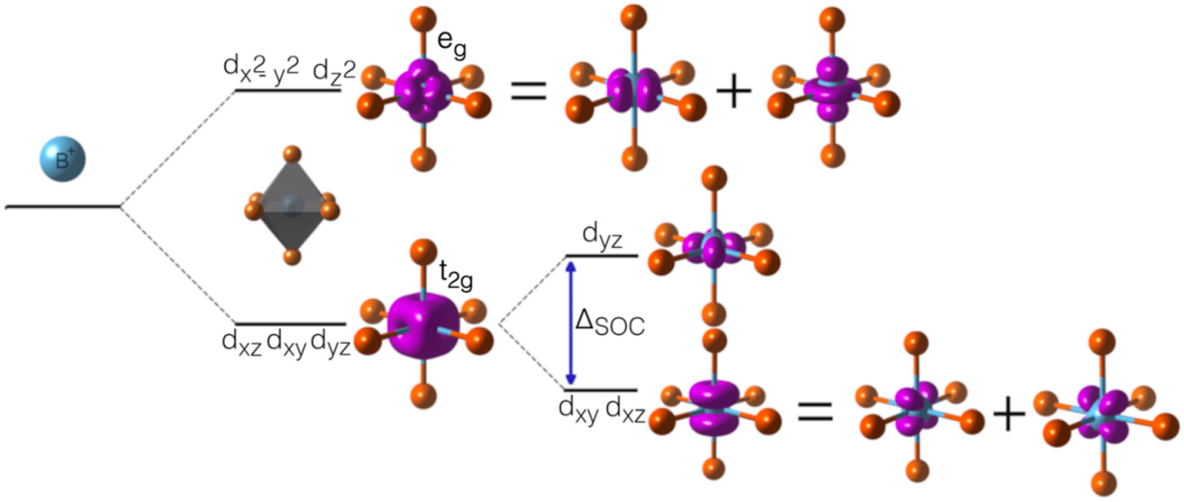

Figure 4.4 – Splitting of Ti/Zr d-states due to octahedral coordination and Δ_{SOC} split. Figure adapted from reference [157].

states, consistent with the pseudo-charge density plots of Cs_2TiBr_6 and Cs_2ZrI_6. Including SOC interactions affects the conduction band, causing a second splitting of the t_{2g} states at the CBM at the Γ point, as can be seen in Figure 4.2. We observe splittings of 22 and 85 meV for Cs_2TiBr_6 and Cs_2ZrI_6, respectively, within DFT-HSE. The value of Δ_{SOC} increases when going from Ti to Zr, which is consistent with the positioning of the atomic reference levels for the d-orbitals of Ti and Zr. The VBM of all compounds is comprised exclusively of p-orbitals of the halogens, which are arranged around the vacant site as shown in Figure 4.5(a). This corroborates the previous idea, where the interaction between the halogens dictates the size of the vacant site.

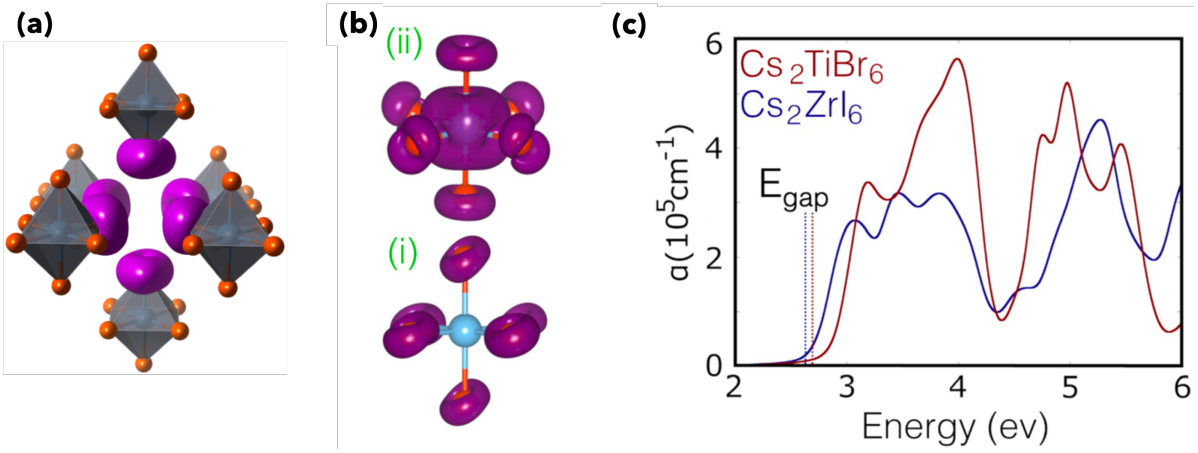

Figure 4.5 – (a) The charge density on the VBM is shown to be p-orbitals of halide surrounding the vacant site. (b) Pseudo-charge density for the first symmetry allowed transition between points (i) to (ii) as shown in Fig. 4.2. (c) Calculated absorption coefficient with DFT-HSE band-gap illustrated with dotted lines. Figure adapted from reference [157].

4.4 Optical Properties: Independent Particle Approach

In the following, we investigate these compounds' optical properties. The lowest direct transition shown in the band structures of Figure 4.2 is parity forbidden at the Γ and X points. We find that the first parity allowed transition is given by the irreducible representations $F_{3/2,u}$ and $F_{3/2,g}$ at the VBM and CBM, respectively. These transitions are 161 and 67 meV below the VBM of Cs_2TiBr_6 and Cs_2ZrI_6 and the correspondent charge density is show in Figure 4.5(b). The inclusion of SOC is shown to be important due to both band splittings and energy level shifts. Figure 4.5(c) shows the calculated absorption coefficient obtained within DFT-PBE. The plot is shifted to match the HSE06 band-gap. Here one can observe a small shift at the onset of the spectra concerning the position of the DFT-HSE06 band-gap (dotted lines in Figure 4.5(c)), which is consistent with the symmetry forbidden direct transition at Γ.

To investigate the potential transport properties of these compounds, we evaluate the charge carriers' effective masses at the band edges, summarized in Table 4.2. At the VBM, all materials exhibit heavy and light holes at the Γ point. The iodine-based materials exhibit lower effective masses, while the hole masses are practically the same between bromides and iodides. In the conduction band, the Zr-based compounds exhibit lower effective masses for electrons. Therefore, halogens affect electron and hole masses, whereas the M-site atoms only impact the electron mass. Due to the cubic lattice structure of our systems, the in-plane expansion of the charge density is threefold degenerate along symmetry-equivalent planes. However, minor oc-

tahedra distortions that break the crystal symmetry could potentially confine the fast carriers to a two-dimensional plane [158].

Table 4.2 – Charge carrier effective masses in units of electron mass m_0. The masses are isotropic for the holes (m_h) at the valence band top, and we include the heavy and light bands. For electrons (m_e) at the conduction band bottom, there are two components in the effective mass tensor, a fast and a slow direction.

Effective masses (m_0)	m_h^{light}	m_h^{heavy}	m_e^{fast}	m_e^{slow}
Cs_2TiBr_6	1.14	2.84	1.76	7.62
Cs_2TiI_6	0.62	1.55	0.98	8.91
Cs_2ZrBr_6	1.12	2.82	1.27	11.29
Cs_2ZrI_6	0.60	1.45	0.86	11.55

4.5 Chemical and Mechanical Stability

Finally, we move to investigate the mechanical and chemical stability of the materials. To gain insights into the formation of the materials during synthesis and make comparisons within the VODP class, we examine their stability in various possible decomposition reaction pathways. We follow the procedure introduced by Persson *et al.* [159] by imposing that the atomic chemical potential μ_i of atom i must be smaller or equal to its solid phase μ_i^{solid} to assure that there is no precipitation of these, that is $\mu_i \leq \mu_i^{solid} \Rightarrow \Delta\mu_i \leq 0$. Here, when $\mu_i = \mu_i^{solid}$ we obtain the atom i-rich limit of the stability diagram.

$$m\Delta\mu_{Cs} + n\Delta\mu_M + l\Delta\mu_X \leq \Delta H(Cs_mM_nX_l) \tag{4.1}$$

Next, we take into account the stability condition of the Cs_2MX_6 VODP via the relation $2\Delta\mu_{Cs} + \Delta\mu_M + 6\Delta\mu_X = \Delta H(Cs_2MX_6)$, where M=Ti, Zr, X=Br, I and $\Delta H(Cs_2MX_6)$ is the heat of formation of the compound. We derive similar relations to all the possible competing phases during synthesis. That means that one should impose that the sum of the chemical potentials of constituent atoms of each compound should be less than their respective heat of formation. This allows us to draw the extreme limits where all the competing phases will not form, but the VODP in the analysis will. We use the Materials Project database [160] to identify these compounds and derive the set of inequalities given by Equation 4.1.

The obtained decomposition pathway diagrams for Cs_2TiBr_6 and Cs_2ZrI_6 are shown in Figure 4.6(a). We find that all binary compounds that do not contain Cs are stable within the Cs-poor region, while compounds containing Cs are in the B-poor region, which shows the consistency of the diagrams. The grey-shaded region in these diagrams reveals the region where the Cs_2MX_6 compound can form, but all other competing phases can not. Since this region is located approximately in the middle of the diagram, we expect these VODP materials to be more easily synthesized in a chemically balanced environment. The materials Cs_2TiI_6 and Cs_2ZrBr_6 are also shown to be stable as they exhibit the same features. The stability plots for the last two compounds and all inequalities can be found in Appendix B. A comparison of the grey region sizes between all compounds shows that Zr-based VODPs are expected to be more stable against decomposition than Ti-based ones. Furthermore, iodine-based compounds should be less stable than bromides. We also investigate the mechanical stability of each compound by employing

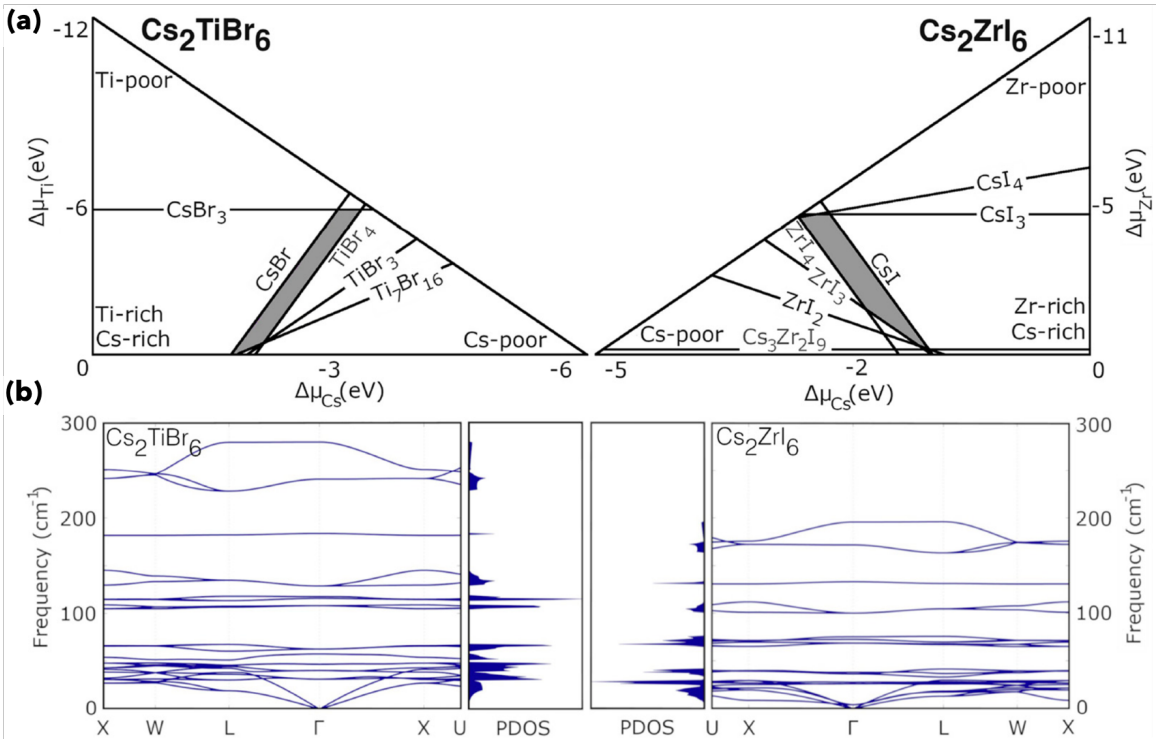

Figure 4.6 – (a) Decomposition pathway diagrams for Cs_2TiBr_6 and Cs_2ZrI_6 with stability region shown as the gray shaded area. (b) Phonon dispersion and density of states. The absence of imaginary (or soft) modes indicates dynamical stability. Figure adapted from reference [157].

DFPT (See Chapter 2.4) to compute the phonon dispersions. The absence of modes with imaginary frequencies confirms the mechanical stability of these materials, as shown in Figure 4.6

and Appendix B. Moreover, we observe a redshift of the phonon modes between different compounds, corresponding to the increasing mass of compounds from the lighter Ti-based bromide to the heavier Zr-based iodide. Both chemical and dynamical stability investigations support that all compounds discussed in this section should be stable. This is particularly important for the proposed prototypical Cs_2ZrI_6, which synthesis was reported only once in the literature in the early 1980s [161]. Yet, it exhibits good stability, the lowest charge carrier effective masses, and relatively small band-gaps.

4.6 Closed-Shell Families of VODPs

The confined nature of the VODP octahedra and low-dispersive electronic bands motivated us to perform a deep investigation of the electron-hole coupling, which could be of potential interest for light-emitting applications, optically controlled information processing, and fast/slow light applications [103].

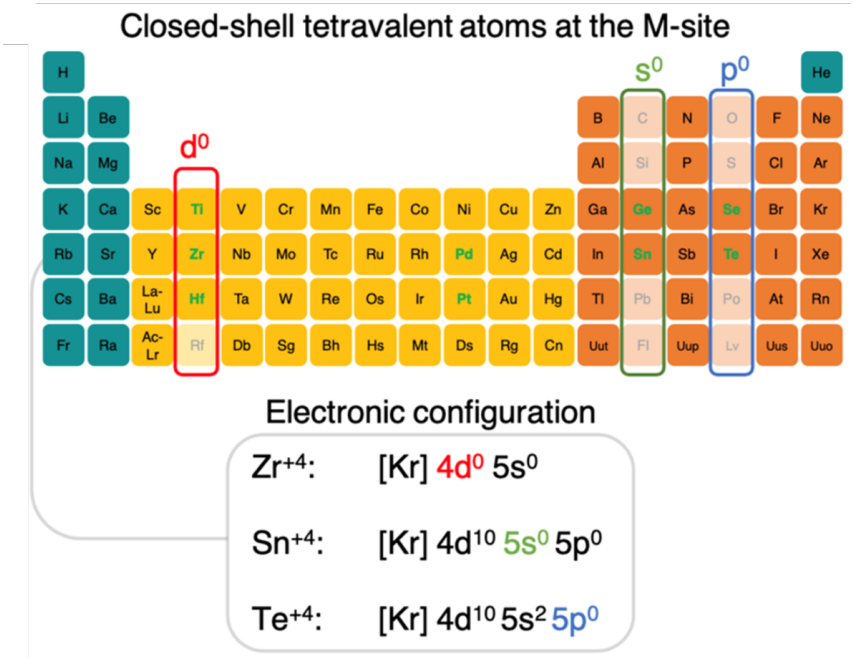

Figure 4.7 – In green summary of the M^{4+} tetravalent atoms successfully synthesized in a VODP material. The boxes marks the s^0, p^0, and d^0 closed-shell atoms for a +4 oxidation state. The general electronic configuration is also shown. Figure adapted from reference [162].

When it comes to electron-hole coupling and excitonic processes in VODP, one can find

several discussions in the literature that associate their tunable and broad photoluminescence to the formation of exciton [72, 74, 143, 163]. Yet, to date, a detailed theoretical description of excitons in VODP is still missing. To investigate these effects, we first generalize the analysis we did for Ti-based and Zr-based VODPs and expand to study the entire class of materials exhibiting closed shells. In Figure 4.7, we illustrate the columns of the periodic table on which atoms exhibit s-, p-, or d-closed shells at a +4 oxidation state. The atoms highlighted in green have already been incorporated into VODP materials. We choose to classify the VODPs according to the electronic configuration of the M-site metal. The reason for this choice is due to the fact that while halogen p-orbitals participate actively at both the VBM and CBM of all VODPs, the M-site orbital will primarily dictate the properties of the CBM. This means that one can expect VODP with different M-site metals that exhibit the same electronic configuration to have similar electronic and optical properties. Thus, identifying the closed-shell families of VODP will allow us to cover several materials with just a few representative compounds. We select period five of the periodic table, thus Sn, Te, and Zr as the atomic species at the M-site to represent each closed-shell VODP type, as all these materials have already been synthesized. This generates six different materials: Cs_2TeX_6, Cs_2SnX_6, and Cs_2ZrX_6 (with X = Br, I). Interestingly, Te^{4+} is isoelectronic with Pb^{2+}, the building block of the most efficient perovskite materials for optoelectronic applications.

Table 4.3 – Optimized structural parameters within DFT-PBE. Here, a and a_{exp} are the theoretical and experimental lattice parameters, respectively, d_{M-X} is the bond length between the metal site and halogen, and V_{vac} is the volume of the vacant site. (M is the metal site, Δ the vacancy site, and X the halogens).

M-site valency	s^0		p^0		d^0	
	Cs_2SnBr_6	Cs_2SnI_6	Cs_2TeBr_6	Cs_2TeI_6	Cs_2ZrBr_6	Cs_2ZrI_6
a (Å)	11.14	12.02	11.32	12.08	11.24	12.00
a_{exp} (Å)	10.86[164]	11.62[29]	10.91[165]	11.70[144]	11.16[142]	11.66[161]
d_{M-X} (Å)	2.65	2.91	2.74	2.98	2.65	2.88
V_{vac} (Å^3)	33.2	38.3	34.9	40.4	33.1	40.2

As a starting point, we fully optimize the atomic coordinates and lattice parameters for all materials within DFT-PBE. Table 4.3 summarizes the optimized lattice parameters, metal-halogen bond lengths, and volumetric size of the vacant site. The structures for all compounds are in the $Fm\bar{3}m$ space-group, except Cs_2SnI_6 which exhibits slightly rotated Sn-I octahedra

and minor octahedra distortions, in agreement with the work of Jong *et al* [166]. Earlier in this section, we show that halogen-halogen p-orbital interactions dictate the size of the vacant site for Ti- and Zr-based VODP. Here we observe the same for all VODPs regardless of the atom at the M-site. Hence, Br-to-I substitution can be used as a tuning parameter to control the size of the vacant site from 33 to 40 $Å^3$, and Cl-based VODPs would be expected to exhibit even smaller vacant sites. To also address the mechanical stability of these compounds, we perform phonon calculations within DFPT, as shown in Figure 4.8. As presented in the first half of this section, the absence of phonon imaginary modes for all studied compounds indicates mechanical stability. We also observe a redshift of the phonon dispersions when going from Br- to I-based compounds, which is consistent with the increase of the atomic mass of halogens and thus damping the M-X oscillation modes.

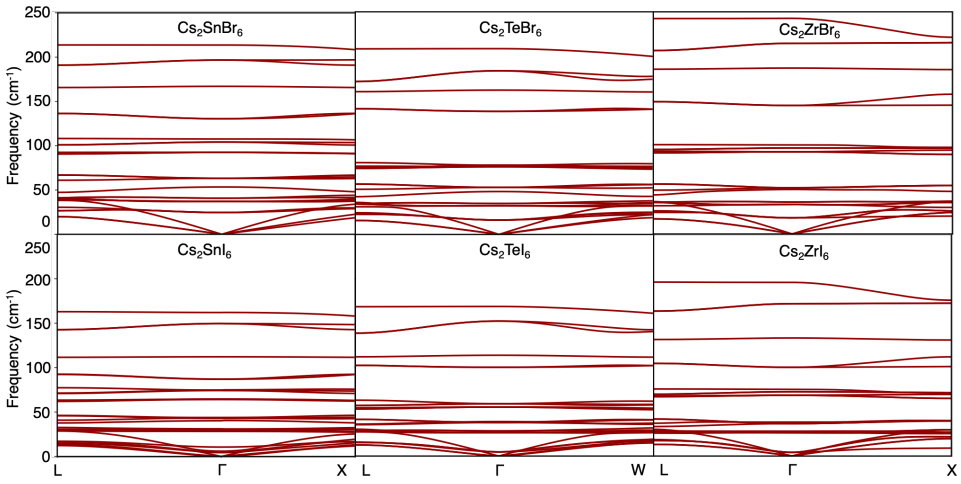

Figure 4.8 – Phonon dispersions of the optimized structures. The absence of imaginary modes confirms mechanical stability. Figure adapted from reference [162].

4.7 Electronic Structure of Closed-Shell VODPs

To accurately evaluate excitonic properties, it is essential to have a good description of the electronic band-gaps and charge carrier effective masses, as both properties will strongly impact the predicted exciton binding energies and relative peak positions. To this goal, we employ G_0W_0 calculations to take into the quasi-particle effects due to screened electron-electron interactions as previously discussed.

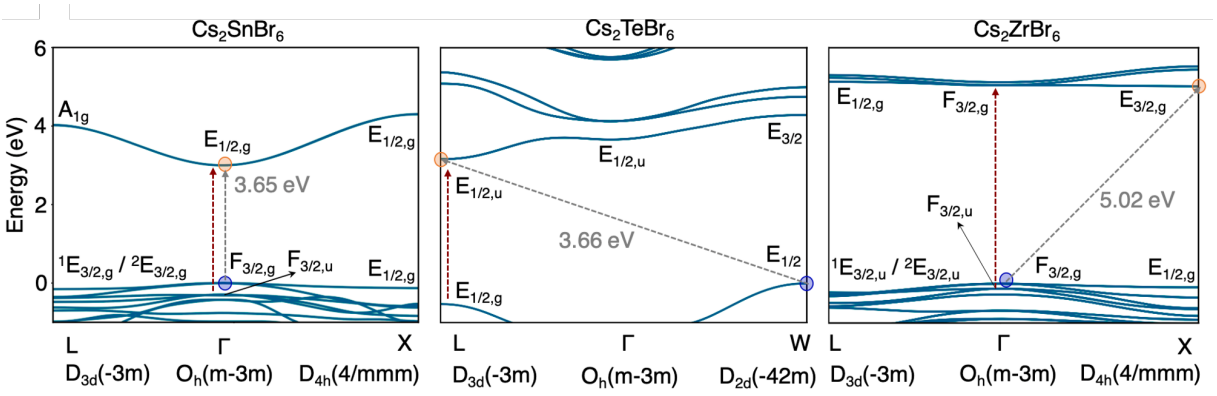

Figure 4.9 – G_0W_0 electronic band structures and charge densities for Br-based materials. The irreducible representations and point group symmetries are shown, as well as the VBM and CBM, marked with blue and orange circles, respectively. The grey and red arrows indicate the fundamental band-gap and first direct allowed transition, respectively. Figure adapted from reference [162].

Figure 4.9 shows the electronic band structures for the Br-based compounds, while the results for I-based materials are illustrated in Figure 4.10. Sn-based compounds exhibit direct band-gaps at the Γ point. By performing a symmetry analysis of the electronic band structures we identify that the transition from the VBM to the CBM is given by a transition from the irreducible representation $F_{3/2,g}$ to $E_{1/2,g}$, which is in-fact parity forbidden. Instead, we identify the first direct dipole-allowed transition for the Sn-based compounds as a transition from the VBM-1 ($F_{3/2,u}$) to CBM ($E_{1/2,g}$), that is, 300 and 350 meV larger than the fundamental band-gaps of Cs_2SnBr_6 and Cs_2SnI_6, respectively. Due to the different orbitals involved at the band edges,

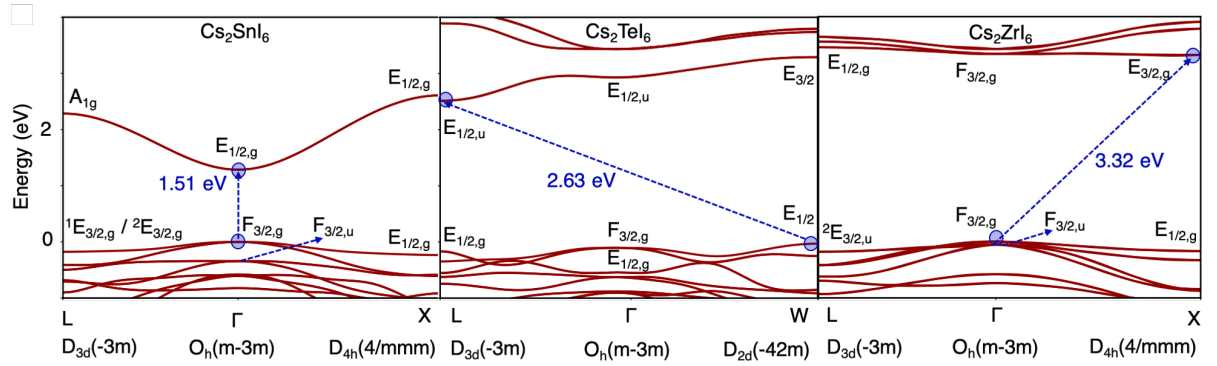

Figure 4.10 – G_0W_0 electronic band structures and charge densities for I-based materials. Figure adapted from reference [162].

the band-gaps are indirect between the *L* and *W* high-symmetry points for the Te-based com-

pounds. Based on our symmetry analysis, we identify the first allowed transition as being from the VBM ($E_{1/2,g}$) to the CBM ($E_{1/2,u}$) at L for Cs_2TeX_6. Within G_0W_0 these transitions are of 2.83 and 3.90 eV for Cs_2TeI_6 and Cs_2TeBr_6, respectively. For the Zr-based compounds, the first allowed transition is identified to be from the VBM-1 ($F_{3/2,u}$) to CBM ($F_{3/2,g}$). Within G_0W_0, these transitions are of 5.18 and 3.64 eV for Cs_2ZrBr_6 and Cs_2ZrI_6, respectively. Table 4.4 gathers a summary of the obtained DFT-PBE and G_0W_0 band-gaps.

Table 4.4 – Summary of the predicted electronic band-gaps within DFT-PBE and G_0W_0.

	Cs_2SnBr_6	Cs_2SnI_6	Cs_2TeBr_6	Cs_2TeI_6	Cs_2ZrBr_6	Cs_2ZrI_6
DFT (eV)	1.30	0.17	2.04	1.16	2.73	1.65
G_0W_0 (eV)	3.65	1.51	3.66	2.63	5.02	3.32

As shown in Figure 4.11, the VBM of Sn- and Zr-based compounds is composed solely of halogen's p-orbitals, which is not the case of Te-based materials where these are hybridized with Te s-orbitals forming a VBM which resembles Pb-based halide perovskites. This is potentially interesting for hole transport, as only Te-based compounds have a uniform charge density that expands in three dimensions. The CBM of Sn-based materials is formed by a hybridization of Sn s-orbitals and halogen's p-orbitals, which resembles the VBM of Te-based materials. This similarity makes Sn-based materials potentially interesting for electron transport. For Zr-based

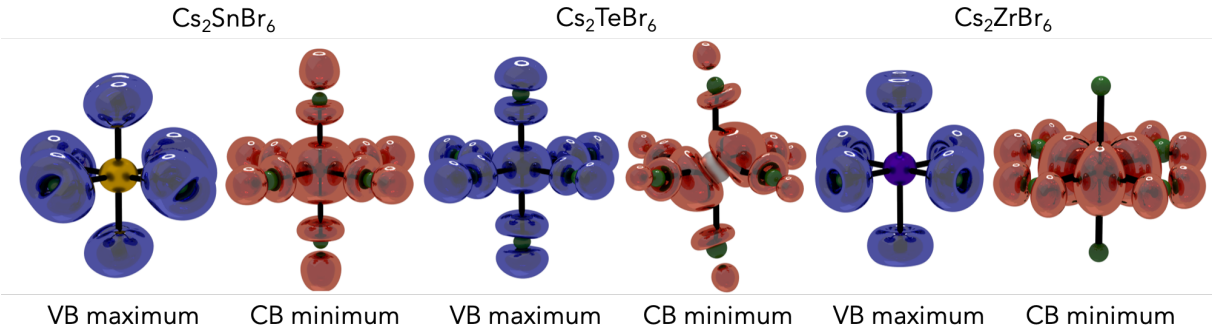

Figure 4.11 – Electronic charge densities are evaluated at the VBM and CBM of Cs_2MBr_6 (M = Sn, Te, Zr). Figure adapted from reference [162].

materials, we find contributions of Zr d- and halogen's p-orbitals, while for Te-based compounds, we see contributions of p-orbitals of both Te and halogens. This analysis confirms that the electronic contributions of the M-site metals are indeed in agreement with their electronic

valency, as we first categorize as the s^0, p^0 and d^0 families in Figure 4.7. That is, the empty s^0 of Sn, p^0 of Te and d^0 of Zr have a primary role at the conduction band edges.

Next, we evaluate the charge carrier effective masses at the band-edges within the G_0W_0 level. Sn-based materials exhibit light and isotropic electron effective masses as well as Te-based hole effective masses due to the s-orbital character involved in their electronic structure. Which further sustains the potential application of Sn-based materials for electron transport and Te-based for hole transport. Zr-based materials exhibit large effective masses for both electrons and holes, which would challenge their performance as transport layers. A summary of the average of the effective masses tensor can be found in Table 4.5.

Table 4.5 – Average electron (m_e) and hole (m_h) effective masses at the band edges within G_0W_0. Subscript *l* and *h* refer to light and heavy bands' effective masses.

Effective masses(m_0)	Cs_2SnBr_6	Cs_2SnI_6	Cs_2TeBr_6	Cs_2TeI_6	Cs_2ZrBr_6	Cs_2ZrI_6
m_e	0.24	0.29	0.33	0.39	1.80	1.24
m_h^l	0.55	0.58	0.46	0.29	1.12	0.60
m_h^h	1.22	1.08	-	-	2.82	1.45

4.8 Optical Properties: Bethe-Salpeter Equation

Having established the general electronic structure, we now move to the investigation of their optical properties including electron-hole interactions. For this purpose, we employ the ab-initio Bethe-Salpeter formalism (See methods in Chapter 2.3), which accounts for the electron-hole interactions that give rise to excitons. Figure 4.12 shows the calculated absorption coefficients for all materials within BSE@G_0W_0 and IP@G_0W_0 (without electron-hole coupling). We observe a strong modification of the IP spectra in comparison to the calculation including excitonic effects. This can be understood by the quasi-isolated nature of the octahedra in VODP, which induces confinement effects. The inclusion of electron-hole coupling leads to a red-shift of all the BSE spectra, and the oscillator strengths are redistributed compared to the IP calculation. We find bright exciton states within the band-gap and dark states (not optically active) at lower energies for all materials. We look at the optical band-gaps to further analyze the optical spectra. Figure 4.13(a) shows the first allowed transitions (optical band-gap) with and without electron-hole interactions and the experimental data. We find an excellent agreement between

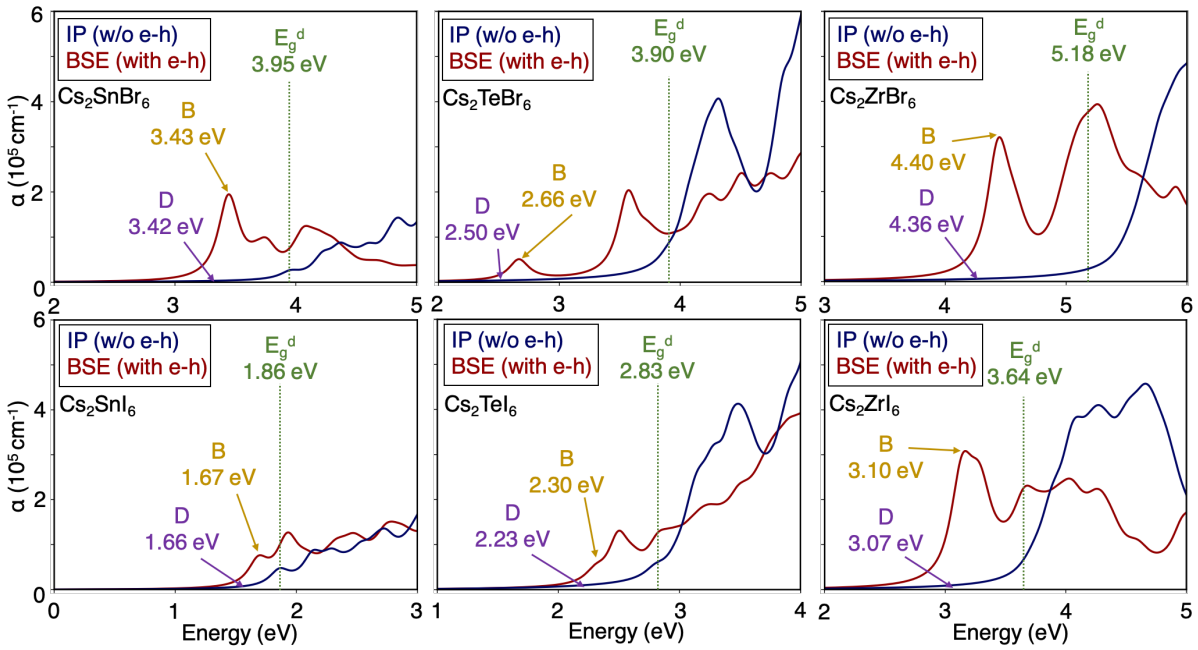

Figure 4.12 – Optical absorption coefficients of the Cs_2MX_6 (M = Sn, Te, Zr, and X = Br, I) vacancy-ordered halide double perovskites within the BSE@G_0W_0 and IP@G_0W_0. The red and blue curves show the coefficients of BSE (with electron-hole interactions) and IP (without electron-hole interactions). The positions of the dark (D) and bright (B) exciton states are shown. The green dotted lines show the position of the first direct dipole-allowed transition, E_g^d, at the G_0W_0 level. Figure adapted from reference [162].

the BSE values and the available measurements, which we extract by picking the first excitonic peak in the experimental absorption of references [142, 165, 167, 168].

We define the exciton binding energy E_b as the energy difference between the BSE bright exciton peak and the first allowed transition. As shown in Figure 4.13(b), we find large exciton binding energies ranging from 190 to 540 meV for iodine- and 510 to 1240 meV for bromine-based compounds. These values are quite large, as can be expected from the quasi-isolated nature of the VODP octahedra. The exciton binding energies are larger for bromide compounds than for the iodide counterparts. This is related to the connection between these materials' electronic band-gap and dielectric constant, as the electron polarizability decreases as the band-gap increases. This means that screening the Coulomb interactions between electrons and holes becomes less efficient, leading to more tightly bounded excitonic states [169]. This is consistent with the available literature for excitons in AMX_3 halide perovskites [169, 170] and also $A_2MM'X_6$ double perovskites [171]. Te-based materials exhibit very large exciton binding energies. This is surprising as they share common optical features to Pb-based halide perovskites,

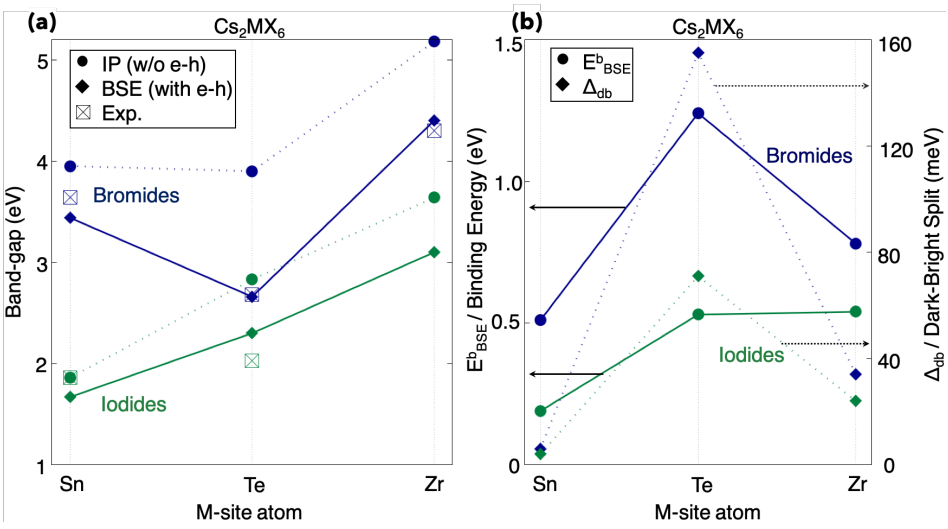

Figure 4.13 – (a) Comparison between the first allowed transition at the G0W$_0$ level, the first bright peak of BSE calculation, and experimentally measured optical band-gaps. (b) Exciton binding energy E_b and dark-bright splitting Δ_{db} obtained from the BSE calculations. Blue and green curves represent bromides and iodides, respectively. Figure adapted from reference [162].

i.e. strong optical transitions that involve s (active lone-pair) to p orbitals of the respective M-site atoms. Yet, Pb-based halide perovskites exhibit low exciton binding energy [169, 172]. We attribute the strong electron-hole interactions observed in the case of the Te-based materials to their intrinsic structural confinement and their indirect band-gap electronic structure, which give rise to Frenkel-like excitons. Hence, despite the similar electronic configuration, Te-based VODPs are far from considered reasonable alternatives to Pb-based halide perovskites.

The calculated wavefunctions for the first bright excitons are shown in Figure 4.14(a) as a spatial distribution given by $|\Psi(r_h, r_e)|^2$, where r_h and r_e are the hole and electron positions, respectively. The exciton wavefunction is more localized for Te-based materials, while Sn-based materials exhibit significantly delocalized wavefunctions that extend over several unit cells of the lattice. Moreover, the wavefunction associated with I-based materials is more delocalized than Br-based ones, in agreement with the calculated exciton binding energies. The exciton in Cs_2SnI_6 is closer to a Wannier-type (spatially delocalized exciton), which is also confirmed by its binding energy, which is sizeably smaller than for the other compounds. On the other hand, Cs_2TeX_6 and Cs_2ZrX_6 compounds are closer to a Frenkel-type description (spatially localized excitons). Over the series of closed-shell VODP, we observe an interplay between Wannier- and Frenkel-type excitons that are closely related to the atomic orbital at the M-site, as a clear example of a Wannier-like exciton is formed for Cs_2SnI_6 and a Frenkel-type for Cs_2TeBr_6. The

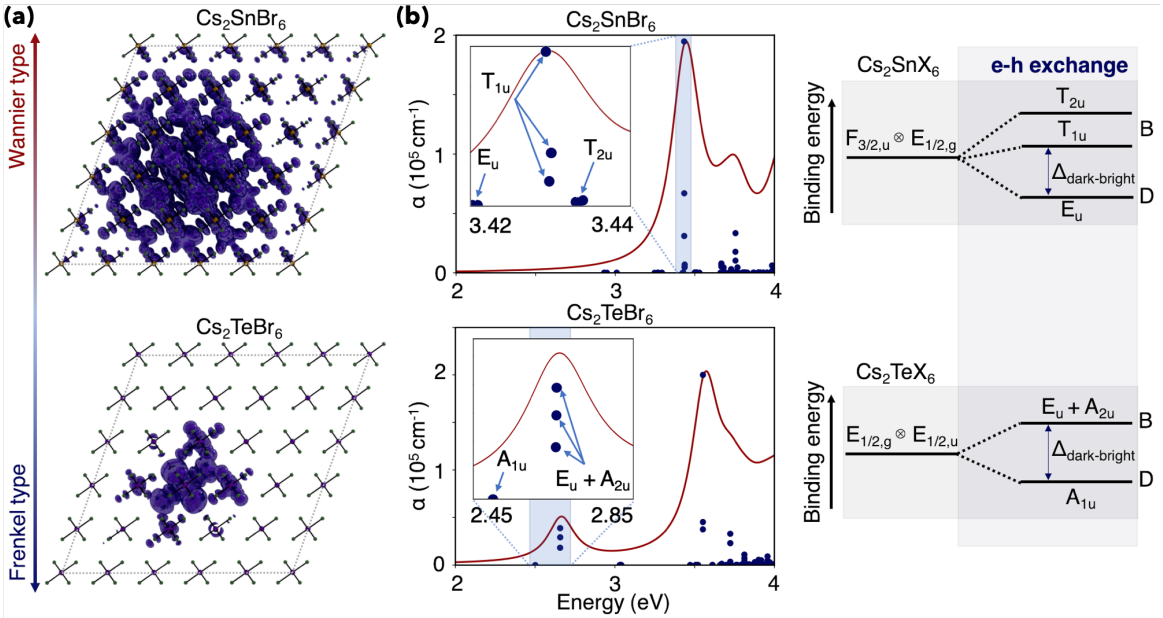

Figure 4.14 – (a) Exciton spatial distribution $|\Psi(r_h, r_e)|^2$ for the bright exciton. The hole position r_h is fixed near the halogen atoms. The isovalue for the volumetric plot is chosen to represent 85% of the total wavefunction distribution. (b) Calculated exciton oscillator strengths, with fine structure, shown as an inset plot. On the right an illustration of the dark-bright splitting. Figure adapted from reference [162].

wavefunction for the other compounds can be found in Figure 4.15.

This crossover can also be understood from the projection of the exciton weights $|A^{\lambda}_{eh}|$ over the band-structures shown in Figure 4.16, where $|\lambda\rangle = \sum_{cv\mathbf{k}} A^{\lambda}_{cv\mathbf{k}} |\psi_{eh}\rangle$. The exciton weights we obtain for Sn-based materials are localized near the band edges, which leads to a large delocalization in real space. For the cases of Zr- and Te-iodides, the weights are still localized near the band edges but less than in the previous case, leading to a degree of localization in real space. Finally, the weights span the entire Brillouin zone for Zr- and Te-bromides, leading to strong localization in real space. The material's order from Wannier-like to Frenkel-like excitons perfectly follows the exciton binding energy trend. To support this statement, we also compare our ab-initio results with the semi-empirical Wannier-Mott model. The Wannier-Mott type of exciton is usually found in semiconductors with small band-gaps and high dielectric constants. As a result, the Coulomb interactions between electrons and holes are intensely screened, leading to small binding energies and a delocalization of the exciton wavefunction. Within the hydrogenoid WM model, the binding energies and exciton Bohr radius are obtained via the following equations [173]

$$E^b_{WM} = -\frac{\mu Ry}{m_0 \varepsilon^2_\infty}, \tag{4.2}$$

$$r_{WM} = \varepsilon_\infty \frac{m_0}{\mu} a_b, \tag{4.3}$$

where μ represents the reduced effective mass of the charge carriers, ε is the dielectric constant, R_y is the Rydberg constant and a_b is the Bohr radius. We show that the model fails to qualitatively assess the relationship between the exciton binding energies for all cases but the strongly delocalized Cs_2SnI_6 material. Table 4.6 contains all parameters necessary for the Wannier-Mott model.

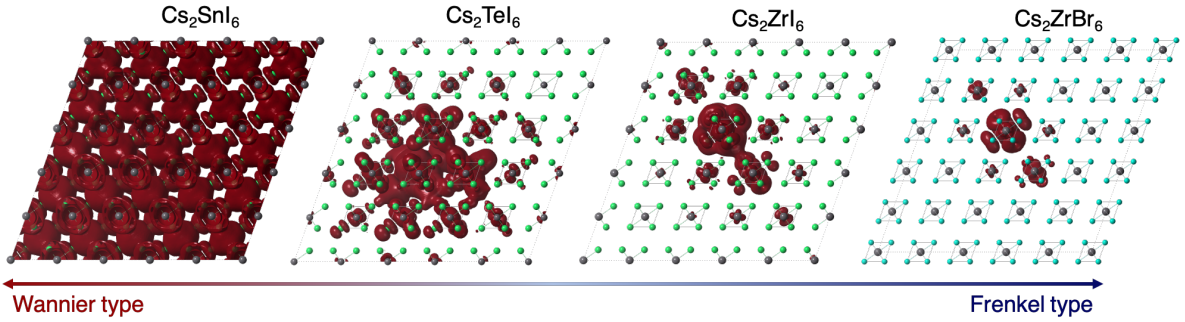

Figure 4.15 – Exciton spatial distribution $|\Psi(r_h, r_e)|^2$ for the bright exciton of Cs_2SnI_6, Cs_2TeI_6, Cs_2ZrI_6 and Cs_2ZrBr_6. The hole position r_h is fixed in the vicinity of the halogen atoms. The wavefunctions are plotted using 85% of the maximum isovalue. Figure adapted from reference [162].

4.9 Fine Structure of Excitons

In this section, we discuss in-depth the symmetry and fine structure of the excitons. The exciton state discussed before can also be written in terms of the electronic wavefunctions for the valence and conduction band states as $|\lambda\rangle = \sum_{cv\mathbf{k}} A^{\lambda}_{cv\mathbf{k}} |\psi_{v\mathbf{k}}\rangle \otimes |\psi_{c\mathbf{k}}\rangle$. The direct product between wavefunction is equivalent to the analysis of the direct product between the irreducible representations of these states, which represents the symmetries of each one of these wavefunctions. More generally, the symmetry of an exciton will be given by a direct product between the irreducible representations of the corresponding electron-hole pairs multiplied by an envelope function. As we show in Figure 4.16, the bright exciton of Cs_2SnBr_6 is originated from localized transitions around Γ from the VBM-1 to CBM, and also small contributions from the optically forbidden transition from VBM to CBM. In contrast, for Cs_2SnI_6, the last contribution is not observed due to the large energy separation between the VBM and VBM-1. By tak-

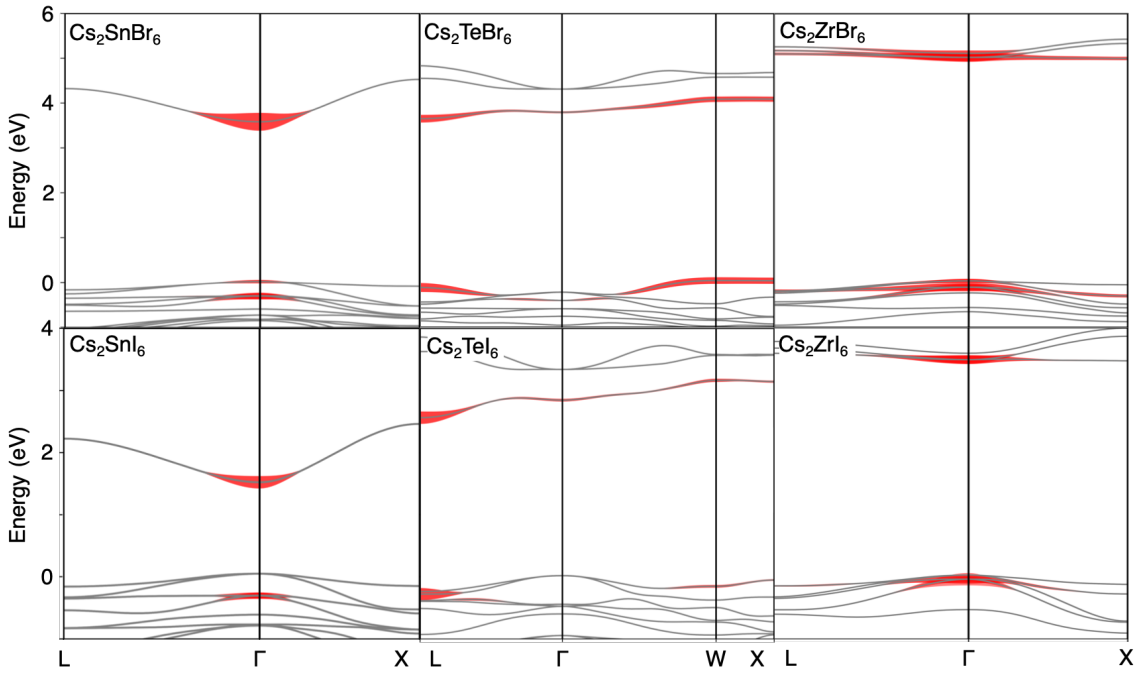

Figure 4.16 – Projection of the weights $|A^{\lambda}_{eh}|$ over the DFT-PBE band structure. The band-gaps are rigidly shifted to match the G_0W_0 calculation. Here $|A^{\lambda}_{eh}|$ represents the expansion coefficient of the first bright exciton eigenvectors in terms of the electron-hole pairs $|eh\rangle$, i.e., $|\lambda\rangle = \sum_{eh} A^{\lambda}_{eh}|eh\rangle$. Figure adapted from reference [162].

ing the correspondent representations for Cs_2SnBr_6, we obtain $F_{3/2,u} \otimes E_{1/2,g} = E_u \oplus T_{1u} \oplus T_{2u}$ multiplied by a s-like envelope function (i.e. for s-like excitons, and hence doesn't change the symmetry). For Cs_2TeX_6, the main contributions come from transitions from the VBM to CBM at L, with small contributions around the W high-symmetry point. By performing the symmetry analysis at the L point we obtain $E_{1/2,g} \otimes E_{1/2,u} = E_u \oplus A_{2u} \oplus A_{1u}$. Finally, for Cs_2ZrX_6 the contributions are originated from transitions from VBM to CBM at the Γ point, leading to $F_{3/2,u} \otimes F_{3/2,g} = A_{1u} \oplus E_u \oplus 2T_{1u} \oplus 2T_{2u} \oplus A_{2u}$. We also observe small contributions from the transition VBM to CBM+1 for the bromide compound due to the CBM and CBM+1 being closer in energy when compared to iodides.

These bright exciton states originate from electrons and holes with anti-parallel spins and can recombine quite easily via the emission of a photon and thus exhibit fast lifetimes [103]. However, a bounded state with parallel spins can also exist, and due to spin momentum conservation rules, these cannot recombine via the direct emission of a photon and thus exhibit larger radiative lifetimes compared to bright excitons. These states are often called dark ex-

citons and are not intrinsically optically active, i.e. their oscillator strength is zero, and arise from the electron-hole exchange interaction. It is also important to note that these dark excitons are intrinsically connected to the bright exciton via their wavefunctions, making dark excitons fundamentally different states than standard optically forbidden transitions. Dark excitons and their energy split from the bright states (Δ_{db}) are of particular interest for a couple of state-of-art technologies such as optically controlled information processing and fast/slow light applications [103]. Figure 4.13(b) and Table 4.6 summarizes the obtained Δ_{db} values for all compounds in this work, while Figure 4.14(b) presents the discussed exciton symmetries and fine structure.

Table 4.6 – Exciton binding energies E^b_{BSE} and dark-bright splitting (Δ_{db}) obtained from BSE@G_0W_0. The exciton binding energy is defined as the energy difference between the first direct dipole-allowed electronic transition and the first bright excitonic peak. The parameters employed for the Wannier-Mott model are also shown. The number between parenthesis represents the calculation with heavy effective masses.

Compound	Cs_2SnBr_6	Cs_2SnI_6	Cs_2TeBr_6	Cs_2TeI_6	Cs_2ZrBr_6	Cs_2ZrI_6
E^b_{BSE} (eV)	0.510	0.190	1.240	0.530	0.780	0.540
Δ_{db} (meV)	6	4	155	71	34	24
ε_∞	3.30	4.84	3.62	4.81	3.20	4.02
me^*_{GW}	0.24	0.29	0.29 [0.50]	0.33 [0.67]	1.23 (4.17)	0.85 (3.20)
mh^*_{GW}	0.37 (0.77)	0.54 (0.65)	0.22 [1.80]	0.21 [2.30]	0.61 (1.10)	0.33 (0.48)
μ	0.182	0.200	0.161	0.185	0.870	0.417
E^b_{WM} (eV)	0.228	0.116	0.167	0.109	1.156	0.351
r_{WM} (Å)	9.54	12.76	11.83	13.69	1.94	5.04

From the symmetry analysis performed for Cs_2SnX_6, we find an E_u doublet dark exciton state, which is split from the bright triplet peak T_{1u} by 6 and 4 meV for bromide and iodide, respectively. The splitting between the bright peak T_{1u} and the optically inactive triplet state T_{2u} is also observed. For the Te-based compounds, we find an A_{1u} dark singlet exciton, which is split from the bright peak, which is composed by an optically active doublet E_u and singlet A_{2u}. The dark-bright splittings are 155 and 71 meV for Te-based bromide and iodide compounds, respectively. The energy difference between the E_u and A_{2u} states is below the resolution of our calculation, and as so, they are treated as practically a triple degenerated state. Due to the large

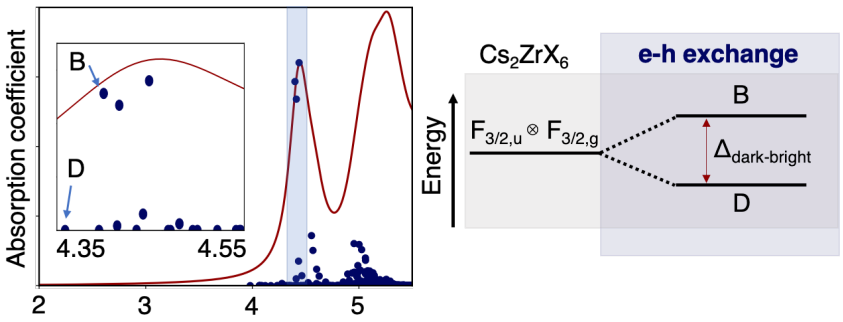

Figure 4.17 – Calculated exciton oscillator strength with fine structure shown as inset plot for Cs_2ZrBr_6. On the right an illustration of the dark-bright splitting. Figure adapted from reference [162].

number of energetically close electronic states near the VBM, a strong coupling of the valence bands and many transition states are expected for Zr-based compounds. In practice, this leads to several oscillator strengths near the bright exciton peak, which do not allow proper identification of the sixteen $A_{1u} \oplus E_u \oplus 2T_{1u} \oplus 2T_{2u} \oplus A_{2u}$ predicted states, as shown in Figure 4.17. Yet, by analyzing the electron-hole pairs contributions presented earlier, we identify the dark state as originating from the VBM to CBM transition at the Γ point. The dark-bright splittings are 34 and 24 meV for bromide and iodide, respectively. Overall, Δ_{db} decreases from Te, Zr to Sn, with Te-based materials exhibiting the largest dark-bright splitting when compounds with the same halogen are compared. Furthermore, Br-based materials exhibit larger splittings than I-based ones.

To better understand the large dark-bright splittings of Te-based materials, we also solve the BSE without including the electron-hole exchange interaction $\bar{V}^{vck}_{v'c'k'}$ (See Chapter 4). Figure 4.18 demonstrates that the spectrum renormalization caused by the electron-hole exchange interaction is always more significant for Br-based materials than I-based ones. This trend has also been observed for Pb-based halide perovskites nanocrystals [174], for which bromides' larger exciton binding energy is attributed to the larger electron-hole exchange interactions. This interaction appears to be particularly strong in the case of Te-based compounds. For the VODPs, metal, and halogen substitution allow the tuning of Δ_{db} within a considerable range from 4 to 155 meV.

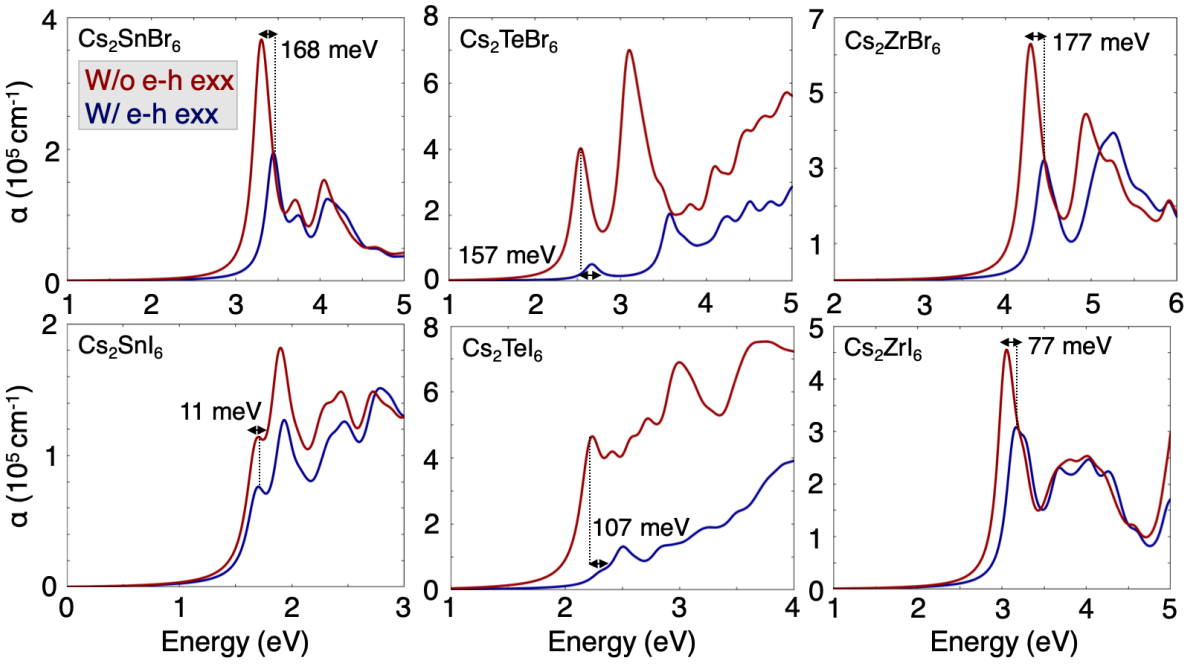

Figure 4.18 – Comparison between the absorption coefficient obtained by solving the BSE with and without the inclusion of the electron-hole exchange interaction term $\bar{V}^{vck}_{v'c'k'}$ (See Chapter 4). The black dotted lines show the position of the first direct dipole-allowed transition E^d_g at G_0W_0 level. Figure adapted from reference [162].

Take-home Messages

- In VODP, the non-corner-sharing MX_6 octahedra are quasi-isolated structures, exhibiting the same band splittings that one would expect from tetrahedrally coordinated atoms, as predicted within the crystal field theory models shown in Figure 4.4.
- The compounds discussed here exhibit stable lattice dynamics and seem to exhibit a domain of chemical stability. This reveals Cs_2ZrI_6, an unexplored material, as a potential candidate for optoelectronic applications.
- Based on their electronic structure, we find Te-based compounds most interesting for hole transport, while Sn-based compounds are suitable for electron transport.
- We show that electron-hole interactions play a major role in the optical properties of the VODPs. They exhibit large and tunable exciton binding energies through a range of 0.2-1.2 eV and dark-bright splitting through a range of 4 to 155 meV by both M- and X-site composition.
- Via a joint analysis of the exciton wavefunctions and exciton binding energies, we conclude that the VODPs can host both Wannier- and Frenkel-type excitons depending on the choice of M- and X-site species.
- Finally, due to the large and/or indirect electronic band-gaps, heavy effective masses of charge carriers, and the strong electron-hole coupling, these materials cannot be suitable alternatives to Pb-free photovoltaic devices. However, they present great opportunities for light-emission and quantum optical technologies.

The results discussed in this chapter have been published in two different works. One published in *Applied Physics Letters* which can be found at reference [157], and a second one featured at the front cover of *ACS Materials Letters* which can be found at reference [162].

CHAPTER 5

LAYERED HALIDE DOUBLE PEROVSKITES

In this chapter, I will present the investigation of the structural and electronic properties of layered halide perovskites. This work is a collaboration with Prof. C. C. Stoumpos and Dr. M. Maniadi from the University of Crete in Greece. I will present a series of newly synthesized lead-free layered double perovskites by our collaborators, and structural models I developed to probe their electronic structure. This collaboration was established as an initiative of our collaborators to establish a theoretical framework for the newly synthesized structures. I will start the discussion by introducing the relationship between layered perovskites and layered double perovskites. Following, the models will be introduced and applied to predict these materials' properties. These results will be compared side-by-side with the available experimental data.

ABX_3 perovskite materials are obtained via the combination of metal- and halide-based (or organic-based) salts, such as ABr (A=Cs^+, $CH_3NH_3^+$ or $HC(NH_2)_2^+$) and $PbBr_2$. Due to the small size of the A-site cations, these structures will crystallize in a 3D corner-sharing octahedra network characterized by the AMX_3 stoichiometry. However, by introducing a combination of large and small A-site cations, it is possible to break the connectivity of the octahedra network along certain directions to form layered perovskites [175], as discussed in more detail at the introduction of this thesis. Two main phases of layered perovskite can be formed depending on

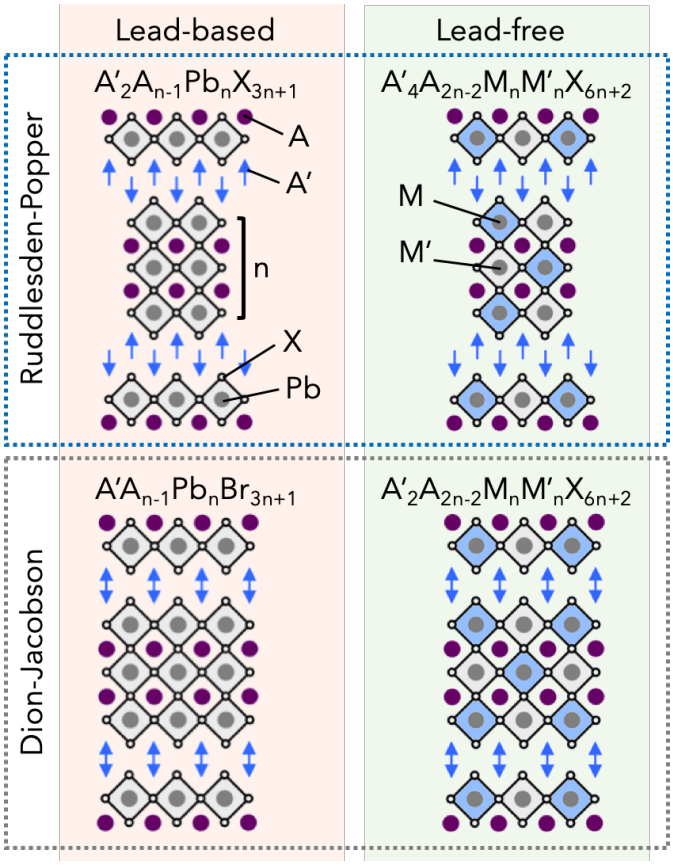

Figure 5.1 – Representation of different types of layered perovskite materials. We split them according to the stacking type, i.e. Ruddlesden-Popper or Dion-Jacobson phases, and also between lead-based (layered perovskite) and lead-free (layered double perovskite). The parameter *n* indicates the number of inorganic layers being separated by the long cations A'.

the characteristics of the chosen A-site cation, the Ruddlesden-Popper (RP) or Dion-Jacobson (DJ) phase. These are usually characterized according to the relative shift of the inorganic layers along the stacking direction, as represented in Figure 5.1. The DJ phase exhibits no relative shift between the inorganic layers, leading to octahedra stacked on top of each other. The RP

phase exhibits a relative shift of $(0.5, 0.5, 0.0)$ between the inorganic layers separated by the long cations A'. RP layered perovskites have been extensively investigated throughout the past couple of years, while DJ phases are a relatively rare phase of layered perovskite. Regardless of the layered perovskite phase, we commonly categorize these materials according to the number of perovskite layers that are sandwiched between the long organic cations, given by the parameter n shown in Figure 5.1. Nowadays, 2D halide perovskites are broadly investigated for optoelectronics due to their highly tunable chemical and physical properties, which can be achieved by changing the halogen/metal composition [176] by the introduction of mixed small and large organic cations [177] and also by engineering the slab thickness via the parameter n [178]. Yet, as for the three-dimensional case, the presence of lead in these materials is still a point to be addressed.

A possible solution is to work with layered double perovskites, which are lead-free analogs of conventional layered perovskites, as investigated by Connor *et al.* [179]. These materials can be achieved during synthesis by substituting the input lead-based salt with two different metal-halide salts. This will lead to new structures which highly resemble the conventional layered perovskites. However, the metal sites that were previously occupied by lead now will be occupied by the new metal species in a rock-salt-like arrangement [28], as shown in Figure 5.1. In this chapter, I will investigate three new layered double perovskite materials synthesized by our collaborators M. Maniadi and C. C. Stoumpos from the University of Crete. These materials exhibit a DJ phase based on the short cation 4-aminomethyl piperidine ($CH_6H_{14}N_2$). Furthermore, they are $n = 1$ type and are defined by the general stoichiometry (4-AMP)$_2$AgMBr$_8\cdot$ H$_2$O (M=Bi, Sb, In), differing on the M-site metal species.

5.1 Structural Properties

As a first approach, I employed the experimentally reported structures and performed a structural optimization of the atomic position and lattice parameters. For this purpose, I employ the PBEsol functional and optimize the inorganic perovskite layer. During this process, the organic network was kept frozen due to the fact that some of the atoms in the organic network are given via partial occupations and have to be placed in the structure manually. More details about the computation can be found in the Appendix A.3. We obtained good agreement for all the calculated bond lengths compared to the experimental data. Significant Ag-Br octahedra distortions are observed, with the octahedra elongated along the in-plane direction and shortened along the stacking direction, as seen in Figure 5.2(a). Moreover, the Ag-Br distortions are

more significant for In and smaller for Bi, which follows the same measured trend. The M-Br octahedra are relatively isotropic and exhibit similar bond lengths along both directions. We also quantify the interlayer distance *d*, which in this work is defined as the shortest distance between two halogens of different layers. We obtain distances of 4.18 Å, 4.00 Å, and 3.93 Å for In-, Sb- and Bi-based materials, which are between the shortest ones ever synthesized. Short interlayer distances can be particularly important for electronic transport, as charge carrier mobilities along the stacking directions are usually hindered due to the large organic cations [180].

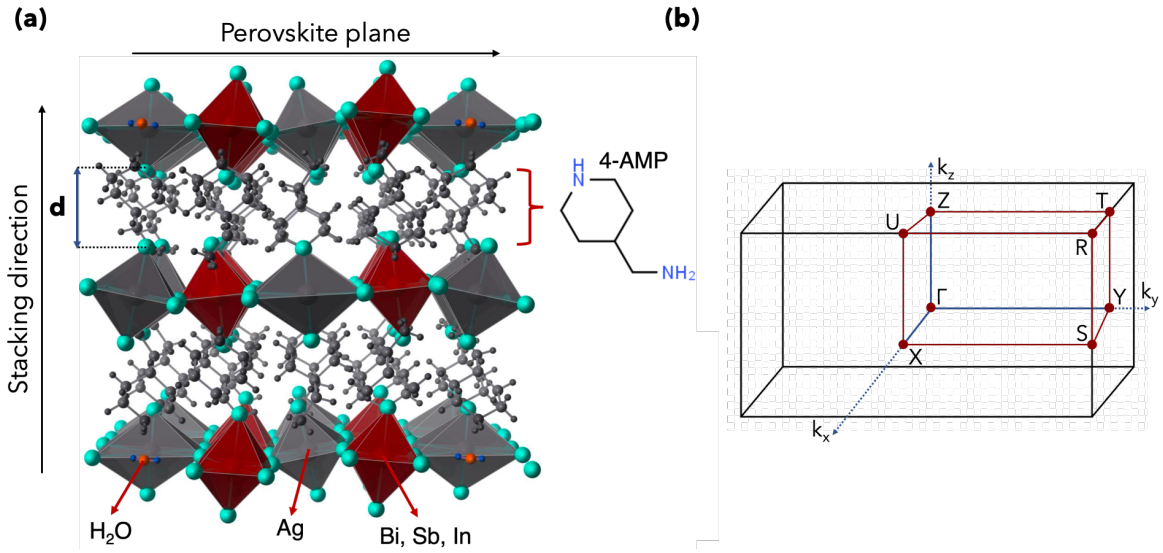

Figure 5.2 – (a) Schematic representation of the three two-dimensional double perovskite materials. The stacking direction and the perovskite inorganic plane are shown. (b) Brillouin zone of the layered systems. The stacking direction is defined along the Γ-X high symmetry path.

Table 5.1 – Summary of the DFT-PBEsol and experimental bond-lengths for (4-AMP)$_2$AgMBr$_8$· H$_2$O (M=Bi, Sb, In).

M-site Metal	DFT (Å)				Exp. (Å)			
	In-plane		Out-of-plane		In-plane		Out-of-plane	
	Ag-Br	M-Br	Ag-Br	M-Br	Ag-Br	M-Br	Ag-Br	M-Br
In	3.40	2.71	2.51	2.70	3.47	2.70	2.49	2.68
Sb	3.37	2.84	2.52	2.82	3.36	2.76	2.50	2.89
Bi	3.35	2.88	2.54	2.87	3.16	2.86	2.56	2.90

5.2 Electronic Properties

Next, we evaluate the electronic band structures for all three compounds, as shown in Figure 5.3(a-c). Bi- and Sb-based compounds exhibit a direct band of 1.76 eV and 2.23 eV at the Γ-point, while In-based exhibit an indirect band-gap between the Z to Γ high symmetry points. The Brillouin zone of these systems is shown in Figure 5.2(b). The PDOS analysis shows that the VBM of all compounds originated from hybridization between Ag-d and Br-p orbitals. The CBM of Bi- and Sb-based materials are mainly composed of the metal site p-orbitals and Br-p orbitals, but one can observe tiny contributions of Ag-d states as well. For In-based, we see the same contributions of the halogen and Ag atoms, but s-orbitals of In.

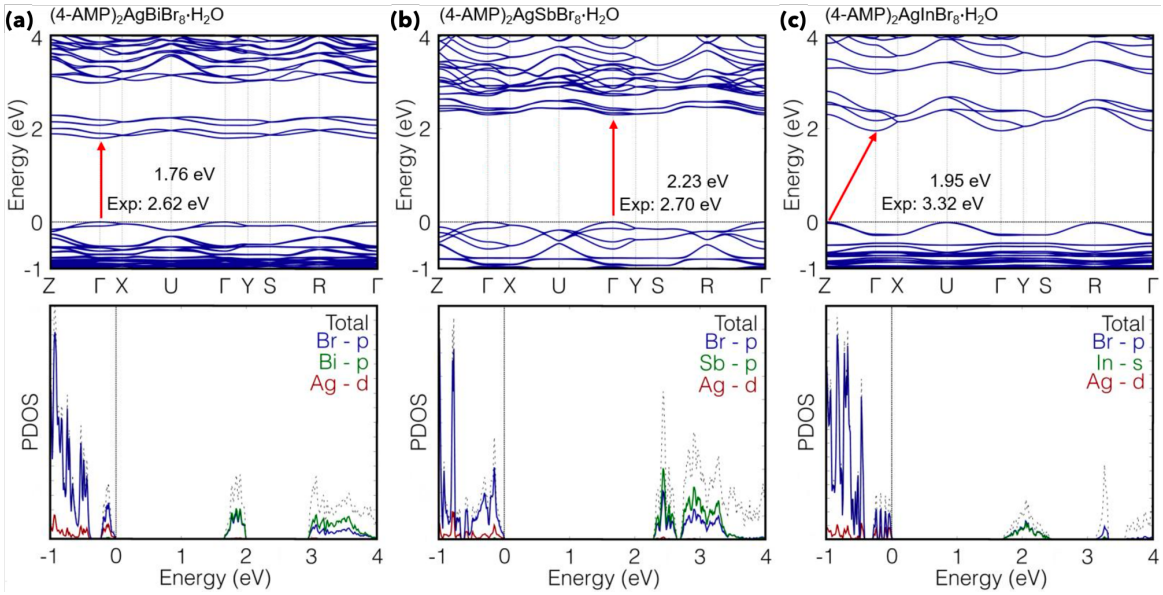

Figure 5.3 – Electronic bands structure for (a) $(4\text{-AMP})_2AgBiBr_8 \cdot H_2O$, (b) $(4\text{-AMP})_2AgSbBr_8 \cdot H_2O$ and $(4\text{-AMP})_2AgInBr_8 \cdot H_2O$. The projected density of states is also shown.

We also perform a band symmetry analysis of the electronic bands. These materials crystallize in the non-centrosymmetric space group $P2_12_12$ which leads to the C_2 point-group at the Γ point. We find that both Bi- and Sb-based compounds exhibit the *B* irreducible representation at the VBM and CBM, while the VBM-1 state has irreducible representation *A*. The transition *B* to *B* (VBM to CBM) is only allowed for light polarization along the stacking direction. In contrast, the transition *A* to *B* (VBM-1 to CBM) is only allowed for light polarization in the perovskite plane, defined in Figure 5.2(a). The stacking direction can be found at the band structures along the Γ-X path, which shows slightly dispersive bands due to the interlayer inter-

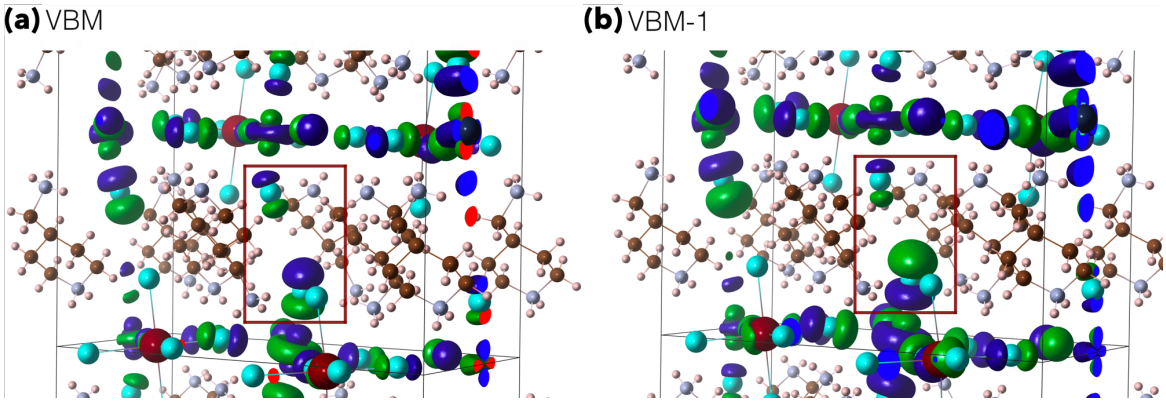

Figure 5.4 – Charge density representation of the (a) anti-bonding and (b) bonding states at the VBM of $(4\text{-AMP})_2AgBiBr_8 \cdot H_2O$

action generated by the short distance between the perovskite layers. Band splittings are caused by the interlayer interaction, which generates the VBM and VBM-1 pair of bands and CBM and CBM+1. Figure 5.4 shows the electronic wavefunctions at the VBM and VBM-1. These correspond to the bonding and anti-bonding interlayer interaction. The anti-bonding state is less stable and located at the VBM, while the more stable bonding state can be found at the VBM-1. We quantify the strength of this interaction by taking the energy difference between each pair of these states at the Γ point. At the VBM, these splitting are 20 meV, 130 meV, and 100 meV, while at CBM, they are 90 meV, 200 meV, and 110 meV for In-, Sb- and Bi-based compounds, respectively.

5.3 Structural Models for Layered Perovskites

To understand the impact on the electronic structure generated by the different structural features that we observe in the experiments, such as octahedra tilting and Ag-Br octahedra distortions, we develop four different models that capture some of these effects, as shown schematically in Figure 5.5(a). Model 1 is the simplest exhibiting no octahedra tilting or distortions. In model 2 we add octahedra tilting, while in model 3 we add distortions. Finally, in model 4 both octahedra tilting and distortions are taken into account. In order to remove the effects of distortion in models 1 and 2 we optimize the lattice parameters, as the octahedra distortion induces an anisotropy in the perovskite plane's lattice parameters. In models 3 and 4 we fix the lattice parameters to the experimental values.

Our first step towards building these simpler models was to verify whether the organic

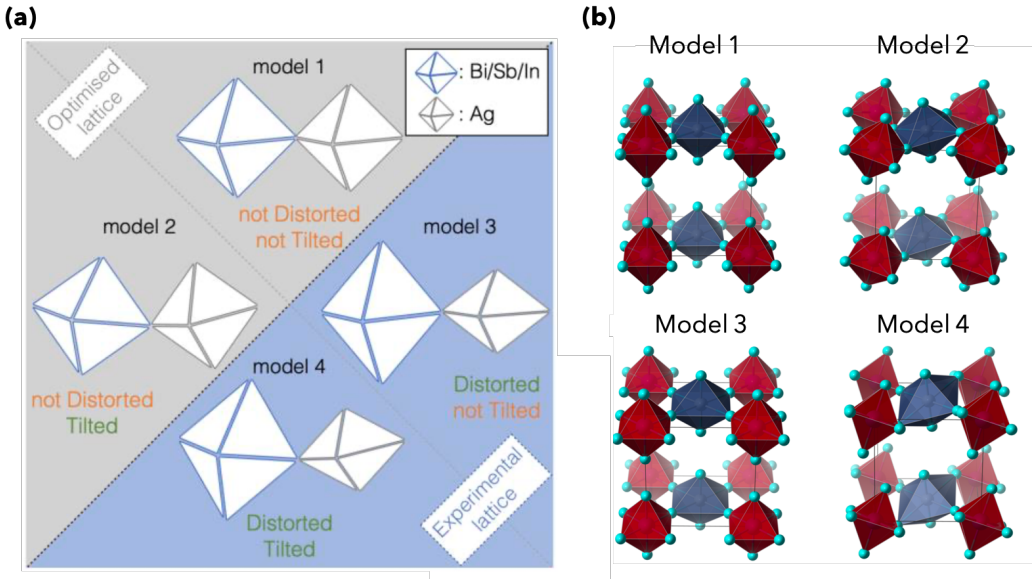

Figure 5.5 – (a) Illustration of the four structural models developed for this work. (b) The four simplified model structures to capture the effects of tilting, distortion, and their combination.

cation separating the layers has an important role in the electronic structure. Figure 5.6 shows a comparison between the band structure of the full $(4\text{-AMP})_2AgBiBr_8 \cdot H_2O$ compound and its simplified version $[AgBiBr_8]^{-2}$, where we charge the cell in the later case to compensate the missing organic cation charge. The bands' dispersion remains unchanged, and we observe a relatively small band-gap shift of 110 meV, allowing us to remove the organic spacer and water molecules. The final models after optimizations and removal of organic cations are shown in Figure 5.5(b).

5.4 Electronic Structure of the Models

After setting up these simple models, our main goal is to be able to compare their band structure with the full compounds discussed in Figure 5.3. However, the experimental structures correspond to $2 \times 2 \times 1$ super-cells of our models. We first employ a band structure unfold procedure to establish a common ground for comparing the two systems.

The Brillouin zone unfolding technique has been developed by V. Popescu and A. Zunger and has been implemented by M. Zacharias and F. Giustino in the Quantum ESPRESSO package [181, 182]. It consists in evaluating the electron spectral function in the Lehman represen-

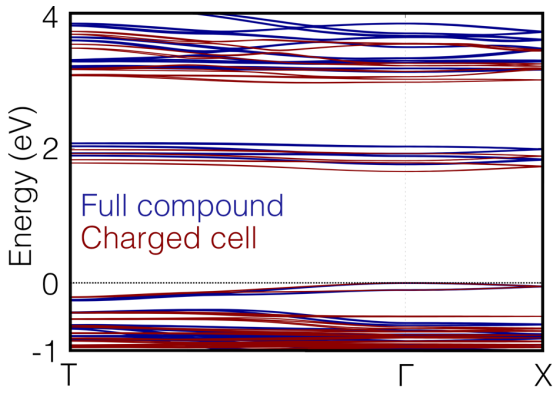

Figure 5.6 – Comparison between the band structure of the full $(4\text{-AMP})_2AgBiBr_8 \cdot H_2O$ compound and its simplification $[AgBiBr_8]^{-2}$, where a background charge is added to compensate the missing charge.

tation, which is given by

$$A_{\mathbf{k}}(\varepsilon) = \sum_{m\mathbf{K}} P_{m\mathbf{K},\mathbf{k}} \delta(\varepsilon - \varepsilon_{m\mathbf{K}}), \tag{5.1}$$

where $\varepsilon_{m\mathbf{K}}$ is the energy of the KS state $\left|\Psi^{SC}_{m\mathbf{K}}\right\rangle$ of the super-cell structure and $P_{m\mathbf{K},\mathbf{k}}$ are the spectral weights defined as

$$P_{m\mathbf{K},\mathbf{k}} = \sum_{n} \left|\left\langle \psi^{SC}_{m\mathbf{K}} \middle| \psi_{n\mathbf{k}} \right\rangle\right|^2. \tag{5.2}$$

These spectral weights represent the overlap probability between the super-cell states with wavevector $\mathbf{K}$ with all KS states from the reference primitive or conventional cell. This procedure is useful as it will allow us to unfold the super-cell band structure in the primitive Brillouin zone of our model systems.

Figure 5.7 shows the unfolded band structure of the Bi-based material compared to the four structural models presented earlier in this section. The models introduced in Figure 5.7(a) and Figure 5.7(c) reproduce well the features of the conduction band states while not perfectly the valence states. Figure 5.7(d) describes the valence states nicely but fails to describe the conduction states, while Figure 5.7(c) seems to show the best agreement between the model and the full calculation. We also note that all models reproduce the band-gap of the full structure. Overall, Ag-Br distortions appear to have a role in the valence states together with tilting, while the conduction bands are mainly dictated by octahedra tilting. We also compare our best model, shown in Figure 5.7(b), with the unfolded band structure of the other compounds, as shown in Figure 5.8. The model reproduces well the main features of the band structure of all compounds, also showing a good agreement for the band-gaps. Surprisingly, the model that features both

tilting and distortion does not lead to the best description of the electronic band structures. It is possible that the DFT optimization can not capture correctly the averaged distortions seen in the experimentally resolved structures, leading to unrealistically distorted octahedra.

Due to the simplicity of the models developed in this chapter, they can be used as a basis for higher-level calculations that would not be trivial to perform using experimental structures, such as optical absorption simulations, hybrid functionals, and GW calculations. In the next chapter, similar models will be used as a basis to perform state-of-art transport calculations.

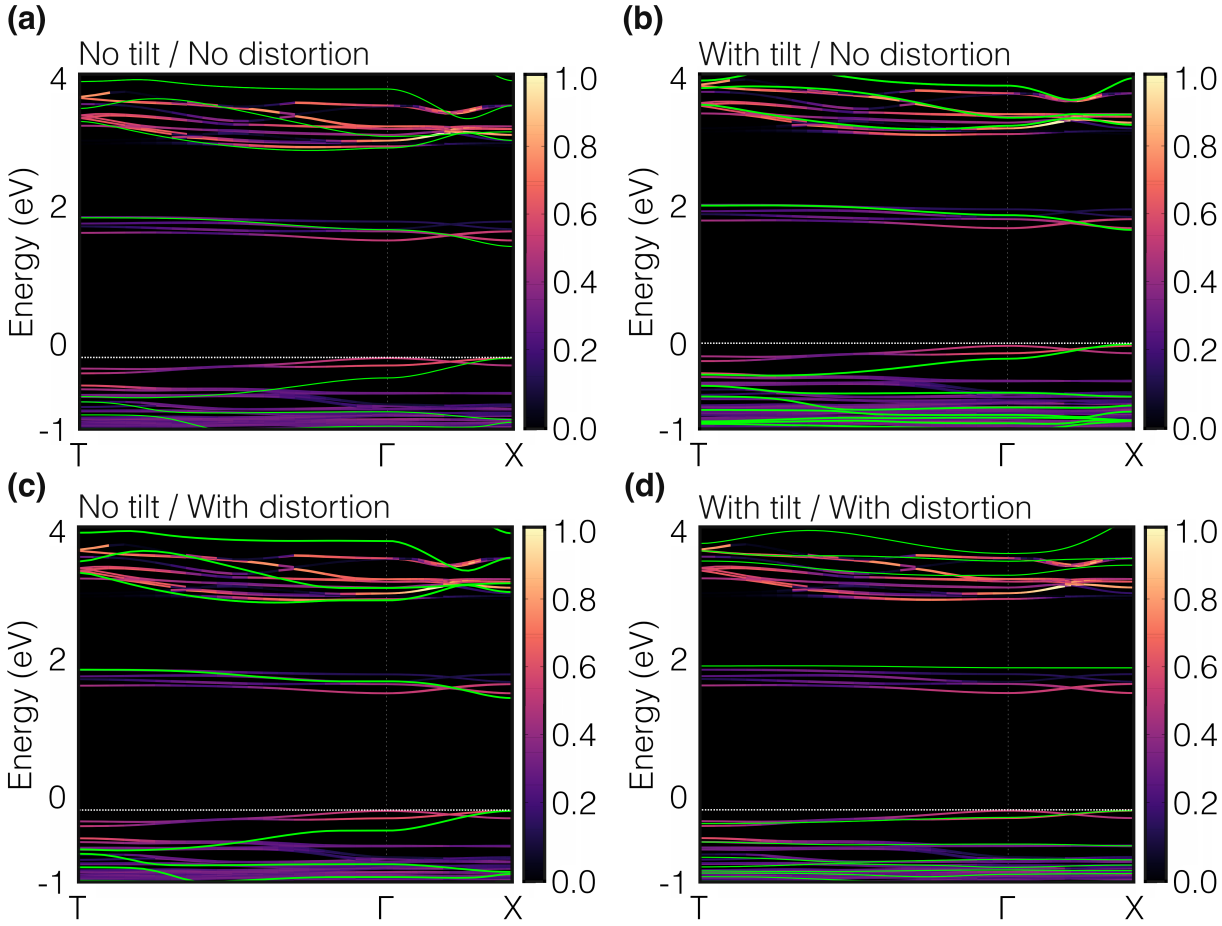

Figure 5.7 – Comparison between the unfolded band structure of (4-AMP)$_2$AgBiBr$_8$· H$_2$O and the model structures featuring (a) no tilting and no distortions, (b) tilting and no distortions, (c) distortions but no tilting and (d) tilting and distortions. Green lines represent the model's band structures, and the colored spectral functions are the unfolded bands.

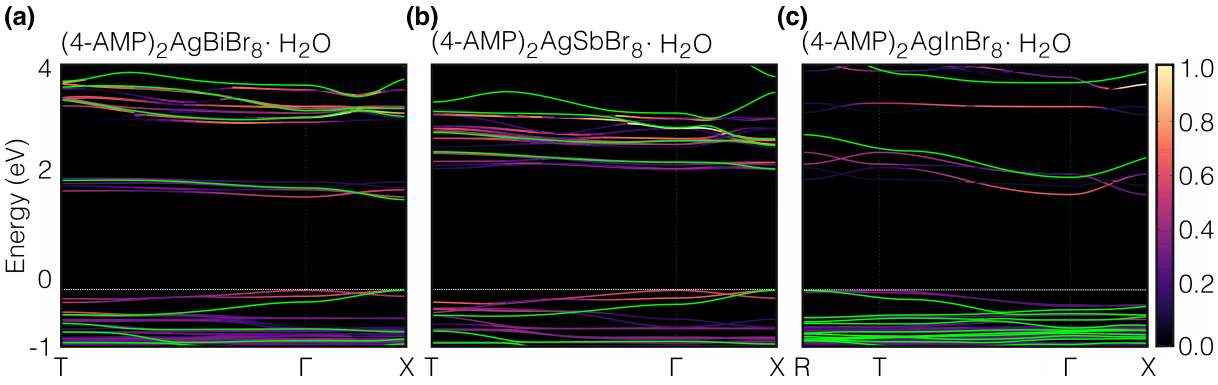

Figure 5.8 – Comparison between the model containing tilting and no distortions (Figure 5.7(b)) and the unfolded band structure of the (a) Bi-, (b) Sb- and (c) In-based systems.

Take-home Messages

- Three DJ layered perovskite materials, namely (4-AMP)$_2$AgMBr$_8$· H$_2$O (M=Bi, Sb, In), have been synthesized for the first time. These compounds are based on the short 4-aminomethyl piperidine cation and exhibit one of the smallest interlayer distances available in the literature [183].
- We developed very simple models to isolate and investigate different structural features of the experimental structures. Although simple, these models can reproduce most features of the full compound band structures and band-gaps, allowing higher-level calculations in layered perovskite systems for a much cheaper computational cost.
- Due to the very short interlayer distances, we predict and observe an interlayer band splitting in bonding and anti-bonding states. We can also quantify this splitting and investigate its role in the optical properties via a band symmetry analysis.

A manuscript related to this work is currently under preparation with our experimental collaborators.

CHAPTER 6

THE ORIGIN OF LOW CARRIER MOBILITIES IN LAYERED PEROVSKITES

In this chapter, I will discuss the transport properties of layered and three-dimensional systems by means of electron-phonon coupling calculations. Due to the highly demanding calculations, we start by constructing a series of models for the layered systems, which are inspired by the work developed throughout Chapter 5. I will then present the primary differences between these systems' electronic and phononic properties. Next, I will apply the ab-initio Boltzmann equation to evaluate transported properties such as charge carrier scattering rates and mobilities. Following, we will use symmetry analysis to understand the origins of electron-phonon coupling in these materials and point out the difference between the charge carrier transport in layered and three-dimensional systems. We finalize this chapter by discussing the origin of low carrier mobilities in layered perovskites. This work has been made in collaboration with the group of Professor Feliciano Giustino at the University of Texas at Austin, the lead developers of the EPW code for electron-phonon physics.

Throughout Sections 3, 4, and 5, we discussed several aspects regarding the electronic and optical properties of 2D and 3D perovskites. We showed how these properties can be tuned and controlled via metal- and halogen-site substitutions and also via dimensionality engineering, e.g., Ag/Bi double salts (3D), layered perovskites (2D), and VODPs (quasi-0D). We also demonstrated that there are common features even between these different types of perovskite materials, such as the role of metals and halogens orbitals to the band edges. In particular, for the case of 2D and 3D perovskites, one can also establish straightforward connections between the structural properties of the layered octahedra network and the 3D system. Despite the similarities between the electronic and optical properties of layered and three-dimensional systems, transport-related properties such as charge carrier mobilities, are experimentally observed to be orders of magnitude smaller for the layered materials than the ones observed for ABX_3 perovskites. The reduced charge carrier mobilities significantly impact these materials' application

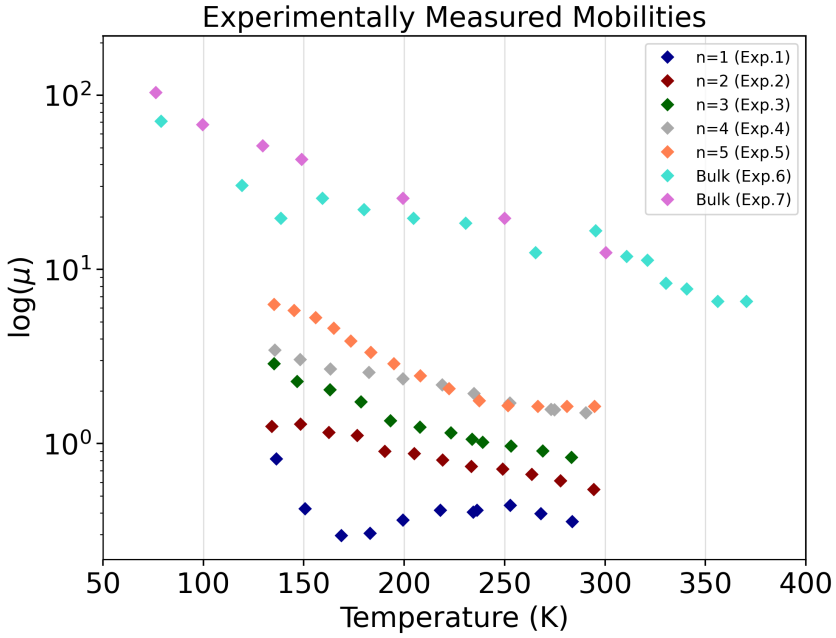

Figure 6.1 – Experimentally measured charge carrier mobilities for layered perovskites $n = 1, 2, 3, 4, 5$ and the ABX_3 perovskite $MAPbI_3$. The experimental measurements (Exp. 1-5) were obtained from reference [178], $MAPbI_3$ (Exp. 6) from reference [184] and $MAPbI_3$ (Exp. 7) from reference [185].

in optoelectronic devices [178, 186] as it can, for example, restrict the collection of charge carriers by transport layers and hinder charge carrier separation, which affects device performance. An example of measured charge carrier mobilities for 2D and 3D systems is shown in

Figure 6.1, taken from the references [178, 184, 185]. The mobilities decrease as a function of temperature and increase as a function of the number of layers, with the upper limit being the three-dimensional system. Different mechanisms have been proposed, such as: Large carrier effective masses [178], due to the mobility being a measure of how easily charge carriers move inside of a material in the presence of an electric field. The presence of trap states [187], as these can act as recombination centers for charge carriers. Lastly, the presence of strongly bounded charge carriers (large exciton binding energies) that adversely affect charge carrier dissociation [180]. Yet, a theoretical investigation of the fundamental physical mechanisms underlying these diminished transport properties in relation to the bulk materials is missing. In this section, we focus on the transport properties of 2D and 3D perovskites and unveil fundamental aspects to understand the origin of low mobilities in 2D perovskites.

6.1 Structural Models

Starting from the ABX_3 system $CsPbBr_3$, I model the case of layered $n = 1$ (Cs_2PbBr_4) and $n = 2$ ($Cs_3Pb_2Br_7$) and compare their electronic and transport properties to the three-dimensional reference. For the layered systems, we use the high symmetry crystal structures

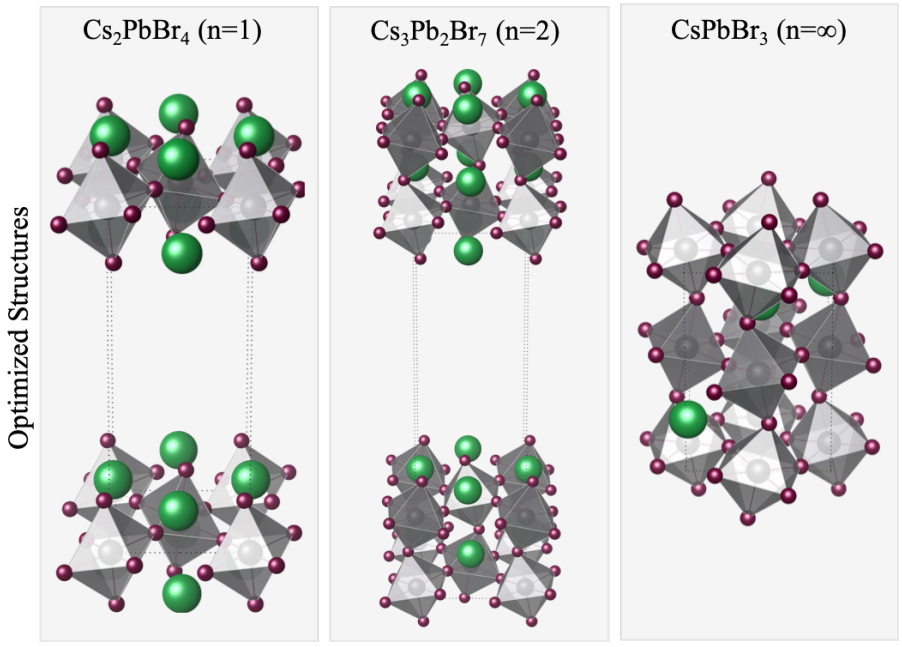

Figure 6.2 – Structural models for the $n = 1$ (Cs_2PbBr_4), $n = 2$ ($Cs_3Pb_2Br_7$) and ABX_3 ($CsPbBr_3$) structures.

and employ models inspired by the ones developed in Section 5 and shown in Figure 6.2. We employ DFT-PBE to optimize the positions of the atoms and lattice parameters for all structures. We then perform DFPT calculations to evaluate the phonon dispersion for the model systems. The models of the layered $n = 1$ and $n = 2$ have a P4/mmm symmetry (space-group 123) and exhibit negative phonons modes across the Brillouin zone, which are related to distortions between Cs and the octahedra and also octahedra tilting, shown in Figure 6.3. The

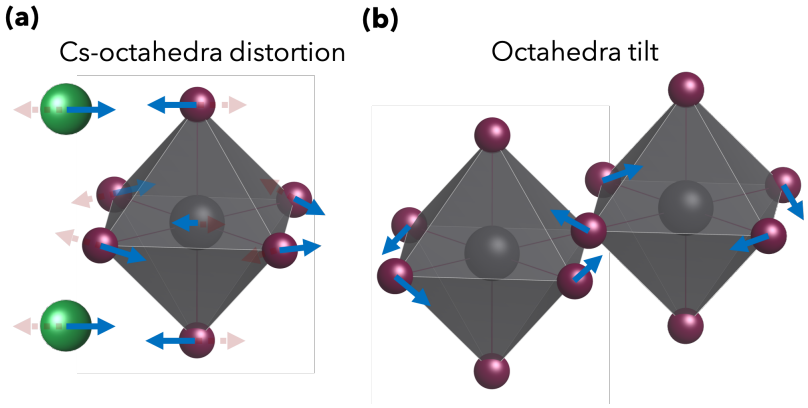

Figure 6.3 – Illustration of the (a) Cs-octahedra distortion and (b) octahedra tilt modes present in the layered systems.

phonon dispersion for the $n = 1$ structure is shown in Figure 6.4. Similarly, the ABX_3 $CsPbBr_3$ structure has a Pnma (space-group 62) symmetry and exhibits negative phonon modes related to octahedra tilting. These instabilities are known and are related to the fact that our initial models do not have tilted octahedra, while in fact, the low-temperature perovskite phase exhibits octahedra tilting [188]. To determine the ground-state (GS) structures within DFT, we displace the atoms from their optimized positions following the negative eigenmodes present in each structure. These displacements can be obtained via the atomic displacement equation 2.16 discussed in Chapter 2.4. This process is performed self-consistently for each structure until the negative phonon modes disappear. Figure 6.5(a-b) shows the GS structures and phonon dispersion we obtained via this approach for the three materials investigated in this section. All materials' highest phonon frequency modes are well within the range $140 - 150$ cm^{-1}. These values are consistent with previous phonons calculations by Poncé *et al.* for the cubic phase of $CsPbI_3$ and orthorhombic $MAPbI_3$, where these modes fall within the range $120 - 170$ cm^{-1} [36]. These phonon dispersions confirm the mechanical stability of the models with residual negative phonon modes being smaller than 0.2 cm^{-1}.

For the GS structures, we obtain average in-plane Pb-Br bond lengths of 3.05, 3.04 Å for

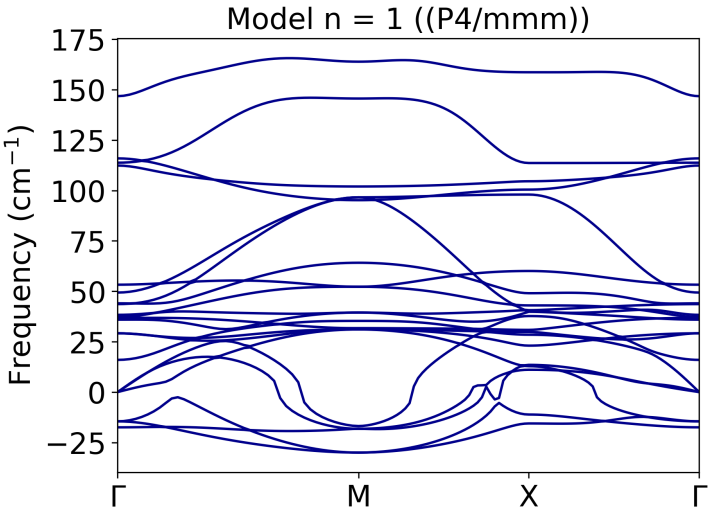

Figure 6.4 – Phonons dispersion for the model layered $n = 1$ (P4/mmm) structure.

$n = 1$, $n = 2$, respectively. While the out-of-plane Pb-Br bond lengths are 3.05 and 2.95 Å for $n = 1$, $n = 2$, respectively. For the three-dimensional system, we obtain an average Pb-Br bond length of 3.04 Å. We also evaluate the average in-plane Pb-Br-Pb octahedra tilting for each system, and we obtain 147.5°, 155.9° and 153.5° for $n = 1$, $n = 2$ and three-dimensional structures, respectively. These results reveal that a slightly larger octahedra tilt is expected for $n = 1$, while $n = 2$ and three-dimensional systems exhibit a similar degree of in-plane tilting. Also, all systems show almost identical in-plane Pb-Br bond lengths. This analysis confirms that the in-plane perovskite octahedra network remains structurally similar between the 2D and 3D systems regardless of the dimensionality reduction.

6.2 Ab-initio Charge Carrier Mobilities

6.2.1 Electronic and Phononic Properties

We move to the analysis of the electronic properties of each system, which are shown in Figure 6.5(b). All materials exhibit a direct band-gap at the Γ high-symmetry point. We obtain band-gaps of 1.86, 1.44 and 1.04 eV for Cs_2PbBr_4, $Cs_3Pb_2Br_7$ and $CsPbBr_3$, respectively. Moreover, we evaluate the in-plane charge carrier effective masses near the band edges, and we obtain effective masses of 0.40, 0.32, and $0.25m_0$ for holes and 0.30, 0.24 and $0.23m_0$ for electrons of Cs_2PbBr_4, $Cs_3Pb_2Br_7$ and $CsPbBr_3$, respectively. The effective masses are consistent with the similar structural properties discussed previously, i.e. similar bond lengths

and in-plane octahedra tilting. In this thesis, I will not discuss transport properties along the stacking directions as they are zero.

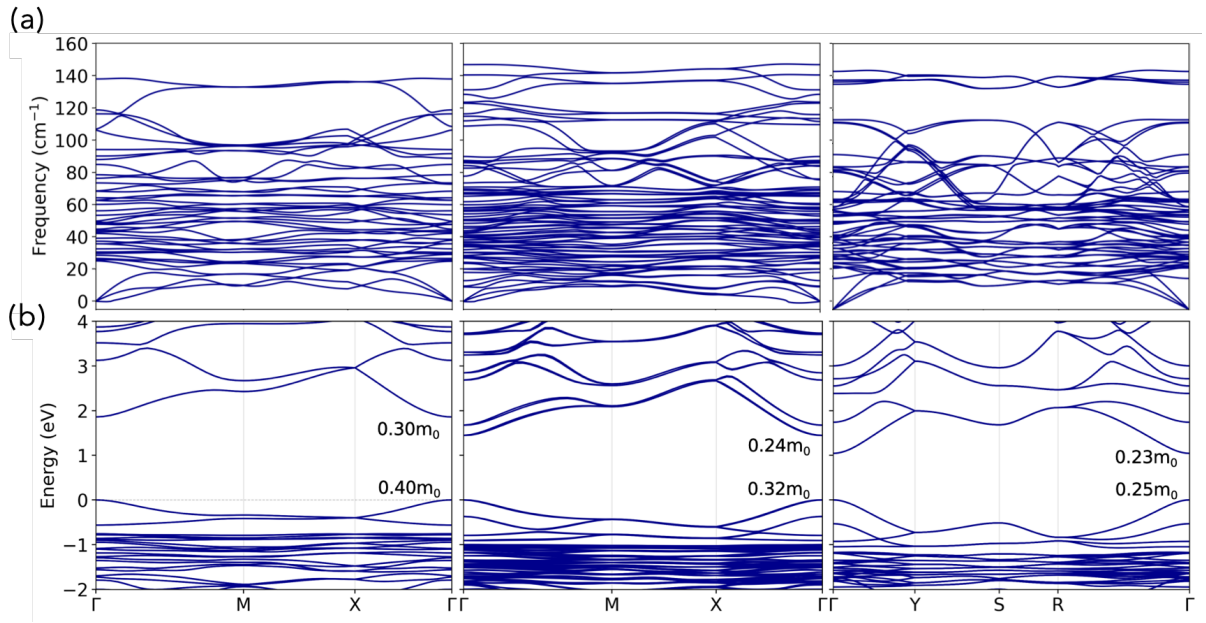

Figure 6.5 – (a) Phonon dispersions and (b) electronic structure for the layered perovskites $Cs_{n+1}Pb_nBr_{3n+1}$ ($n = 1$ and 2) and ABX_3 $CsPbBr_3$. The effective masses for the VBM and CBM are also shown.

Having obtained electronic and phonon band structures, we have all the necessary ingredients to evaluate charge carrier mobilities. A simple approach is to employ the Drude formula for mobility given by $\mu = e\tau/m^*$, which is inversely proportional to the charge carrier's effective mass. By analyzing the in-plane effective masses of the layered systems that we obtained from DFT, we conclude that these do not change enough to cause the mobility to drop orders of magnitude between the layered and three-dimensional structures, which gives us an insight that the origin of the low mobilities lies elsewhere.

6.2.2 Charge Carrier Mobility Calculations

As the Drude model is not sufficient to explain the measured mobilities, we compute transport properties ab-initio. We resort to the state-of-art IBTE approach discussed in Section 2.4. Figure 6.6(a) shows the calculated hole mobilities for the three systems discussed in this section. The mobilities of all materials are shown to decrease with the increase in temperature. This is due to the only scattering mechanism considered in our calculations being the scattering

of charge carriers by lattice vibrations, i.e., electron-phonon interactions. Therefore, as the temperature increases the electronic band edges are more populated leading to large scattering rates and consequently lower mobilities. Moreover, the mobility increases by orders of magnitudes going from the layered to the three-dimensional $CsPbBr_3$ structure, revealing that dimensionality plays a crucial role in the transport properties of perovskites. At room temperature we predict mobilities of 4.4, 10.2 and 38.5 cm^2/Vs for the $n = 1$, $n = 2$ and three-dimensional structures, respectively. The three-dimensional value is in good agreement with the 41 cm^2/Vs previously obtained by Poncé *et al.* for cubic $CsPbBr_3$[36].

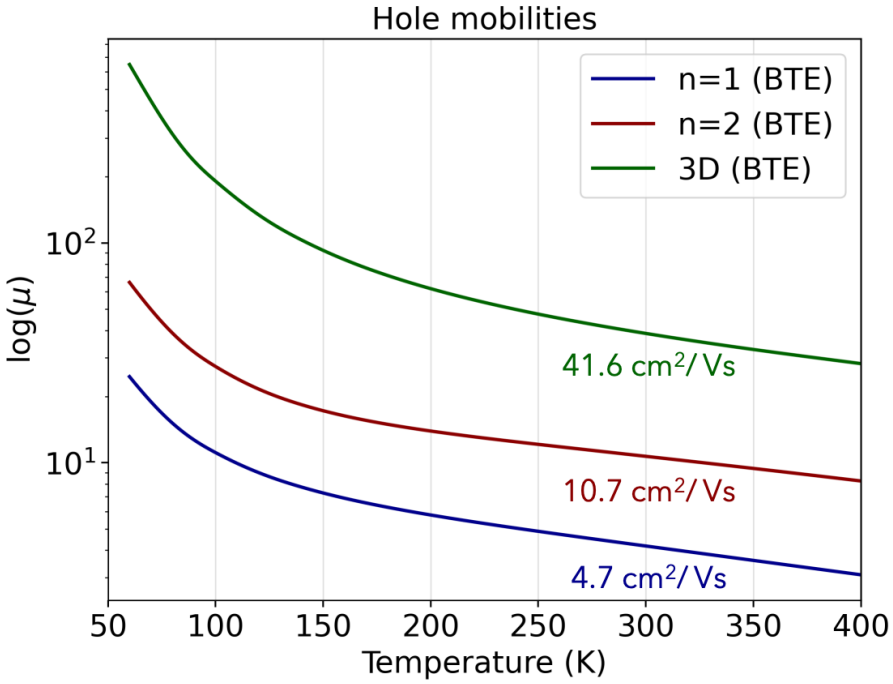

Figure 6.6 – Average in-plane hole mobilities evaluated within the ab-initio IBTE approach for the $n = 1$, $n = 2$, and three-dimensional systems. The y-axis is shown in a logarithm scale.

The calculated scattering rates (equation 2.22) associated with these mobilities are shown in Figure 6.7 as box plots. At the band extrema, the scattering rates are zero, which indicates an infinite lifetime. This is due to the band extrema being locally flat, leading to a zero band velocity, accordingly to $v_{n\mathbf{k}} = \hbar^{-1}\nabla_k \varepsilon_{n\mathbf{k}}$. We observe much larger scattering rates near the band-edges for the $n = 1$ and $n = 2$ systems than the three-dimensional structure, which ranges from one to two orders of magnitude of difference. Consequently, the mobility trend of Figure 6.6 originates from differences in the carrier lifetimes of the $n = 1$, $n = 2$, and three-dimensional.

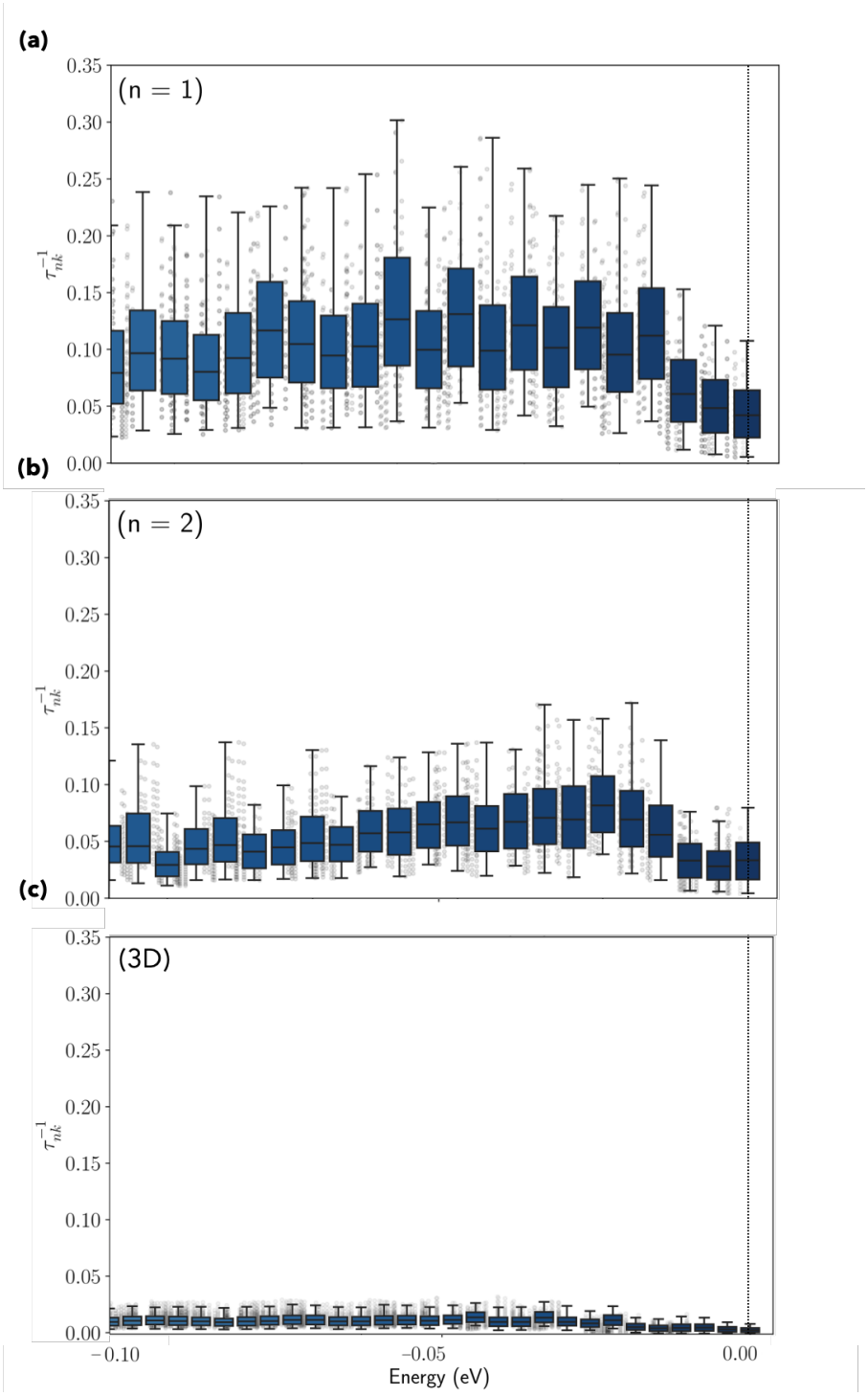

Figure 6.7 – Box plot of the scattering rates evaluated with the ab-initio IBTE approach. The whisker is set to include all the calculated data, and no outlier points are assumed. The VBM of the three systems is aligned to the dotted lines.

6.2.3 Electron-Phonon Coupling Symmetry Analysis

To understand the short carrier lifetimes in the layered structures, we analyze the contribution of each phonon mode to the scattering rates. This can be done by understanding the rate of change of τ^{-1} with respect to the phonon frequencies ω, that is, $\partial\tau^{-1}/\partial\omega$. The spectral decomposition shown in Figure 6.8 reveals that high-frequency optical modes are the main contributors to the charge carrier scattering. In contrast, acoustic and low-frequency optical modes show negligible contributions to the scattering rates. In the case of $n = 1$, the scattering rate is dominated by longitudinal-optical (LO) phonons around 113 cm^{-1} and 121 cm^{-1} which are related to Pb-Br stretching vibrations (Peaks 1 & 2). The Pb-Br stretching mode is decomposed into in-plane and out-of-plane contributions, due to the symmetry breaking along the stacking direction. Symmetry analysis at the Γ-point for the Peak 1 mode reveals that the Pb-Br stretching mode is related to the E_u irreducible representation, which is infrared-active and is also the dipole term of the D_{4h} point-group along the x and y cartesian directions. This type of polar distortion of the lattice can give rise to an electric field along the in-plane direction which can scatter the charge carriers, which is known as Fröhlich-like interaction. Analogously, the Pb-Br stretching mode of Peak 2 is related to the A_{2u} representation, which is infrared-active and is also a dipole term of the D_{4h} point-group, but related to the z cartesian direction.

For $n = 2$, the scattering rate is also dominated by LO phonons associated with a similar Pb-Br stretching mode contribution (Peak 4) around 129 cm^{-1} and Pb-Br-Pb bending modes both in- and out-of-plane (Peak 3) around 121 cm^{-1}. Symmetry analysis at the Γ-point for Peak 4 shows that the stretching mode is associated with the A_1 representation which is both infrared- and Raman-active, and is the dipole term of the C_{4v} point-group along the z cartesian direction. This analysis shows that, as for the $n = 1$ system, the Peak 4 observed for the $n = 2$ system has the same physical origin, which is related to Fröhlich coupling. However, the symmetry analysis for the Peak 3 modes shows that the Pb-Br-Pb bending modes are associated with the B_1 irreducible representation, which is Raman-active, but do not contain any dipole term of the C_{4v} point-group. As so it can not give rise to a scattering electric field as it would be the case for a Fröhlich-like type of interaction. We associate the scattering mechanism of Peak 3 with a non-polar optical deformation potential scattering. This type of scattering arises from the fact that the atomic displacements can be described by long-wavelength acoustic waves. These form elastic strains in the crystal that can lead to scattering of charge carriers. This can be seen by taking the $q = 0$ and the intra-band scattering limit case for the electron-phonon matrix elements $g_{nm\nu}(\mathbf{k},\mathbf{q})$ discussed in Chapter 2.4, that is, $g_{nn\nu}(\mathbf{k},0) = \langle u_{n\mathbf{k}}|\Delta_{0\nu}v_{SCF}|u_{n\mathbf{k}}\rangle_{uc}$. By analyzing the coupling between the phonon modes with irreducible representation B_1 with the charge carri-

ers with irreducible representation E, we see that the transition matrices $\langle u_{n\mathbf{k}}|\Delta_{0v}v_{SCF}|u_{n\mathbf{k}}\rangle_{uc}$ always contain the initial electronic state E, which satisfies the selection rule for the deformation potential coupling [189]. Therefore, the non-polar optical deformation potential coupling between the Pb-Br-Pb bending modes with the charge carriers is allowed by symmetry and contributes to the charge carrier scattering.

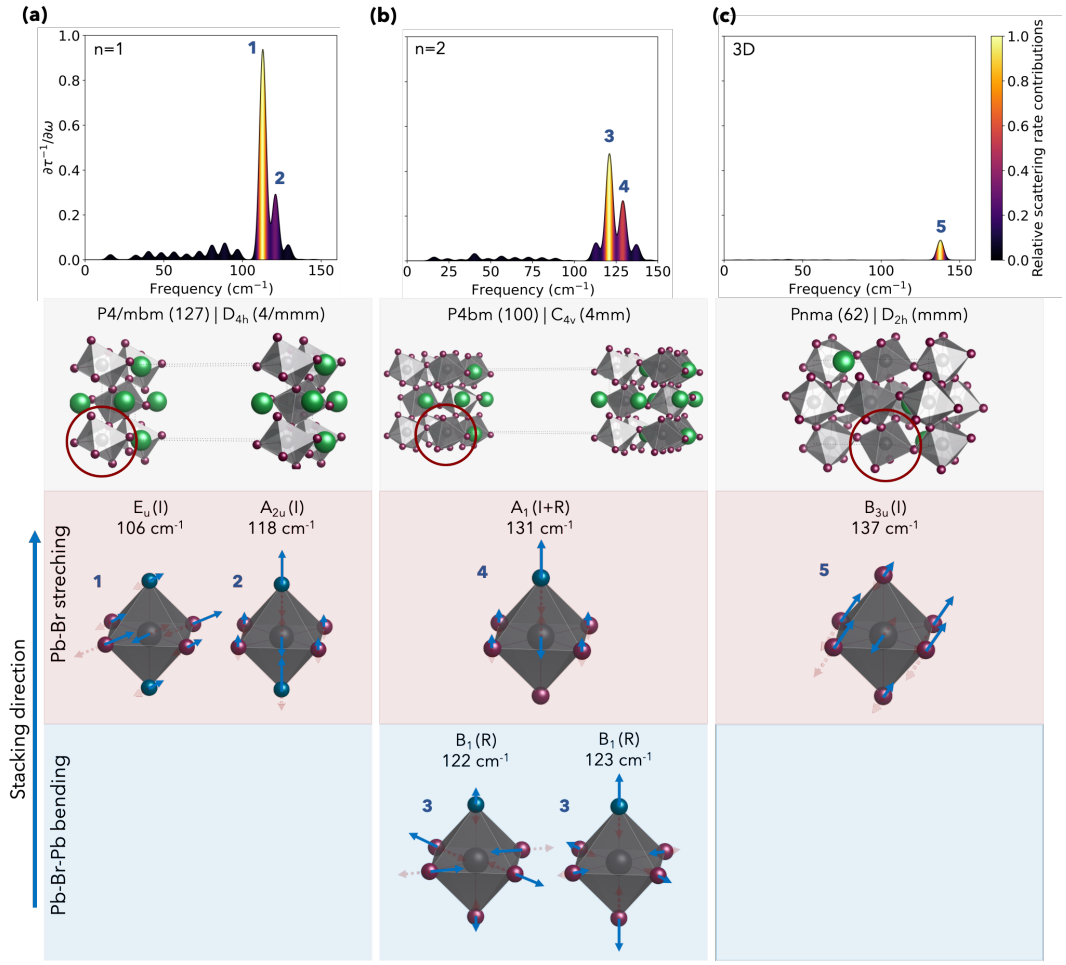

Figure 6.8 – Normalized spectral decomposition of the contribution of phonons with energy $\hbar\omega$ to the scattering rates τ^{-1} for (a) $n = 1$, (b) $n = 2$ and (c) three-dimensional structures. A representation of the vibration modes related to the red-circled octahedra is also shown. The atoms in blue represent the apical halogens, i.e. that are not connected along the stacking direction. The gray boxes below each system indicate each system's space group and Γ-point point groups. The labels *R* and *I* refer to Raman- and infrared-active, respectively.

Finally, the three-dimensional structure exhibits a sharp peak located at around 145 cm^{-1}, which also arises from the scattering via LO phonons and is related to a similar Pb-Br stretch-

ing mode as discussed for the layered systems. The symmetry analysis at the Γ-point for Peak 5 shows that the stretching mode is connected to the B_{3u} irreducible representation, which is infrared-active and contains the dipole term of the D_{2h} point-group. It is important to note that the non-polar optical deformation potential type of scattering predicted for the $n = 2$ system is not allowed either for the $n = 1$ or three-dimensional system. This analysis is consistent with previous symmetry analysis performed by Even *et al.* for three-dimensional cubic perovskites [190]. Moreover, the decomposition analysis obtained for the three-dimensional system is also consistent with previous calculations performed by Poncé *et al.* for $MAPbI_3$ [36]. This analysis reveals that even when the dimensionality is reduced, the primary source of charge carrier relaxation in perovskites is still given by polar-phonon scattering mechanisms arising from the long-range Fröhlich coupling, consistently with calculations for 3D systems such as AMX_3 perovskites [191] and also $A_2MM'X_6$ double perovskites [192]. However, for the layered systems, we also observe new scattering sources from phonon modes that originated from the lack of octahedra connectivity along the stacking direction, leading to large overall scattering rates and, consequently, lower mobilities.

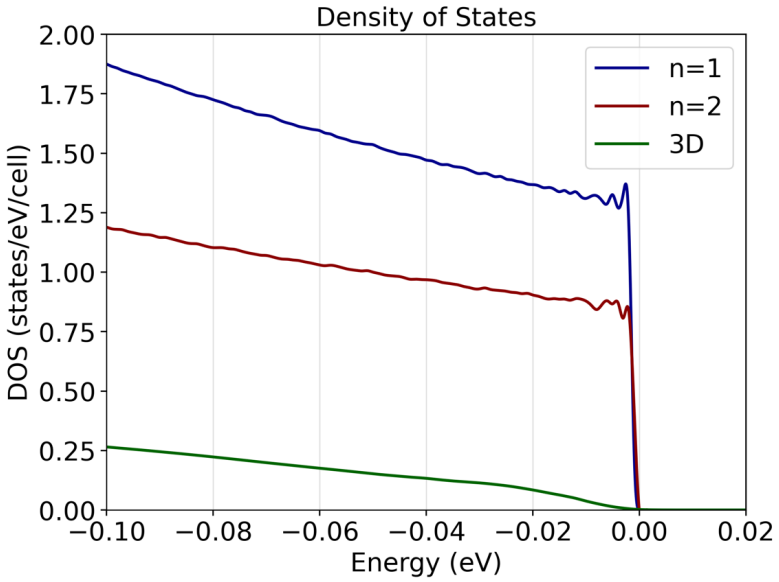

Figure 6.9 – Electronic density of states (DOS) near the valence band edge.

Within time-dependent perturbation theory, the carrier's lifetimes and scattering rates can be obtained from Fermi's Golden Rule [193]. In its simplest approximation, they are proportional to the electron-phonon coupling strength $|g_{nm\nu}(\mathbf{k},\mathbf{q})|^2$ (See Chapter 2.4) and to the electronic density of states $D(\varepsilon)$ at the vicinity of the band-edges, that is $\tau^{-1} \propto |g_{nm\nu}(\mathbf{k},\mathbf{q})|^2 D(\varepsilon)$. The

analysis of $\partial\tau^{-1}/\partial\omega$ discussed in this section provides us information on how strongly the charge carrier is coupled with the different vibration modes in the system, which is related to $|g_{nm\nu}(\mathbf{k},\mathbf{q})|^2$. Yet, differences in the density of states will also lead to differences in the scattering rates. Figure 6.9 shows the calculated electronic density of states (DOS) near the valence band edge. We show that in this region, the DOS is much larger for the layered systems than for the three-dimensional structure. That means many more charge carriers are available to be scattered close to the band-edges, which is the region being populated and contributing to the charge carriers' mobility at room temperature. It can be shown that, as the number of octahedra layers n increases, the DOS of the layered systems decreases and converges to the three-dimensional limit where $D(\varepsilon) \propto \sqrt{\varepsilon}$ [194]. Hence, the mobility of the layered systems is reduced not only by the larger scattering rates coming from the polar-phonon scattering but also by the increased DOS close to the band edges.

Take-home Messages

- The charge carrier mobility decrease observed when going from the layered systems to three-dimensional systems is primarily originated from differences in the carrier's lifetimes.
- We show that as for three-dimensional perovskites, the primary source of charge carrier relaxation in layered perovskites is given by polar-phonon scattering mechanisms arising from the long-range Fröhlich coupling. Yet due to the lack of octahedra connectivity along the stacking direction, we observe new modes and different electron-phonon coupling mechanisms contributing to charge carrier scattering, leading to reduced mobilities.
- We show that the mobilities are not only reduced by the increased polar-phonon scattering mechanisms but also from the much larger DOS in the vicinity of the band-edges.

A manuscript related to this work is under preparation.

CHAPTER 7

CONCLUSIONS & PERSPECTIVES

The investigations and results presented in the previous chapters have collectively advanced our understanding of the relationship between structural, electronic, and optical properties for a set of materials materials beyond conventional perovskites. By performing state-of-art ab initio calculations, we were able to offer insights on the applicability of each of these materials for optoelectronics and addressed several of the challenges that were discussed in the introductory chapter, such as stability, materials toxicity, device performance, and fundamental physics/chemistry of perovskites. Via symmetry-based models, Ag/Bi double salts were identified as potential lead-free solar-cell absorbers, offering good stability, optoelectronic properties, and high theoretical power conversion efficiencies. On the other hand, lead-free VODP were shown to be stable materials that exhibit poor photovoltaic properties in comparison to conventional perovskites. Yet, they show potential to be great light-emitters and platforms to study fundamental exciton physics. Lead-free layered materials were shown to exhibit tunable optoelectronic properties while maintaining stability. More importantly, the models developed for layered compounds were employed to perform high-level transport calculations and elucidate the origin of low charge carrier mobilities in comparison to three-dimensional perovskites.

More specifically, in the first result chapter of this thesis, we elucidated the interplay between structural and electronic properties of a prominent family of lead-free halide perovskite-like materials for optoelectronics. A symmetry-based modeling approach was introduced, allowing us to align theoretical predictions with empirical observations and provide important insights into the application of these materials in photovoltaics. This investigation underscored the importance of adopting an approach that can appropriately describe the atomic positions in the crystal lattice and the role of each atomic species on the electronic and optical properties of Ag/Bi double salts. Our findings support the application of $AgBiI_4$ as a potential solar-cell absorber due to its small and tunable band gap, light effective masses, large absorption coefficient, and high theoretical power conversion efficiency. Moreover, we demonstrated that the current devices based on the Ag/Bi double salts are mainly limited by low V_{oc}, which indicates that optimizing electron/hole transport layers and their interfaces could significantly improve

solar-cell performances.

In the second result chapter, we investigated a family of lead-free halide perovskite materials that drew considerable attention from the community due to their potential applications for optoelectronics. By investigating the role of the non-corner-sharing MX_6 octahedra we unveiled interesting properties of the VODP such as tunable vacant site sizes and tunable conduction band splittings, as supported by crystal field theory. We identified Te-based materials as candidates for hole transport and Sn-based materials for electron transport layers, which are essential building blocks for efficient photovoltaic devices. Moreover, we proposed Cs_2ZrI_6 as a new stable material that exhibits one of the smallest band-gaps and charge carrier effective masses within the VODP family. Finally, this chapter culminated in the description of the electron-hole interactions in these materials. We demonstrated that due to the large and/or indirect electronic band-gaps, heavy effective masses of charge carriers, and especially, the strong electron-hole coupling, these materials cannot be suitable alternatives to lead-free photovoltaic devices. However, they present great opportunities for light-emission and quantum optical technologies due to their tunable dark-bright splittings and exciton binding energies, which leads these materials to exhibit both Wannier-type and Frenkel-type excitons.

In the following chapter, about layered halide double perovskites, we entered into the domain of layered perovskites, the two-dimensional analogs of AMX_3 perovskites. Via the development of a series of structural models, we were able to investigate the role of octahedra tilting and distortions on the structural and electronic properties of layered systems in comparison to the three-dimensional bulk case. In collaboration with experimental partners, three new layered halide perovskites were synthesized. We showed that our models are capable of describing qualitatively the electronic properties of the synthesized systems and demonstrate the possibility of hosting interlayer interactions, which can have impacts on the optical properties of the layered systems. Furthermore, the simplicity of our structural models allowed us to pursue higher-level calculations, which would not be achievable by considering the reported experimental structures as a basis for computational simulations.

In the final results chapter, we unified the knowledge acquired throughout this thesis and unveiled the origin of low charge carrier mobilities in layered perovskites in comparison to the bulk case. We demonstrated that as for the bulk systems, the long-range Fröhlich interaction is the primary source of charge carrier scattering in layered perovskites. Furthermore, we showed that due to the lack of octahedra connectivity along the stacking direction for the layered systems, new phonon modes and different electron-phonon coupling mechanisms arise and contribute to charge carrier scattering, leading to reduced mobilities in layered systems. In

addition, we also demonstrate that layered perovskites exhibit an increased electronic density of states close to the band edges, which also contributes to the increased scattering rates and lower charge carrier mobilities.

For future perspectives, much could be done in the framework of any of these chapters. Going into specifics, for the Ag/Bi double salts, an interesting route could be employing our symmetry-based models to investigate substitutional engineering and explore other double salt families, such as Ag/In double salts. For the VODP, one could take a step further from electron-hole interactions to investigate the interaction of excitons with the crystal lattice, which is the origin of the self-trapped excitonic states discussed previously. More broadly speaking I believe there is still plenty of future for halide-based perovskite materials, and we demonstrated that computational material science can be a powerful tool for modeling them. Based only on computational modeling we were able to tackle several open challenges towards the commercialization of these technologies, and also work closely with experimentalists. We hope the methodologies, codes, and calculations done in this thesis will pave the way to more efficient and stable optoelectronic devices based on lead-free perovskites and perovskite-like materials.

Bibliography

1. Rose, G., Beschreibung einiger neuen Mineralien des Urals, *Ann. Phys.* **124,** 551–573 (1839).
2. *Mindat.org - Hudson Institute of Mineralogy* `https://www.mindat.org/photo-155026.html`, 2008.
3. Bednorz, J. G. & Müller, K. A., Possible high T c superconductivity in the Ba- La- Cu- O system, *Z. Phys. B Cond. Matt.* **64,** 189–193 (1986).
4. Levy, P. M., Giant magnetoresistance in magnetic layered and granular materials, *Science* **256,** 972–973 (1992).
5. Kim, H. J. *et al.,* High Mobility in a Stable Transparent Perovskite Oxide, *Appl. Phys. Express* **5,** 061102 (2012).
6. Luo, X. *et al.,* High carrier mobility in transparent Ba1xLaxSnO3 crystals with a wide band gap, *Appl. Phys. Lett.* **100,** 172112 (2012).
7. Filip, M. R. & Giustino, F., The geometric blueprint of perovskites, *Proc. Natl. Acad. Sci. U.S.A.* **115,** 5397–5402 (2018).
8. Volonakis, G., Sakai, N., Snaith, H. J. & Giustino, F., Oxide Analogs of Halide Perovskites and the New Semiconductor Ba2AgIO6, *J. Phys. Chem. Lett.* **10,** 1722–1728 (2019).
9. Wells, H. L., Über die cäsium-und kalium-bleihalogenide, *Z. Anorg. Allg. Chem.* **3,** 195–210 (1893).
10. Marronnier, A. *et al.,* Anharmonicity and Disorder in the Black Phases of Cesium Lead Iodide Used for Stable Inorganic Perovskite Solar Cells, *ACS Nano* **12,** 3477–3486 (2018).
11. Zacharias, M., Volonakis, G., Giustino, F. & Even, J., Anharmonic lattice dynamics via the special displacement method, *Phys. Rev. B* **108,** 035155 (2023).
12. Kojima, A., Teshima, K., Shirai, Y. & Miyasaka, T., Organometal Halide Perovskites as Visible-Light Sensitizers for Photovoltaic Cells, *J. Am. Chem. Soc.* **131,** 6050–6051 (2009).
13. Turren-Cruz, S.-H., Hagfeldt, A. & Saliba, M., Methylammonium-free, high-performance, and stable perovskite solar cells on a planar architecture, *Science* **362,** 449–453 (2018).

14. Stoumpos, C. C., Malliakas, C. D. & Kanatzidis, M. G., Semiconducting tin and lead iodide perovskites with organic cations: phase transitions, high mobilities, and near-infrared photoluminescent properties, *Inorg. Chem.* **52,** 9019–9038 (2013).

15. Saliba, M. *et al.,* Cesium-containing triple cation perovskite solar cells: improved stability, reproducibility and high efficiency, *Energy Environ. Sci.* **9,** 1989–1997 (2016).

16. Tsai, H. *et al.,* High-efficiency two-dimensional Ruddlesden–Popper perovskite solar cells, *Nature* **536,** 312–316 (2016).

17. Chen, Y. *et al.,* 2D Ruddlesden–Popper Perovskites for Optoelectronics, *Adv. Mater.* **30,** 1703487 (2018).

18. Katan, C., Mercier, N. & Even, J., Quantum and Dielectric Confinement Effects in Lower-Dimensional Hybrid Perovskite Semiconductors, *Chem. Rev.* **119,** 3140–3192 (2019).

19. Pedesseau, L. *et al.,* Advances and Promises of Layered Halide Hybrid Perovskite Semiconductors, *ACS Nano* **10,** 9776–9786 (2016).

20. Li, X., Hoffman, J. M. & Kanatzidis, M. G., The 2D Halide Perovskite Rulebook: How the Spacer Influences Everything from the Structure to Optoelectronic Device Efficiency, *Chem. Rev.* **121,** 2230–2291 (2021).

21. Saparov, B. & Mitzi, D. B., Organic–Inorganic Perovskites: Structural Versatility for Functional Materials Design, *Chem. Rev.* **116,** 4558–4596 (2016).

22. Zheng, Y. *et al.,* Unique characteristics of 2D Ruddlesden–Popper (2DRP) perovskite for future photovoltaic application, *J. Mater. Chem. A* **7,** 13860–13872 (2019).

23. Byeon, J. *et al.,* Structural Isomer of Fluorinated Ruddlesden-Popper Perovskites Toward Efficient and Stable 2D/3D Perovskite Solar Cells, *ACS Appl. Mater. Interfaces* **15,** 27853–27864 (2023).

24. Volonakis, G. *et al.,* Lead-Free Halide Double Perovskites via Heterovalent Substitution of Noble Metals, *J. Phys. Chem. Lett.* **7,** 1254–1259 (2016).

25. Volonakis, G. *et al.,* Cs2InAgCl6: A New Lead-Free Halide Double Perovskite with Direct Band Gap, *J. Phys. Chem. Lett.* **8,** 772–778 (2017).

26. Filip, M. R., Hillman, S., Haghighirad, A. A., Snaith, H. J. & Giustino, F., Band Gaps of the Lead-Free Halide Double Perovskites Cs2BiAgCl6 and Cs2BiAgBr6 from Theory and Experiment, *J. Phys. Chem. Lett.* **7,** 2579–2585 (2016).

27. García-Espejo, G., Rodríguez-Padrón, D., Luque, R., Camacho, L. & de Miguel, G., Mechanochemical synthesis of three double perovskites: Cs2AgBiBr6, (CH3NH3)2TlBiBr6 and Cs2AgSbBr6, *Nanoscale* **11,** 16650–16657 (2019).

28. Vargas, B., Rodrıguez-López, G. & Solis-Ibarra, D., The Emergence of Halide Layered Double Perovskites, *ACS Energy Lett.* **5,** 3591–3608 (2020).

29. Lee, B. *et al.,* Air-Stable Molecular Semiconducting Iodosalts for Solar Cell Applications: Cs2SnI6 as a Hole Conductor, *J. Am. Chem. Soc.* **136,** 15379–15385 (2014).

30. Turkevych, I. *et al.,* Photovoltaic Rudorffites: Lead-Free Silver Bismuth Halides Alternative to Hybrid Lead Halide Perovskites, *ChemSusChem* **10,** 3754–3759 (2017).

31. D'innocenzo, V. *et al.,* Excitons versus free charges in organo-lead tri-halide perovskites, *Nature Comm.* **5,** 3586 (2014).

32. Schulz, P. *et al.,* Interface energetics in organo-metal halide perovskite-based photovoltaic cells, *Energy Environ. Sci.* **7,** 1377–1381 (2014).

33. Protesescu, L. *et al.,* Nanocrystals of Cesium Lead Halide Perovskites (CsPbX3, X = Cl, Br, and I): Novel Optoelectronic Materials Showing Bright Emission with Wide Color Gamut, *Nano Lett.* **15,** 3692–3696 (2015).

34. Even, J., Pedesseau, L., Jancu, J.-M. & Katan, C., Importance of Spin–Orbit Coupling in Hybrid Organic/Inorganic Perovskites for Photovoltaic Applications, *J. Phys. Chem. Lett.* **4,** 2999–3005 (2013).

35. Kepenekian, M. *et al.,* Rashba and Dresselhaus Effects in Hybrid Organic–Inorganic Perovskites: From Basics to Devices, *ACS Nano* **9,** 11557–11567 (2015).

36. Poncé, S., Schlipf, M. & Giustino, F., Origin of Low Carrier Mobilities in Halide Perovskites, *ACS Energy Lett.* **4,** 456–463 (2019).

37. Edri, E. *et al.,* Elucidating the charge carrier separation and working mechanism of CH3NH3PbI3- x Cl x perovskite solar cells, *Nat. Comm.* **5,** 3461 (2014).

38. Filip, M. R., Verdi, C. & Giustino, F., GW Band Structures and Carrier Effective Masses of CH3NH3PbI3 and Hypothetical Perovskites of the Type APbI3: A = NH4, PH4, AsH4, and SbH4, *J. Phys. Chem. C* **119,** 25209–25219 (2015).

39. Leguy, A. M. A. *et al.,* Experimental and theoretical optical properties of methylammonium lead halide perovskites, *Nanoscale* **8,** 6317–6327 (2016).

40. Fabini, D. H., Seshadri, R. & Kanatzidis, M. G., The underappreciated lone pair in halide perovskites underpins their unusual properties, *MRS Bulletin* **45,** 467–477 (2020).

41. Stranks, S. D. & Snaith, H. J., Metal-Halide Perovskites for Photovoltaic and Light-Emitting Devices, *Nat. Nanotechnol.* **10,** 391–402 (2015).

42. Cui, J. *et al.,* Efficient Light-Emitting Diodes Based on Oriented Perovskite Nanoplatelets, *Sci. Adv.* **7,** eabg8458 (2021).

43. Zhang, Z. *et al.,* Stable and Highly Efficient Photocatalysis with Lead-Free Double-Perovskite of $Cs_2AgBiBr_6$, *Angew. Chem. Int. Ed.* **58,** 7263–7267 (2019).

44. Fehr, A. M. *et al.,* Integrated halide perovskite photoelectrochemical cells with solar-driven water-splitting efficiency of 20.8%, *Nature Comm.* **14,** 3797 (2023).

45. Tian, W., Zhou, H. & Li, L., Hybrid organic–inorganic perovskite photodetectors, *Small* **13,** 1702107 (2017).

46. Wu, H., Ge, Y., Niu, G. & Tang, J., Metal Halide Perovskites for X-Ray Detection and Imaging, *Matter* **4,** 144–163 (2021).

47. Xing, G. *et al.,* Long-Range Balanced Electron- and Hole-Transport Lengths in Organic-Inorganic $CH_3NH_3PbI_3$, *Science* **342,** 344–347 (2013).

48. Waser, R., Dittmann, R., Staikov, G. & Szot, K., Redox-Based Resistive Switching Memories-Nanoionic Mechanisms, Prospects, and Challenges, *Adv. Mater.* **21,** 2632–2663 (2009).

49. Reyren, N. *et al.,* Superconducting Interfaces Between Insulating Oxides, *Science* **317,** 1196–1199 (2007).

50. Lee, M. M., Teuscher, J., Miyasaka, T., Murakami, T. N. & Snaith, H. J., Efficient Hybrid Solar Cells Based on Meso-Superstructured Organometal Halide Perovskites, *Science* **338,** 643–647 (2012).

51. Ball, J. M., Lee, M. M., Hey, A. & Snaith, H. J., Low-temperature processed meso-superstructured to thin-film perovskite solar cells, *Energy Environ. Sci.* **6,** 1739–1743 (2013).

52. Eperon, G. E., Burlakov, V. M., Docampo, P., Goriely, A. & Snaith, H. J., Morphological Control for High Performance, Solution-Processed Planar Heterojunction Perovskite Solar Cells, *Adv. Funct. Mater.* **24,** 151–157 (2014).

53. Burschka, J. *et al.,* Sequential deposition as a route to high-performance perovskite-sensitized solar cells, *Nature* **499,** 316–319 (2013).

54. *Best Research-Cell Efficiencies* http://www.nrel.gov/, 2023.

55. Herz, L. M., Charge-Carrier Mobilities in Metal Halide Perovskites: Fundamental Mechanisms and Limits, *ACS Energy Lett.* **2,** 1539–1548 (2017).

56. Kim, Y. *et al.,* Pure Cubic-Phase Hybrid Iodobismuthates AgBi2I7 for Thin-Film Photovoltaics, *Angew. Chem. Int. Ed.* **55,** 9586–9590 (2016).

57. Khazaee, M. *et al.,* Dual-source evaporation of silver bismuth iodide films for planar junction solar cells, *J. Mater. Chem. A* **7,** 2095–2105 (2019).

58. Eperon, G. E. *et al.,* Perovskite-perovskite tandem photovoltaics with optimized band gaps, *Science* **354,** 861–865 (2016).

59. Tan, Z.-K. *et al.,* Bright light-emitting diodes based on organometal halide perovskite, *Nat. Nanotechnol.* **9,** 687–692 (2014).

60. Zhang, Z. *et al.,* Efficient deep-blue luminescence based on dual-channel intra/intermolecular exciplexes, *Sci. Adv.* **9,** eadf4060 (2023).

61. Lin, K. *et al.,* Perovskite light-emitting diodes with external quantum efficiency exceeding 20 per cent, *Nature* **562,** 245–248 (2018).

62. Chiba, T. *et al.,* Anion-exchange red perovskite quantum dots with ammonium iodine salts for highly efficient light-emitting devices, *Nat. Photonics* **12,** 681–687 (2018).

63. Cao, Y. *et al.,* Perovskite light-emitting diodes based on spontaneously formed submicrometre-scale structures, *Nature* **562,** 249–253 (2018).

64. Pacchioni, G., Highly efficient perovskite LEDs, *Nat. Rev. Mater.* **6,** 108–108 (2021).

65. Ma, D. *et al.,* Distribution control enables efficient reduced-dimensional perovskite LEDs, *Nature* **599,** 594–598 (2021).

66. Pereyra, C., Xie, H. & Lira-Cantu, M., Additive engineering for stable halide perovskite solar cells, *J. Energy Chem.* **60,** 599–634 (2021).

67. Nie, W. *et al.,* Critical Role of Interface and Crystallinity on the Performance and Photostability of Perovskite Solar Cell on Nickel Oxide, *Adv. Mater.* **30,** 1703879 (2018).

68. Li, J. *et al.,* Encapsulation of perovskite solar cells for enhanced stability: Structures, materials and characterization, *J. Power Sources* **485,** 229313 (2021).

69. Babayigit, A., Ethirajan, A., Muller, M. & Conings, B., Toxicity of organometal halide perovskite solar cells, *Nat. Materials* **15,** 247–251 (2016).

70. Giustino, F. & Snaith, H. J., Toward Lead-Free Perovskite Solar Cells, *ACS Energy Lett.* **1,** 1233–1240 (2016).

71. Blancon, J.-C. *et al.,* Scaling law for excitons in 2D perovskite quantum wells, *Nature Comm.* **9,** 2254 (2018).

72. Zeng, R. *et al.,* Boosting triplet self-trapped exciton emission in Te (IV)-doped Cs 2 SnCl 6 perovskite variants, *Nano Res.* **14,** 1551–1558 (2021).

73. Miyata, K. *et al.,* Large polarons in lead halide perovskites, *Sci. Adv.* **3,** e1701217 (2017).

74. Liu, S. *et al.,* Colloidal Synthesis and Tunable Multicolor Emission of Vacancy-Ordered Cs2HfCl6 Perovskite Nanocrystals, *Laser Photonics Rev.* **16,** 2100439 (2022).

75. Mao, L. *et al.,* Structural Diversity in White-Light-Emitting Hybrid Lead Bromide Perovskites, *J. Am. Chem. Soc.* **140,** 13078–13088 (2018).

76. Zhang, J. L. *et al.,* Epitaxial Growth of Single Layer Blue Phosphorus: A New Phase of Two-Dimensional Phosphorus, *Nano Lett.* **16,** 4903–4908 (2016).

77. Zhu, Z. Y., Cheng, Y. C. & Schwingenschlögl, U., Giant spin-orbit-induced spin splitting in two-dimensional transition-metal dichalcogenide semiconductors, *Phys. Rev. B* **84,** 153402 (2011).

78. Tang, Q., Zhou, Z. & Shen, P., Are MXenes Promising Anode Materials for Li Ion Batteries? Computational Studies on Electronic Properties and Li Storage Capability of Ti3C2 and Ti3C2X2 (X = F, OH) Monolayer, *J. Am. Chem. Soc.* **134,** 16909–16916 (2012).

79. Kuèhnle, A., Linderoth, T. R., Hammer, B. & Besenbacher, F., Chiral recognition in dimerization of adsorbed cysteine observed by scanning tunnelling microscopy, *Nature* **415,** 891–893 (2002).

80. Meng, J., *Relativistic density functional for nuclear structure* (World Scientific, 2016).

81. Hohenberg, P. & Kohn, W., Inhomogeneous Electron Gas, *Phys. Rev.* **136,** B864–B871 (1964).

82. Born, M. & Oppenheimer, R., *in Quantum Chemistry: Classic Scientific Papers* 1–24 (World Scientific, 2000).

83. Parr, R. G., *Density functional theory of atoms and molecules in Horizons of Quantum Chemistry: Proceedings of the Third International Congress of Quantum Chemistry Held at Kyoto, Japan, October 29-November 3, 1979* (1980), 5–15.

84. Perdew, J. P., Burke, K. & Ernzerhof, M., Generalized Gradient Approximation Made Simple, *Phys. Rev. Lett.* **77,** 3865–3868 (1996).

85. Haas, P., Tran, F. & Blaha, P., Calculation of the lattice constant of solids with semilocal functionals, *Phys. Rev. B* **79,** 085104 (2009).

86. Sun, J., Ruzsinszky, A. & Perdew, J. P., Strongly Constrained and Appropriately Normed Semilocal Density Functional, *Phys. Rev. Lett.* **115,** 036402 (2015).

87. Heyd, J., Scuseria, G. E. & Ernzerhof, M., Hybrid functionals based on a screened Coulomb potential, *J. Chem. Phys.* **118,** 8207–8215 (2003).

88. Ceperley, D. M. & Alder, B. J., Ground State of the Electron Gas by a Stochastic Method, *Phys. Rev. Lett.* **45,** 566–569 (1980).

89. Dick, S. & Fernandez-Serra, M., Machine learning accurate exchange and correlation functionals of the electronic density, *Nature Comm.* **11,** 3509 (2020).

90. Pickett, W. E., Pseudopotential methods in condensed matter applications, *Comput. Phys. Rep.* **9,** 115–197 (1989).

91. Ghosh, K., Ma, H., Gavini, V. & Galli, G., All-electron density functional calculations for electron and nuclear spin interactions in molecules and solids, *Phys. Rev. Mater.* **3,** 043801 (2019).

92. Kresse, G. & Furthmüller, J., Efficient iterative schemes for ab initio total-energy calculations using a plane-wave basis set, *Phys. Rev. B* **54,** 11169 (1996).

93. Towler, M. D., Zupan, A. & Causà, M., Density functional theory in periodic systems using local Gaussian basis sets, *Comput. Phys. Commun.* **98,** 181–205 (1996).

94. Enkovaara, J. *et al.,* Electronic structure calculations with GPAW: a real-space implementation of the projector augmented-wave method, *J. Condens. Matter Phys.* **22,** 253202 (2010).

95. Perdew, J. P., Parr, R. G., Levy, M. & Balduz, J. L., Density-Functional Theory for Fractional Particle Number: Derivative Discontinuities of the Energy, *Phys. Rev. Lett.* **49,** 1691–1694 (1982).

96. Borlido, P. *et al.,* Exchange-correlation functionals for band gaps of solids: benchmark, reparametrization and machine learning, *Npj Comput. Mater.* **6,** 96 (2020).

97. Hedin, L., On correlation effects in electron spectroscopies and the GW approximation, *J. Condens. Matter Phys.* **11,** R489 (1999).

98. Biswas, T. & Singh, A. K., Excitonic effects in absorption spectra of carbon dioxide reduction photocatalysts, *Npj Comput. Mater.* **7,** 189 (2021).

99. Caruso, F., Filip, M. R. & Giustino, F., Excitons in one-dimensional van der Waals materials: Sb 2 S 3 nanoribbons, *Phys. Rev. B* **92,** 125134 (2015).

100. Kamminga, M. E. *et al.,* Confinement Effects in Low-Dimensional Lead Iodide Perovskite Hybrids, *Chem. Mater.* **28,** 4554–4562 (2016).

101. Hüser, F., Olsen, T. & Thygesen, K. S., Quasiparticle GW calculations for solids, molecules, and two-dimensional materials, *Phys. Rev. B* **87,** 235132 (2013).

102. Mueller, T. & Malic, E., Exciton physics and device application of two-dimensional transition metal dichalcogenide semiconductors, *NPJ 2D Mater. Appl.* **2,** 29 (2018).

103. Zhang, X.-X. *et al.,* Magnetic brightening and control of dark excitons in monolayer WSe2, *Nat. Nanotechnol.* **12,** 883–888 (2017).

104. Salpeter, E. E. & Bethe, H. A., A Relativistic Equation for Bound-State Problems, *Phys. Rev.* **84,** 1232–1242 (1951).

105. Giustino, F., Electron-phonon interactions from first principles, *Rev. Mod. Phys.* **89,** 015003 (2017).

106. Maradudin, A. A. & Vosko, S. H., Symmetry Properties of the Normal Vibrations of a Crystal, *Rev. Mod. Phys.* **40,** 1–37 (1968).

107. Poncé, S., Li, W., Reichardt, S. & Giustino, F., First-principles calculations of charge carrier mobility and conductivity in bulk semiconductors and two-dimensional materials, *Rep. Prog. Phys.* **83,** 036501 (2020).

108. Baroni, S., de Gironcoli, S., Dal Corso, A. & Giannozzi, P., Phonons and related crystal properties from density-functional perturbation theory, *Rev. Mod. Phys.* **73,** 515–562 (2001).

109. Wannier, G. H., Dynamics of band electrons in electric and magnetic fields, *Rev. Mod. Phys.* **34,** 645 (1962).

110. Sporkmann, B. & Bross, H., Calculation of Wannier functions for fcc transition metals by Fourier transformation of Bloch functions, *Phys. Rev. B* **49,** 10869 (1994).

111. Sporkmann, B. & Bross, H., Calculation of Wannier functions for zinc-blende-type semiconductors, *J. Condens. Matter Phys.* **9,** 5593 (1997).

112. Marzari, N., Mostofi, A. A., Yates, J. R., Souza, I. & Vanderbilt, D., Maximally localized Wannier functions: Theory and applications, *Rev. Mod. Phys.* **84,** 1419–1475 (2012).

113. Mostofi, A. A. *et al.,* An Updated Version of Wannier90: A Tool for Obtaining Maximally-Localised Wannier Functions, *Comput. Phys. Commun.* **185,** 2309–2310 (2014).

114. Wu, Q., Zhang, S., Song, H.-F., Troyer, M. & Soluyanov, A. A., WannierTools : An Open-Source Software Package for Novel Topological Materials, *Comput. Phys. Commun.* **224,** 405–416 (2018).

115. Sangalli, D. *et al.,* Many-Body Perturbation Theory Calculations Using the Yambo Code, *J. Phys. Condens. Matter.* **31,** 325902 (2019).

116. Poncé, S., Margine, E., Verdi, C. & Giustino, F., EPW: Electron–phonon coupling, transport and superconducting properties using maximally localized Wannier functions, *Comput. Phys. Commun.* **209,** 116–133 (2016).

117. Shockley, W. & Queisser, H. J., Detailed Balance Limit of Efficiency of p-n Junction Solar Cells, *J. Appl. Phys.* **32,** 510–519 (1961).

118. Yu, L. & Zunger, A., Identification of Potential Photovoltaic Absorbers Based on First-Principles Spectroscopic Screening of Materials, *Phys. Rev. Lett.* **108,** 068701 (2012).

119. Tiedje, T., Yablonovitch, E., Cody, G. & Brooks, B., *IEEE Trans. Electron Dev.* **31,** 711–716 (1984).

120. Wang, L. *et al.,* Revealing the Potential Crystal Structures of Earth-Abundant Nontoxic Photovoltaic CuBiI4, *Cryst. Growth Des.* **21,** 2850–2855 (2021).

121. Rüdorff, W. & Becker, H., Die Strukturen von $LiV0_2$, $NaVO_2$, $LiCrO_2$ und $NaCr0_2$, *Z. Naturforsch. B* **9,** 614–615 (1954).

122. Danilović, D. *et al.,* Aerosol Synthesis and Gas-Phase Photoelectron Spectroscopy of Ag-Bi-I Nanosystems, *J. Phys. Chem. C* **124,** 23930–23937 (2020).

123. Turkevych, I., Kazaoui, S., Shirakawa, N. & Fukuda, N., Potential of AgBiI4 rudorffites for indoor photovoltaic energy harvesters in autonomous environmental nanosensors, *Jpn. J. Appl. Phys.* **60,** SCCE06 (2021).

124. Pai, N. *et al.,* Silver Bismuth Sulfoiodide Solar Cells: Tuning Optoelectronic Properties by Sulfide Modification for Enhanced Photovoltaic Performance, *Adv. Energy Mater.* **9,** 1803396 (2019).

125. Jiang, P. *et al.,* Pb-free halide perovskites for solar cells, light-emitting diodes, and photocatalysts, *APL Mater.* **10** (2022).

126. Tie, S. *et al.,* Efficient X-ray attenuation lead-free AgBi2I7 halide rudorffite alternative for sensitive and stable X-ray detection, *J. Phys. Chem. Lett.* **11,** 7939–7945 (2020).

127. Popoola, I. K., Gondal, M. A., Oloore, L. E. & Popoola, A., Inorganic antimony-based rudorffite photo-responsive electrochemical capacitor utilizing non-aqueous polyvinylpyrrolidone polymer gel electrolyte for hybrid energy harvesting and storage applications, *Mater. Sci. Eng. B* **291,** 116373 (2023).

128. Paramanik, S. & Pal, A. J., Combining negative photoconductivity and resistive switching towards in-memory logic operations, *Nanoscale* **15,** 5001–5010 (2023).

129. Xiao, Z., Meng, W., Mitzi, D. B. & Yan, Y., Crystal Structure of AgBi2I7 Thin Films, *J. Phys. Chem. Lett.* **7,** 3903–3907 (2016).

130. Sansom, H. C. *et al.,* AgBiI4 as a Lead-Free Solar Absorber with Potential Application in Photovoltaics, *Chem. Mater.* **29,** 1538–1549 (2017).

131. Cucco, B. *et al.,* Silver–Bismuth Halide Double Salts for Lead-Free Photovoltaics: Insights from Symmetry-Based Modeling, *Sol. RRL* **6,** 2200718 (2022).

132. Zunger, A., Wei, S.-H., Ferreira, L. G. & Bernard, J. E., Special quasirandom structures, *Phys. Rev. Lett.* **65,** 353–356 (1990).

133. Bellaiche, L. & Vanderbilt, D., Virtual crystal approximation revisited: Application to dielectric and piezoelectric properties of perovskites, *Phys. Rev. B* **61,** 7877–7882 (2000).

134. Wondratschek, H., Splitting of Wyckoff positions (orbits), *Mineral Petrol.* **48,** 87–96 (1993).

135. Barone, V. T., Tuttle, B. R. & Khare, S. V., Properties of AgBiI4 using high through-put DFT and machine learning methods, *J. Appl. Phys.* **131** (2022).

136. Oldag, T., Aussieker, T., Keller, H.-L., Preitschaft, C. & Pfitzner, A., Solvothermale Synthese und Bestimmung der Kristallstrukturen von AgBiI4 und Ag3BiI6, *Z. fur Anorg. Allg. Chem.* **631,** 677–682 (2005).

137. Crovetto, A. *et al.,* Parallel Evaluation of the BiI3, BiOI, and Ag3BiI6 Layered Photoabsorbers, *Chem. Mater.* **32,** 3385–3395 (2020).

138. Li, X. *et al.,* Bismuth/Silver-Based Two-Dimensional Iodide Double and One-Dimensional Bi Perovskites: Interplay between Structural and Electronic Dimensions, *Chem. Mater.* **33,** 6206–6216 (2021).

139. Wang, B. *et al.,* Chlorophyll Derivative-Sensitized TiO2 Electron Transport Layer for Record Efficiency of Cs2AgBiBr6 Double Perovskite Solar Cells, *J. Am. Chem. Soc.* **143,** 2207–2211 (2021).

140. Correa Guerrero, N. B., Guo, Z., Shibayama, N., Jena, A. K. & Miyasaka, T., A Semi-transparent Silver–Bismuth Iodide Solar Cell with Voc above 0.8 V for Indoor Photovoltaics, *ACS Appl. Energy Mater.* **0,** null (0).

141. Chen, M. *et al.,* Cesium Titanium(IV) Bromide Thin Films Based Stable Lead-free Perovskite Solar Cells, *Joule* **2,** 558–570 (2018).

142. Abfalterer, A. *et al.,* Colloidal Synthesis and Optical Properties of Perovskite-Inspired Cesium Zirconium Halide Nanocrystals, *ACS Mat. Lett.* **2,** 1644–1652 (2020).

143. Zhang, F. *et al.,* Highly stable vacancy-ordered double perovskite Rb2ZrCl6 with broadband emission for down-conversion white light-emitting diodes, *J. Lumin.* **251,** 119150 (2022).

144. Maughan, A. E. *et al.,* Defect Tolerance to Intolerance in the Vacancy-Ordered Double Perovskite Semiconductors Cs2SnI6 and Cs2TeI6, *J. Am. Chem. Soc.* **138,** 8453–8464 (2016).

145. Sakai, N. *et al.,* Solution-Processed Cesium Hexabromopalladate(IV), Cs2PdBr6, for Optoelectronic Applications, *J. Am. Chem. Soc.* **139,** 6030–6033 (2017).

146. Evans, H. A. *et al.,* Hydrogen Bonding Controls the Structural Evolution in Perovskite-Related Hybrid Platinum(IV) Iodides, *Inorg. Chem.* **57,** 10375–10382 (2018).

147. Low temperature luminescence spectra of the d10s2 complexes Cs2MX6 (M = Se, Te and X = Cl, Br). The Jahn—Teller effect in the $\Gamma_4(^3T_{1u})$ excited state, *Chem. Phys.* **47,** 235–244 (1980).

148. Day, P., Spectra and Constitution of Antimony(III) Antimony(V) Hexahalide Salts and Related Compounds, *Inorg. Chem.* **2,** 452–456 (1963).

149. Laubengayer, A. W., Billings, O. B. & Newkirk, A. E., Chlorogermanic Acid and the Chlorogermanates. Properties and Crystal Structure of Cesium Hexachlorogermanate, *J. Am. Chem. Soc.* **62,** 546–548 (1940).

150. Qiu, X. *et al.,* From unstable CsSnI3 to air-stable Cs2SnI6: A lead-free perovskite solar cell light absorber with bandgap of 1.48eV and high absorption coefficient, *Sol. Energy Mater Sol.* **159,** 227–234 (2017).

151. Ju, M.-G. *et al.,* Earth-Abundant Nontoxic Titanium(IV)-based Vacancy-Ordered Double Perovskite Halides with Tunable 1.0 to 1.8 eV Bandgaps for Photovoltaic Applications, *ACS Energy Lett.* **3,** 297–304 (2018).

152. Euvrard, J., Wang, X., Li, T., Yan, Y. & Mitzi, D. B., Is Cs_2TiBr_6 a promising Pb-free perovskite for solar energy applications?, *J. Mater. Chem. A* **8,** 4049–4054 (2020).

153. Kong, D. *et al.,* Solution processed lead-free cesium titanium halide perovskites and their structural, thermal and optical characteristics, *J. Mater. Chem. C* **8,** 1591–1597 (2020).

154. Giannozzi, P. *et al.,* QUANTUM ESPRESSO: a modular and open-source software project for quantum simulations of materials, *J. Condens. Matter Phys.* **21,** 395502 (2009).

155. Giannozzi, P. *et al.,* Advanced capabilities for materials modelling with Quantum ESPRESSO, *J. Condens. Matter Phys.* **29,** 465901 (2017).

156. van Setten, M. *et al.,* The PseudoDojo: Training and grading a 85 element optimized norm-conserving pseudopotential table, *Comput. Phys. Commun.* **226,** 39–54 (2018).

157. Cucco, B. *et al.,* Electronic structure and stability of Cs2TiX6 and Cs2ZrX6 (X = Br, I) vacancy ordered double perovskites, *Appl. Phys. Lett.* **119** (2021).

158. Salluzzo, M. *et al.,* Orbital Reconstruction and the Two-Dimensional Electron Gas at the $LaAlO_3/SrTiO_3$ Interface, *Phys. Rev. Lett.* **102,** 166804 (2009).

159. Persson, C., Zhao, Y.-J., Lany, S. & Zunger, A., *n*-type doping of $CuInSe_2$ and $CuGaSe_2$, *Phys. Rev. B* **72,** 035211 (2005).

160. Jain, A. *et al.,* Commentary: The Materials Project: A materials genome approach to accelerating materials innovation, *APL Mater.* **1** (2013).

161. Guthrie, D. H. & Corbett, J. D., Two zirconium iodide clusters. Hexazirconium dodecaiodide (Zr6I12) and cesium hexazirconium tetradecaiodide (CsZr6I14), *Inorg. Chem.* **21,** 3290–3295 (1982).

162. Cucco, B., Katan, C., Even, J., Kepenekian, M. & Volonakis, G., Fine Structure of Excitons in Vacancy-Ordered Halide Double Perovskites, *ACS Mat. Lett.* **5,** 52–59 (2023).

163. Zheng, K. *et al.,* Vacancy-Ordered Double Perovskite Rb2ZrCl6xBrx: Facile Synthesis and Insight into Efficient Intrinsic Self-Trapped Emission, *Adv. Opt. Mater.* **10,** 2101661 (2022).

164. Kaltzoglou, A. *et al.,* Optical-Vibrational Properties of the Cs_2SnX_6 (X = Cl, Br, I) Defect Perovskites and Hole-Transport Efficiency in Dye-Sensitized Solar Cells, *J. Phys. Chem. C* **120,** 11777–11785 (2016).

165. Folgueras, M. C. *et al.,* Lattice Dynamics and Optoelectronic Properties of Vacancy-Ordered Double Perovskite Cs_2TeX_6 (X = Cl–, Br–, I–) Single Crystals, *J. Phys. Chem. C* **125,** 25126–25139 (2021).

166. Jong, U.-G. *et al.,* Anharmonic phonons and phase transitions in the vacancy-ordered double perovskite Cs_2SnI_6 from first-principles predictions, *Phys. Rev. B* **99,** 184105 (2019).

167. Kavanagh, S. R. *et al.,* Frenkel Excitons in Vacancy-Ordered Titanium Halide Perovskites (Cs2TiX6), *J. Phys. Chem. Lett.* **13,** 10965–10975 (2022).

168. Vázquez-Fernández, I. *et al.,* Vacancy-Ordered Double Perovskite Cs2TeI6 Thin Films for Optoelectronics, *Chem. Mater.* **32,** 6676–6684 (2020).

169. Marongiu, D., Saba, M., Quochi, F., Mura, A. & Bongiovanni, G., The role of excitons in 3D and 2D lead halide perovskites, *J. Mater. Chem. C* **7,** 12006–12018 (2019).

170. Galkowski, K. *et al.,* Determination of the exciton binding energy and effective masses for methylammonium and formamidinium lead tri-halide perovskite semiconductors, *Energy Environ. Sci.* **9,** 962–970 (2016).

171. Palummo, M., Berrios, E., Varsano, D. & Giorgi, G., Optical Properties of Lead-Free Double Perovskites by Ab Initio Excited-State Methods, *ACS Energy Lett.* **5,** 457–463 (2020).

172. Miyata, A. *et al.,* Direct measurement of the exciton binding energy and effective masses for charge carriers in organic–inorganic tri-halide perovskites, *Nat. Physics* **11,** 582–587 (2015).

173. Wannier, G. H., The Structure of Electronic Excitation Levels in Insulating Crystals, *Phys. Rev.* **52,** 191–197 (1937).

174. Becker, M. A. *et al.,* Bright triplet excitons in caesium lead halide perovskites, *Nature* **553,** 189–193 (2018).

175. Mao, L., Stoumpos, C. C. & Kanatzidis, M. G., Two-Dimensional Hybrid Halide Perovskites: Principles and Promises, *J. Am. Chem. Soc.* **141,** 1171–1190 (2019).

176. Matheu, R., Vigil, J. A., Crace, E. J. & Karunadasa, H. I., The halogen chemistry of halide perovskites, *Trends Chem.* **4,** 206–219 (2022).

177. Xie, Y., Yu, H., Duan, J., Xu, L. & Hu, B., Enhancing device performance in quasi-2D perovskite ((BA) 2 (MA) 3Pb4I13) solar cells using PbCl2 additives, *ACS Appl. Mater. Interfaces* **12,** 11190–11196 (2020).

178. Gélvez-Rueda, M. C. *et al.,* Interconversion between Free Charges and Bound Excitons in 2D Hybrid Lead Halide Perovskites, *J. Phys. Chem. C* **121,** 26566–26574 (2017).

179. Connor, B. A., Leppert, L., Smith, M. D., Neaton, J. B. & Karunadasa, H. I., Layered Halide Double Perovskites: Dimensional Reduction of Cs2AgBiBr6, *J. Am. Chem. Soc.* **140,** 5235–5240 (2018).

180. Kober-Czerny, M. *et al.,* Excellent Long-Range Charge-Carrier Mobility in 2D Perovskites, *Adv. Funct. Mater.* **32,** 2203064 (2022).

181. Popescu, V. & Zunger, A., Extracting E versus k effective band structure from supercell calculations on alloys and impurities, *Phys. Rev. B* **85,** 085201 (2012).

182. Zacharias, M. & Giustino, F., Theory of the special displacement method for electronic structure calculations at finite temperature, *Phys. Rev. Res.* **2** (2020).

183. Marchenko, E. I. *et al.,* Database of Two-Dimensional Hybrid Perovskite Materials: Open-Access Collection of Crystal Structures, Band Gaps, and Atomic Partial Charges Predicted by Machine Learning, *Chem. Mater.* **32,** 7383–7388 (2020).

184. Milot, R. L., Eperon, G. E., Snaith, H. J., Johnston, M. B. & Herz, L. M., Temperature-Dependent Charge-Carrier Dynamics in CH3NH3PbI3 Perovskite Thin Films, *Adv. Funct. Mater.* **25,** 6218–6227 (2015).

185. Karakus, M. *et al.,* Phonon–Electron Scattering Limits Free Charge Mobility in Methylammonium Lead Iodide Perovskites, *J. Phys. Chem. Lett.* **6,** 4991–4996 (2015).

186. Milot, R. L. *et al.,* Charge-Carrier Dynamics in 2D Hybrid Metal–Halide Perovskites, *Nano Lett.* **16,** 7001–7007 (2016).

187. Buizza, L. R. V. *et al.,* Charge-Carrier Dynamics, Mobilities, and Diffusion Lengths of 2D–3D Hybrid Butylammonium–Cesium–Formamidinium Lead Halide Perovskites, *Adv. Funct. Mater.* **29,** 1902656 (2019).

188. Ziegler, J. D. *et al.,* Excitons at the Phase Transition of 2D Hybrid Perovskites, *ACS Photonics* **9,** 3609–3616 (2022).

189. Ludwig, W. & Falter, C., *Symmetries in physics: group theory applied to physical problems* 256–258 (Springer Science & Business Media, 2012).

190. Even, J. *et al., Carrier scattering processes and low energy phonon spectroscopy in hybrid perovskites crystals in Physics, Simulation, and Photonic Engineering of Photovoltaic Devices V* (eds Freundlich, A., Lombez, L. & Sugiyama, M.) **9743** (SPIE, 2016), 97430M.

191. Schlipf, M., Poncé, S. & Giustino, F., Carrier Lifetimes and Polaronic Mass Enhancement in the Hybrid Halide Perovskite $CH_3NH_3PbI_3$ from Multiphonon Fröhlich Coupling, *Phys. Rev. Lett.* **121,** 086402 (2018).

192. Leveillee, J., Volonakis, G. & Giustino, F., Phonon-Limited Mobility and Electron–Phonon Coupling in Lead-Free Halide Double Perovskites, *J. Phys. Chem. Lett.* **12,** 4474–4482 (2021).

193. Grimvall, G., *The Electron-phonon Interaction in Metals* ISBN: 9780444861054 (North-Holland Publishing Company : sole distributors for the U.S.A. and Canada, Elsevier North-Holland, 1981).

194. Li, W., Poncé, S. & Giustino, F., Dimensional Crossover in the Carrier Mobility of Two-Dimensional Semiconductors: The Case of InSe, *Nano Lett.* **19,** 1774–1781 (2019).

195. Hoye, R. L. Z. *et al.,* The Role of Dimensionality on the Optoelectronic Properties of Oxide and Halide Perovskites, and their Halide Derivatives, *Adv. Energy Mater.* **12,** 2100499 (2022).

196. Chen, C. *et al.,* White-light emission lead-free perovskite phosphor Cs2ZrCl6:Sb3+, *Ceram. Int.* **48,** 1851–1856 (2022).

197. Patrick, C. E. & Giustino, F., GW quasiparticle bandgaps of anatase TiO2 starting from DFT + U, *J. Condens. Matter Phys.* **24,** 202201 (2012).

198. Yuan, Z. *et al.,* One-dimensional organic lead halide perovskites with efficient bluish white-light emission, *Nature Comm.* **8,** 14051 (2017).

199. Zhu, C. *et al.,* Many-Body Correlations and Exciton Complexes in CsPbBr3 Quantum Dots, *Adv. Mater.* **35,** 2208354 (2023).

200. Wang, Z. *et al.,* Efficient ambient-air-stable solar cells with 2D–3D heterostructured butylammonium-caesium-formamidinium lead halide perovskites, *Nat. Energy* **2,** 1–10 (2017).

201. Rubel, O., Tran, F., Rocquefelte, X. & Blaha, P., Perturbation Approach to Ab Initio Effective Mass Calculations, *Comput. Phys. Commun.* **261,** 107648 (2021).

202. Hajinazar, S., Thorn, A., Sandoval, E. D., Kharabadze, S. & Kolmogorov, A. N., MAISE: Construction of neural network interatomic models and evolutionary structure optimization, *Comput. Phys. Commun.* **259,** 107679 (2021).

203. Rojas, H. N., Godby, R. W. & Needs, R. J., Space-Time Method for Ab Initio Calculations of Self-Energies and Dielectric Response Functions of Solids, *Phys. Rev. Lett.* **74,** 1827–1830 (1995).

204. Kronik, L. & Neaton, J. B., Excited-State Properties of Molecular Solids from First Principles, *Annu. Rev. Phys. Chem.* **67,** 587–616 (2016).

205. Filip, M. R. & Giustino, F., GW quasiparticle band gap of the hybrid organic-inorganic perovskite $CH_3NH_3PbI_3$: Effect of spin-orbit interaction, semicore electrons, and self-consistency, *Phys. Rev. B* **90** (2014).

206. Ning, W. & Gao, F., Structural and functional diversity in lead-free halide perovskite materials, *Adv. Mater.* **31,** 1900326 (2019).

207. Ma, C. *et al.,* Centimeter-Sized 2D Perovskitoid Single Crystals for Efficient X-ray Photoresponsivity, *Chem. Mater.* **34,** 1699–1709 (2022).

208. Xu, F. *et al.,* 1D Perovskitoid as Absorbing Material for Stable Solar Cells, *Crystals* **11** (2021).

209. Kong, T. *et al.,* Perovskitoid-Templated Formation of a 1D@3D Perovskite Structure toward Highly Efficient and Stable Perovskite Solar Cells, *Adv. Energy Mater.* **11,** 2101018 (2021).

210. Jeong, J. *et al.,* Pseudo-halide anion engineering for α-FAPbI3 perovskite solar cells, *Nature* **592,** 381–385 (2021).

211. Nechache, R. *et al.,* Bandgap tuning of multiferroic oxide solar cells, *Nat. Photonics* **9,** 61–67 (2015).

APPENDIX A

COMPUTATIONAL DETAILS

A.1 Chapter 3

All the calculations in this section are performed within the DFT framework using Quantum ESPRESSO Suite [154, 155]. All the structures are relaxed with an 80 Ry cutoff for the plane-wave kinetic energy with a converged $8 \times 8 \times 8$ Brillouin zone sampling. The threshold on forces and total energy during ionic minimization were converged to 10^{-6} alongside a threshold of 10^{-10} for the SCF steps. All the calculations are performed using fully-relativistic norm-conserving PBE pseudopotential [156] taken from the pseudo-dojo database (http://www.pseudo-dojo.org). The optical absorption calculations are performed using the YAMBO [115] code. Calculations are performed within random phase approximation (RPA) employing a dense $16 \times 16 \times 16$ k-point grid and 800 bands. Furthermore, the optical spectra are scissor shifted to match the PBE0 band gap. The hybrid DFT-PBE0 calculations are performed using a $4 \times 4 \times 4$ k-grid sampling with a $2 \times 2 \times 2$ q-grid sampling for the Fock operator. The hybrid band structures are interpolated using the code Wannier90 [113]. We employed a fine $50 \times 50 \times 50$ k-point grid, where $Ag-d$, $Bi-p$, and $I-p$ orbitals are used as the basis to construct the Wannier functions. The effective masses are evaluated via a degenerate perturbation k.p approach with the direct evaluation of the velocity and momentum matrix elements, as implemented on the *mstar* code by O. Rubel *et al.*[201]. These calculations include 1000 bands for the evaluation of the optical matrix. The radial distribution functions (RDF) are evaluated using the code Module for Ab-Initio Structure Evolution (MAISE) [202].

A.2 Chapter 4

All the calculations within the DFT framework are performed using the Quantum ESPRESSO Suite [154, 155]. Structures are optimized with a 90 Ry cutoff for the plane-wave kinetic energy with a $8 \times 8 \times 8$ Brillouin zone sampling. The threshold on forces and total energy

during ionic minimization were converged to 10^{-6} and 10^{-11}, respectively. During the optimization, a 0.1 Kbar threshold is employed for the pressure on the variable cell. A threshold of 10^{-11} is employed for the SCF steps. All the calculations are performed using fully-relativistic norm-conserving PBE pseudopotential [156] taken from the pseudo-dojo database (http://www.pseudo-dojo.org). The phonon calculations are performed within the DFPT framework, as also implemented in Quantum ESPRESSO. A $4 \times 4 \times 4$ k-grid is employed for the SCF, while the phonons are solved in a $2 \times 2 \times 2$ q-grid. A 10^{-16} threshold for phonon self-consistency is employed. For the electronic band structure symmetry analysis, we assume a cubic structure for Cs_2SnI_6 due to the structural and energetic similarities between the perfectly cubic crystalline structure and the distorted/rotated one. The total energy difference between the perfectly cubic and slightly tilted Cs_2SnI_6 is smaller than 1 meV/atom. The G_0W_0 calculations are performed on a $6 \times 6 \times 6$ k-grid sampling using the Rojas-Godby-Needs plasmon pole model to treat the frequency-dependent dielectric function[203]. Spin-orbit coupling is accounted for non-perturbatively. We employ the equivalent of a 15 Ry cutoff to set several G vectors to be summed in the expression of the exchange self-energy alongside an 8 Ry cutoff for the dielectric function calculation. We also include 400 bands for the sum over state summation in the GW correlation self-energy term. We included 600 polarization function bands for the calculation of the static dielectric screening. Furthermore, due to well knows problems regarding perovskites GW calculations with half-shell pseudopotentials [36, 205], we employed full-shells for all the pseudopotentials used in this work. Optical absorption calculations are performed using the YAMBO [115] code. Calculations are performed within the Bethe-Salpeter formalism for e-h coupling and also the IP approach. The BSE is solved within the Tamm-Dancoff approximation[204] on top of the G_0W_0 calculations by direct diagonalization on a uniform $6 \times 6 \times 6$ k-grid with 26 included bands around the band edges. We employ a cutoff of 10 Ry and 2 Ry for the summations on the reciprocal lattice vectors which appear in the exchange and attraction terms of the kernel, respectively. The calculations are performed using the same static dielectric screening from GW. For the exciton spacial distribution, the hole position r_h is fixed close to the halogen atoms. This assumption comes from the fact that the VBM of these compounds is mainly composed of halogen-p orbitals. The G_0W_0 band structures were interpolated with Wannier90 [113] on a dense $50 \times 50 \times 50$ k-grid to evaluate accurate effective masses. The orbitals composing the VBM and CBM of each material were used as the basis to construct the Wannier functions. The effective masses were obtained by applying the finite differences method to the Wannier interpolated band structures, as implemented on the WannierTools [114] software package.

A.3 Chapter 5

The calculations in this section are performed within the DFT framework using Quantum ESPRESSO Suite [154, 155]. All the structures are relaxed with an 80 Ry cutoff for the plane-wave kinetic energy with a converged $8 \times 8 \times 1$ Brillouin zone sampling. The threshold on forces and total energy during ionic minimization were converged to 10^{-6} alongside a threshold of 10^{-10} for the SCF steps. All the calculations are performed using fully-relativistic norm-conserving PBE pseudopotential [156] taken from the pseudo-dojo database (http://www.pseudo-dojo.org). The unfolding is performed using the Quantum ESPRESSO package using the methodology implemented by M. Zacharias and F. Giustino [182].

A.4 Chapter 6

All the calculations within the DFT framework are performed using the Quantum ESPRESSO Suite [154, 155]. Structures are optimized with a 80 Ry cutoff for the plane-wave kinetic energy with a $4 \times 4 \times 1$ Brillouin zone sampling for the layered systems and $4 \times 4 \times 4$ for the bulk system. The threshold on forces and total energy during ionic minimization were converged to 10^{-6} and 10^{-11}, respectively. During the optimization, a 0.1 Kbar threshold is employed for the pressure on the variable cell. A threshold of 10^{-11} is employed for the SCF steps. All the calculations are performed using norm-conserving PBE pseudopotential [156] taken from the pseudo-dojo database (http://www.pseudo-dojo.org). The phonon calculations are performed within the DFPT framework, as also implemented in Quantum ESPRESSO. A $4 \times 4 \times 1$ k-grid and q-grid are employed for the SCF and phonon calculations of layered systems, while $4 \times 4 \times 4$ k-grid and q-grid are employed for the bulk. A 10^{-17} threshold for phonon self-consistency is employed. We use Wannier interpolation to interpolate the valence band of all materials, for this purpose, Pb s-orbitals are used as a basis for the interpolation. The Wannierization is done on top coarse k-grids of $8 \times 8 \times 1$ and $8 \times 8 \times 8$ for layered and bulk systems, respectively. Both electronic and phonon bands are interpolated in dense k-grid and q-grid of $60 \times 60 \times 1$ and $60 \times 60 \times 60$ to evaluate accurate transport properties. Transport properties are evaluated using the Boltzmann iterative transport equation discussed in the methodology section, as implemented in the EPW code [116].

APPENDIX B

COMPLEMENTARY RESULTS OF CHAPTER 4

B.1 Decomposition Pathway Diagrams and Equations

In the following we present the decomposition pathway diagrams for Cs_2TiI_6 and Cs_2ZrBr_6. Similar to the case of Cs_2TiBr_6 and Cs_2ZrI_6, these compounds exhibit a stability region approx-

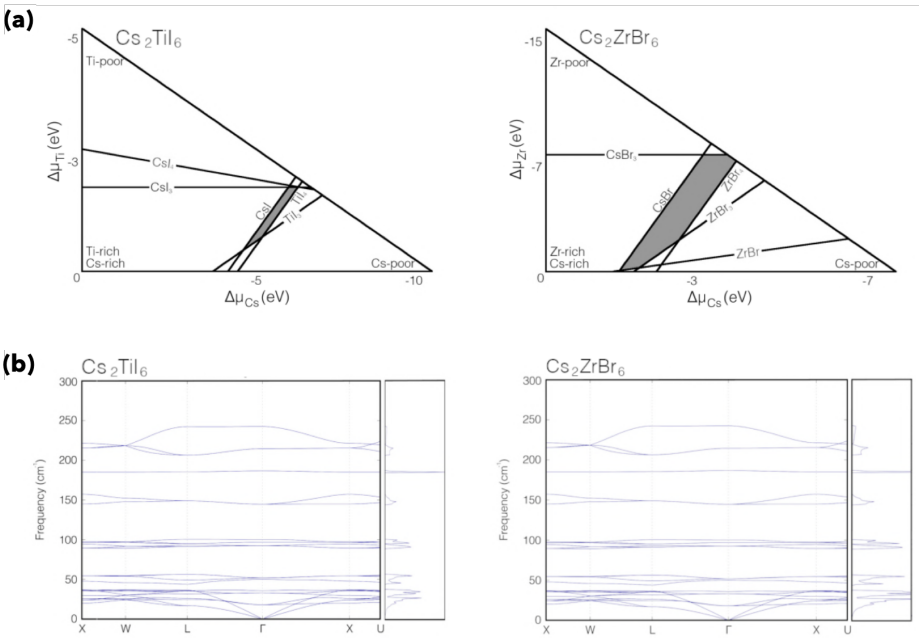

Figure B.1 – (a) Decomposition pathway diagrams for Cs_2TiI_6 and Cs_2ZrBr_6 with stability region represented as the gray shaded area. (b) Phonon dispersion and density of states. The absence of imaginary (or soft) modes indicates dynamical stability. Figure extracted and adapted from reference [157].

imately at the center of the diagram. The absence of negative phonon modes indicates the dynamical stability of the lattice.

Next, we present the stability inequalities for all compounds and competing phases considered in this analysis.

1. Competing phases of $\mathbf{Cs_2TiBr_6}$**:**

$$\Delta\mu_{Cs} + \Delta\mu_{Br} \leq -0.2658 \text{ Ry/f.u.}$$
$$\Delta\mu_{Cs} + 3\Delta\mu_{Br} \leq -0.2918 \text{ Ry/f.u.}$$
$$\Delta\mu_{Cs} + \Delta\mu_{Ti} + 3\Delta\mu_{Br} \leq -0.4981 \text{ Ry/f.u.}$$
$$7\Delta\mu_{Ti} + 16\Delta\mu_{Br} \leq -1.9399 \text{ Ry/f.u.}$$
$$\Delta\mu_{Ti} + 3\Delta\mu_{Br} \leq -0.3517 \text{ Ry/f.u.}$$
$$\Delta\mu_{Ti} + 4\Delta\mu_{Br} \leq -0.4576 \text{ Ry/f.u.}$$

2. Competing phases of $\mathbf{Cs_2TiI_6}$**:**

$$\Delta\mu_{Cs} + l\Delta\mu_{I} \leq -0.2293 \text{ Ry/f.u.}$$
$$\Delta\mu_{Cs} + 3\Delta\mu_{I} \leq -0.2456 \text{ Ry/f.u.}$$
$$\Delta\mu_{Cs} + 4\Delta\mu_{I} \leq -0.2486 \text{ Ry/f.u.}$$
$$\Delta\mu_{Ti} + 3\Delta\mu_{I} \leq -0.2350 \text{ Ry/f.u.}$$
$$\Delta\mu_{Ti} + 4\Delta\mu_{I} \leq -0.2779 \text{ Ry/f.u.}$$

3. Competing phases of $\mathbf{Cs_2ZrBr_6}$**:**

$$\Delta\mu_{Cs} + \Delta\mu_{Br} \leq -0.2658 \text{ Ry/f.u.}$$
$$\Delta\mu_{Cs} + 3\Delta\mu_{Br} \leq -0.2918 \text{ Ry/f.u.}$$
$$\Delta\mu_{Zr} + \Delta\mu_{Br} \leq -0.1531 \text{ Ry/f.u.}$$
$$\Delta\mu_{Zr} + 3\Delta\mu_{Br} \leq -0.4220 \text{ Ry/f.u.}$$
$$\Delta\mu_{Zr} + 4\Delta\mu_{Br} \leq -0.51345 \text{ Ry/f.u.}$$

4. Competing phases of $\mathbf{Cs_2ZrI_6}$**:**

$$3\Delta\mu_{Cs} + 2\Delta\mu_{Zr} + 9\Delta\mu_{I} \leq -1.2691 \text{ Ry/f.u.}$$
$$\Delta\mu_{Cs} + \Delta\mu_{I} \leq -0.2293 \text{ Ry/f.u.}$$
$$\Delta\mu_{Cs} + 3\Delta\mu_{I} \leq -0.2456 \text{ Ry/f.u.}$$
$$\Delta\mu_{Cs} + 4\Delta\mu_{I} \leq -0.2486 \text{ Ry/f.u.}$$
$$\Delta\mu_{Zr} + 2\Delta\mu_{I} \leq -0.1980 \text{ Ry/f.u.}$$
$$\Delta\mu_{Zr} + 3\Delta\mu_{I} \leq -0.2867 \text{ Ry/f.u.}$$
$$\Delta\mu_{Zr} + 4\Delta\mu_{I} \leq -0.3449 \text{ Ry/f.u.}$$

APPENDIX C

ACHIEVEMENTS

C.1 List of Publications (2020-2023)

- **B. Cucco**, C. Katan, J. Even, M. Kepenekian and G. Volonakis, "Fine Structure of Excitons in Vacancy-Ordered Halide Double Perovskites". ACS Materials Letters 5, 52-59, 2023.
- **B. Cucco**, L. Pedesseau, C. Katan, J. Even, M. Kepenekian and G. Volonakis, "Silver-Bismuth Halide Double Salts for Lead-Free Photovoltaic: Insights from Symmetry-Based Modeling". Solar RRL 6, 2200718, 2022.
- P. Fu, M. A. Quintero, C. Welton, X. Li, **B. Cucco**, M. C. De Siena, J. Even, G. Volonakis, M. Kepenekian, R. Liu, C. C. Laing, V. Klepov, Y. Liu, V. P. Dravid, G. N. M. Reddy, C. Li, and M. G. Kanatzidis, "Short Aromatic Diammonium Ions Modulate Distortions in 2D Lead Bromide Perovskites for Tunable White-Light Emission". Chemistry of Materials 34, 9685-9698, 2022.
- **B. Cucco**, G. Bouder, L. Pedesseau, C. Katan, J. Even, M. Kepenekian and G. Volonakis, "Electronic Structure and Stability of Cs_2TiX_6 and Cs_2ZrX_6 (X = Br, I) Vacancy Ordered Double Perovskites". Applied Physics Letters 119, 181903, 2021.

C.2 Awards

- *Young Researcher Award* for the work on Ag/Bi double salts. European Materials Research Society (E-MRS), 2021.
- *Young Researcher Award* for the work on the fine structure of excitons in vacancy-ordered double perovskites. Nanotexnology - ISFOE, 2023.

C.3 Oral Communications in International Conferences

- Fine Structure of Excitons in Vacancy-Ordered Double Perovskites. ISFOE 2023, Thessaloniki, Greece, 2023.
- Fine Structure of Excitons in Vacancy-Ordered Halide Double Perovskites. APS March Meeting, Las Vegas, United States of America, 2023.
- Excitonic Properties of Vacancy Ordered Double Perovskites – Electron-Hole Coupling and GW Quasi-Particles. MRS Fall Meeting, Boston, United States, 2022.
- Bi/Ag Double Salts for Solar-Cell Applications. Journée Scientifique – LUMOMAT, Rennes, France, 2022.
- Bi/Ag Double Salts for Solar-Cell Applications: Insights on their Structures and Opto-Electronic properties. Peroquium: A Two-Days Workshop on Perovskites, Palaiseau, France, 2022.
- Rudorffites for Solar-Cell Applications: Insights on their Structures, Electronic and Optical Properties from First-Principles. E-MRS Spring Meeting, Online, 2021.
- Electronic Structure and Stability of Cs_2TiX_6 and Cs_2ZrX_6 (X = Br, I) Vacancy Ordered Halide Double Perovskites. nanoGe Fall Meeting, Online, 2021

C.4 Covers Gallery

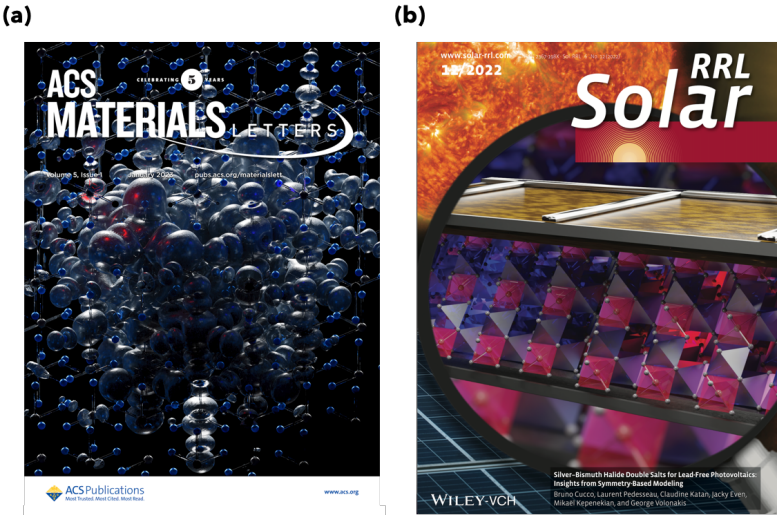

Figure C.1 – Publications that were featured as front covers of the journals. Cover (a) is related to reference [162] and (b) is related to reference [131].

RÉSUMÉ EN FRANÇAIS

Le terme "pérovskite" a été proposé en 1839 par Gustav Rose suite à la découverte d'un nouveau composé inorganique de formule chimique $CaTiO_3$ [1]. Ce minéral a été décrit comme un réseau cristallin constitué d'octaèdres TiO_6 partageant les sommets dans lequel les cations de calcium occupent le site entre les octaèdres. En dehors de quelques exceptions [8], les pérovskites oxydes présentent de larges lacunes de bande et ne sont pas particulièrement intéressantes pour les applications photo-actives. Ce n'est pas le cas d'un autre type de pérovskites qui sont formées avec des atomes d'halogène aux sommets de l'octaèdre, les pérovskites halogénées. Ces matériaux ont été décrits pour la première fois en 1893 dans le travail pionnier de H. L. Wells *et al.*, où les auteurs rapportent la synthèse d'une série de pérovskites halogénées inorganiques, parmi lesquelles des composés prototypes comme $CsPbCl_3$ et $CsPbBr_3$ [9]. De nombreuses pérovskites à base d'halogénures présentent une absorption optique dans le domaine du visible et ont ainsi attiré une attention considérable ces dernières années pour des applications en optoélectronique.

Outre les matériaux entièrement inorganiques, il est également possible de synthétiser des pérovskites halogénées hybrides organico-inorganiques où le cation est une petite molécule organique. Le premier rapport d'un matériau pérovskite hybride a été donné par Kojima *et al.*, via la synthèse de pérovskites à base de méthylammonium (MA), $CH_3NH_3PbBr_3$ ($MAPbBr_3$) et $CH_3NH_3PbI_3$ ($MAPbI_3$) [12]. Des travaux ultérieurs développés par Turren-Cruz *et al.* ont également rapporté la synthèse de pérovskites à base de formamidinium (FA) [13]. Cependant, depuis leurs premiers rapports, les pérovskites à base de FA sont connues pour être très instables, se cristallisant rapidement en phases non-péovskites photoactives [14]. Des travaux ultérieurs de Saliba *et al.* ont démontré la possibilité de stabiliser les pérovskites à base de FA en introduisant un mélange de différents cations (Cs^+, MA^+, FA^+) sur le site A [15].

Tous ces matériaux peuvent être synthétisés via une variété de techniques, y compris des procédés à faible coût qui consistent en un mélange des sels précurseurs en solution. Les techniques de traitement en solution comme le *spin-coating* et l'impression offrent des approches peu coûteuses et évolutives pour la fabrication de films de pérovskite. Ces méthodes impliquent le dépôt de solutions précurseurs sur des substrats et un recuit ultérieur pour induire la cristallisation. Les méthodes de dépôt sous vide, y compris la co-évaporation thermique et la pul-

vérisation, permettent un contrôle précis du dépôt et de la cristallisation des films. On peut optimiser la morphologie du film, la qualité cristalline et les propriétés optoélectroniques en contrôlant soigneusement les paramètres de synthèse, tels que la composition du précurseur, la température de recuit et l'épaisseur du film. Bien que le développement des technologies à base de pérovskite se soit fait rapidement, des défis restent à relever pour la commercialisation des cellule solaire à base de pérovskites (CSP) et des LEDs (*Light Emitting Diodes*) à base de pérovskite. La stabilité à long terme, la toxicité du plomb et la stabilité des couleurs sont autant de points critiques qui doivent être abordés. Il existe un effort croissant pour améliorer la stabilité des CSP en contrôlant leur structure et en développant des stratégies pour contrôler la morphologie et la cristallinité des films, via l'introduction d'additifs [66], l'optimisation des architectures des dispositifs [67], et l'encapsulation des couches de pérovskite [68], qui pourraient toutes contribuer à l'amélioration des performances à long terme et de la fiabilité des CSP et des LEDs. De plus, depuis leurs premiers développements, des préoccupations ont été soulevées concernant la présence de plomb dans les matériaux des pérovskites et ses impacts potentiels sur l'environnement et la santé [69]. Le plomb est connu pour être un métal lourd toxique, et son utilisation dans les cellules solaires à pérovskite et autres dispositifs optoélectroniques a motivé un nombre important de publications axées sur le développement d'alternatives sans plomb [70]. Ces efforts visent à atténuer les risques potentiels associés à l'exposition au plomb, en particulier pendant la fabrication, l'utilisation et l'élimination des dispositifs à base de pérovskite, tout en conservant les fantastiques propriétés électroniques apportées par le plomb. La communauté s'efforce de développer des technologies à base de pérovskite écologiques et durables en explorant des compositions et des matériaux alternatifs. Par exemple, les pérovskites à base d'étain sans Pb présentent des propriétés électroniques et optiques intéressantes mais souffrent d'instabilités bien connues [29]. D'autres approches impliquent une diversification structurelle comme les matériaux à double pérovskite [24], les doubles pérovskites ordonnées en lacune [29] et bien d'autres matériaux au-delà des pérovskites halogénures de plomb conventionnelles.

Il existe également plusieurs questions ouvertes concernant les mécanismes fondamentaux sous-jacents à toutes ces applications. Les effets de confinement diélectrique et quantique dans les structures de pérovskite de basse dimension sont connus pour donner naissance à des états excitoniques fortement liés [71], qui jouent un rôle majeur dans leurs propriétés optiques. De plus, en raison de distorsions importantes du réseau générées par la combinaison d'un fort couplage des porteurs de charge avec le réseau de pérovskite mou peut également conduire à la formation d'excitons auto-piégés [72] et de polarons [73], qui sont supposés être les principaux mécanismes sous-jacents à la large photoluminescence observée dans certaines de ces

pérovskites et une caractéristique clé dans les applications LED [74]. Les mécanismes de couplage électron-phonon dans différentes pérovskites ne sont pas encore entièrement compris, et c'est la base des propriétés de transport des porteurs de charge qui imprègnent toute application optoélectronique. De plus, le rôle de l'anharmonicité du réseau dans la transition de phase structurelle des pérovskites et son effet sur les propriétés électroniques, optiques et de transport, reste une question ouverte [10, 11]. La compréhension expérimentale et théorique de tous ces processus est cruciale pour permettre leurs applications potentielles.

Cette thèse se concentre sur l'utilisation d'approches informatiques de pointe pour relever certains de ces défis et aider à la maturation de ces technologies pour des applications industrielles et commerciales. Je discute d'aspects importants des pérovskites et des matériaux de type pérovskite, allant de leur structure électronique fondamentale à l'investigation des propriétés excitoniques et du transport des porteurs de charge. Le chapitre d'introduction de cette thèse présente une large vue d'ensemble des pérovskites conventionnelles, en énonçant les développements réalisés au cours des dernières années, leur état actuel et certains des défis qui doivent être relevés pour mûrir ces technologies. La thèse est organisée en fonction des différents types de matériaux étudiés, dont certains sont classés comme des matériaux avec des octaèdres connectés en trois dimensions, ci-après appelés "tridimensionnels", et d'autres matériaux avec des octaèdres connectés en deux dimensions (en couches). Dans chaque chapitre, je discute des détails des propriétés électroniques, optiques et de stabilité de chacun de ces matériaux et de leur adéquation aux applications optoélectroniques. Dans les chapitres 3 et 4, qui couvrent les matériaux tridimensionnels, je présente deux familles de composés sans plomb au-delà des pérovskites conventionnelles. Ces chapitres abordent à la fois les défis de stabilité et de toxicité mentionnés précédemment. Les premiers, à savoir les sels doubles Ag/Bi, présentent des propriétés électroniques et optiques prometteuses pour les applications photovoltaïques. Je présente tout d'abord des défis de modélisation de ces matériaux dans le cadre des approches dites *ab initio*. Ensuite, je développe une approche de modélisation basée sur la symétrie qui me permet de décrire correctement les propriétés structurales et électroniques de ces matériaux en excellent accord avec les données expérimentales disponibles. Enfin, je sonde leurs capacités photovoltaïques potentielles en évaluant des quantités clés telles que les rendements de conversion de puissance, les courants de court-circuit et les tensions de circuit ouvert. Les seconds, à savoir les doubles pérovskites halogénées ordonnées en lacune, se révèlent inadaptées au photovoltaïque, mais pourraient être d'excellents éléments constitutifs pour les applications luminescentes. Dans cette étude, je me concentre sur le rôle du couplage électron-trou dans ces matériaux et je démontre qu'ils peuvent héberger des états excitoniques fortement liés. Je

fournis une analyse de symétrie complète de la structure fine des excitons et donne des informations importantes sur l'application de ces composés pour la luminescence. Dans le chapitre 5, j'étudie les matériaux pérovskites doubles en couches sans plomb. J'aborde les problèmes de stabilité et de toxicité présents dans les pérovskites tout en discutant des différences critiques dans les propriétés électroniques et optiques des systèmes en couches et tridimensionnels. Enfin, dans le chapitre 6, je m'attache à décrire comment la réduction de la dimensionnalité affecte le transport des porteurs de charge dans ces matériaux, qui est une propriété fondamentale pour tout type d'application optoélectronique, et il est directement lié aux efficacités des dispositifs. Je démontre qu'il existe une limitation intrinsèque au transport de charge dans les pérovskites en couches, et que les mobilités inférieures proviennent principalement de différences dans la durée de vie des porteurs de charge. De plus, je fournis une analyse de symétrie approfondie des mécanismes de couplage électron-phonon et associe la diffusion polaire-phonon résultant du couplage Fröhlich à longue portée comme la principale source de relaxation des porteurs. De plus, pour les systèmes en couches, d'autres mécanismes tels que la diffusion du potentiel de déformation sont également autorisés par la symétrie.

COLLEGE SCIENCES DE LA MATIERE
DOCTORAL DES MOLECULES
BRETAGNE ET MATERIAUX

Université de Rennes

Titre : Modélisation Ab-initio de Matériaux Photoactifs au-delà des Pérovskites Conventionnelles à Base d'Halogénure de Plomb

Mot clés : Pérovskites, Optoélectronique, DFT, Ab-initio, Cellule Solaire, LED

Résumé : Les pérovskites halogénées sont une classe de matériaux qui ont suscité une grande attention au cours des deux dernières années en raison de leurs propriétés optoélectroniques exceptionnelles, qui ont permis de créer des cellules solaires et des LEDs à haut rendement. Cependant, de nombreux défis restent à relever avant de pouvoir envisager la commercialisation de dispositifs à base de pérovskites, tels que la stabilité à long terme, l'obtention de plus grandes surfaces et la toxicité. Cette thèse de science des matériaux computationnelle se concentre sur les travaux théoriques que j'ai développé pour relever certains de ces défis et ainsi contribuer à la maturation de ces technologies en vue d'applications industrielles et commerciales. Grâce à des calculs ab-initio à l'état de l'art, j'ai exploré les propriétés structurelles, électroniques, optiques et de transport de matériaux parents des pérovskites d'halogénure conventionnelles tels que les sels doubles Ag/Bi, les pérovskites en couches et les pérovskites doubles d'halogénure ordonnées par vacance. J'ai établi qu'il était possible d'obtenir des matériaux sans plomb qui stables et présentant des propriétés optoélectroniques adaptables à différents types d'applications, ouvrant ainsi la voie à des dispositifs optoélectroniques plus efficaces, plus stables et non toxiques.

Title: Ab-initio Modeling of Photo-Active Materials Beyond Conventional Lead Halide Perovskites

Keywords: Perovskites, Optoelectronics, DFT, Ab-initio, Solar-cell, LED

Abstract: Halide perovskites are a class of materials that have drawn significant attention throughout the past couple of years due to their exceptional optoelectronic properties, leading to high-efficiency solar-cells and LEDs. Yet, many challenges remain prior to the commercialization of perovskite-based devices, such as long-term stability, scalability, and toxicity. As a computational material scientist, this thesis will focus on the theoretical works I develop to address some of these challenges and help mature these technologies for industrial and commercial applications. I will employ state-of-art ab-initio calculations to explore the structural, electronic, optical, and transport properties of materials beyond conventional halide perovskites such as Ag/Bi double salts, layered perovskites, and vacancy-ordered halide double perovskites. I will show that is possible to achieve lead-free materials that are stable and have tunable optoelectronic properties for different types of applications, paving the way to more efficient and stable optoelectronic devices based on lead-free perovskites and perovskite-like materials.